2017

Advanced Carbon Materials Based Electrodes for High Performance Symmetric Supercapacitors

Keliang Wang
South Dakota State University

ADVANCED CARBON MATERIALS BASED ELECTRODES FOR HIGH PERFORMANCE SYMMETRIC SUPERCAPACITORS

BY

KELIANG WANG

A dissertation submitted in partial fulfillment of the requirements for the

Doctor of Philosophy

Major in Biological Science

Specialization in Agricultural & Biosystems Engineering

South Dakota State University

2017

ADVANCED CARBON MATERIALS BASED ELECTRODES FOR HIGH PERFORMANCE SYMMETRIC SUPERCAPACITORS

This dissertation is approved as a creditable and independent investigation by a candidate for the Doctor of Philosophy in Biological Science degree and is acceptable for meeting the dissertation requirements for this degree. Acceptance of this does not imply that the conclusions reached by the candidate are necessarily the conclusions of the major department.

Zhengrong Gu, Ph.D.
Dissertation Advisor Date

Van Kelley, Ph.D.
Head, Department of Date
Agricultural and Biosystems Engineering

Dean, Graduate School Date

This dissertation is dedicated to my families who give me support at every moment as always.

ACKNOWLEDGEMENTS

This dissertation would not have been completed without the support that I have received from my committee members, friends and families over the past 32 months. I would like to express my heartfelt gratitude to the following people.

To my advisor Prof. Zhengrong Gu. Thank you for his advice, patience and support of my Ph.D. study and research.

To the rest of my committee members: Dr. James Julson, Dr. Semhar Michael, and Dr. Songxin Tan, for their encouragement, valuable suggestions, and time.

Special gratitude goes to Prof. Qi Hua Fan, who has moved to Michigan State University. For his patience, kindness, fund support, valuable suggestion to my research and life, encouragement and recognition to me. You are far more than an advisor to me.

To staffs in ABE department: Candy Rogness, Christina Lapsley, Jasmine Greene, Jeff Vander Schaaf, and Susan Goens, for their kindness and help.

To my lab mates and collaborators: Hong Jin, Maria Castro, Shouyun Cheng, Xianhui Zhao, Xiaomin Wang and Yuhe Cao, for your kind help in lab life; And Dr. Bing Luo, Mr. Jason Croat, Dr. James D Hoefelmeyer, Dr. Joun Lee, Dr. Jun Liu, Dr. Lloyd, Mtzger, Dr. Phil Ahrenkiel, Dr. Parashu Ram Kharel, Dr. Tylor Johnson, and Dr. Wiliam Gibbons, for their kind help in sample analysis, support and time to my research work.

To my friends: Ashik Sahani, Biyi Chen, Chunyang Wang & Li Wang, Ke Chen, Kee Wee Tan, Ke Yang, Liyan Chen, Lingxi Zhu, Lin Wei, John Fan, Jianyuan Sun, Huiui Yin, Maheshwar Shrestha, Shenggang Wang, Xiaohui Ji, Xiaoyu Ji, Xiaona Li, Xiaoli Mao & Yilei Huang, Yue Huang, Yu Shen, Yi Xu, Zhibo Yang, etc., a fantastic time is enjoyed with all you guys and I am so glad to meet with you.

The deepest gratitude goes to my families: my farther who is looking down to me, my mother, parents-in-law, my wife, brother, sister-in-law, nephew, ect., who are always standing by me. Thank you for your giving without cost.

Note: all mentioned names are in alphabetical order.

CONTENTS

ABSTRACT..... xi

Chapter 1 Introduction 1

Chapter 2 Nickel catalytic graphitized porous carbon as electrode material for high performance supercapacitors 9

2.1 Introduction 9

2.2 Material and methods 11

2.2.1 Preparation of activated carbon 11

2.2.2 Preparation of original carbon 12

2.2.3 Preparation of activated carbon without Ni catalyst.....12

2.2.4 Fabrication of electrodes 12

2.2.5 Physical characterization 12

2.2.6 Electrochemical characterization.....13

2.3 Results and discussion.....13

2.4 Conclusion.....23

Chapter 3 Pyrolytic cyanobacteria derived activated carbon as high performance electrode in symmetric supercapacitor.....25

3.1 Introduction 25

3.2 Experimental 27

3.2.1 Preparation of activation and original carbon 27

3.2.2 Preparation of electrodes 28

3.2.3 Physical characterization 28

3.2.4 Electrochemical characterization.....29

3. 3 Results and discussion.....30

3. 4 Conclusions 37

Chapter 4 Symmetric supercapacitors using urea-modified lignin derived N-doped porous carbon as electrode materials in liquid and solid electrolytes.....38

4.1 Introduction 38

4.2 Experimental 41

4.2.1 Preparation of activated carbon 41

4.2.2 Preparation of solid electrolyte.....41

4.2.3 Preparation of electrodes 42

4.2.4 Physical characterization 42

4.2.5 Electrochemical characterization.....43

4.3 Results and discussion.....43

4.4 Conclusions 52

Chapter 5 Rod-shape porous carbon derived from aniline modified lignin for symmetric supercapacitors.....53

5.1 Introduction 53

5.2 Experimental 55

5.2.1 Preparation of activated carbon 55

5.2.2 Preparation of electrodes 56

5.2.3 Physical characterization 56

5.2.4 Electrochemical characterization.....57

5.3 Results and discussion.....57

5.4 Conclusion.....68

Chapter 6 Nitrogen-modified biomass-derived cheese-like porous carbon for electric double layer capacitors 69

6.1 Introduction 69

6.2 Experimental 71

6.2.1 Preparation of electrode materials 71

6.2.2 Assembly of supercapacitors 72

6.2.3 Physical characterization 73

6.2.4 Electrochemical characterization.....73

6.3 Results and discussion.....73

6.4 Conclusions 83

Chapter 7 Pyrrole modified biomass derived hierarchical porous carbon as high performance symmetrical supercapacitor electrodes 84

7.1 Introduction 84

7.2 Experimental 86

7.2.1 Preparation of activated carbon 86

7.2.2 Preparation of electrodes 87

7.2.3 Physical characterization 87

7.2.4 Electrochemical characterization.....88

7.3 Results and discussion.....88

7.4 Conclusions.....94

Chapter 8 Porous carbon derived from aniline-modified fungus for symmetrical supercapacitor electrodes.....96

8.1 Introduction.....96

8.2 Experimental.....98

8.2.1 Preparation of activated carbon.....98

8.2.2 Preparation of electrodes.....98

8.2.3 Physical characterization.....99

8.2.4 Electrochemical characterization.....100

8.3 Results and discussion.....100

8.4 Conclusions.....106

Chapter 9 Plasma-assisted fabrication of graphene for symmetric supercapacitors108

9.1 Introduction.....108

9.2 Experimental.....109

9.2.1 Preparation of graphite oxides.....109

9.2.2 Preparation of graphene.....110

9.2.3 Preparation of electrodes.....111

9.2.4 Physical characterization.....111

9.2.5 Electrochemical characterization....112

9.3 Results and discussion....112

9.4 Conclusions....121

Chapter 10 Low-temperature plasma exfoliated N-doped graphene for symmetrical electrode supercapacitors....122

10.1 Introduction....122

10.2 Material and methods....125

10.2.1 Preparation of graphite oxides....125

10.2.2 Preparation of N-modified graphite oxides....126

10.2.3 Preparation of graphene....126

10.2.4 Preparation of N-doped graphene....127

10.2.5 Preparation of supercapacitor electrodes....127

10.2.6 Physical characterization....127

10.2.7 Electrochemical characterization....128

10.3 Results and discussion....128

10.4 Conclusions....147

CONCLUSIONS....147

REFERENCES....148

PUBLICATIONS....171

ABSTRACT

ADVANCED CARBON MATERIALS BASED ELECTRODES FOR HIGH PERFORMANCE SYMMETRIC SUPERCAPACITORS

KELIANG WANG

2017

Supercapacitors have received considerable attention due to their high energy density, long life time, rapid charge/discharge rate, and because they are environmental friendly technology. Electrode materials play a key role in the final performance of supercapacitors. Carbon, usually used as symmetric supercapacitors electrode materials, exhibit extraordinary stability in harsh electrolyte and electrochemical performance owing to its physical and chemical properties. In addition, porous structure originated from activation, excellent electrical conductivity, sustainability, wide availability and low cost further offering the improvement in electrochemical performance and make it to be a promising electrode material for symmetric supercapacitors. Considering the factors affected electrochemical performance, such as surface area, pore size and functional groups, several carbon materials are developed and used as high performance symmetric supercapacitors electrodes. In this work, porous carbon derived from different biomass are prepared *via* catalytic graphitization, KOH activation, and plasma treatment. Depending on detailed physical characterizations, porous structure with high surface area and porosity are presented for prepared carbon materials, which serves as reservoir and ion channels for electrolyte and consequently resulted in high capacitance performance for assembled supercapacitors evaluated by electrochemical measurements.

Chapter 1 Introduction

Energy has been rising as a hot spot with increasing energy demand all over the world. According to the Statistics Data of International Energy Outlook 2016 form U.S. Energy Information Administration (EIA), energy consumption will expand from 549 quadrillion British thermal units (Btu) in 2012 to 815 quadrillion Btu in 2040, which means a 48% increase from 2012 to 2040 is expected [1]. Currently, traditional fossil fuels, *e.g.* coal, oil and natural gas still supply the majority of the energy use. However, non-renewability characteristic and climate impact of traditional fuels make us have no choice but seek clean sustainable energy to lower down the dependency and even substitute conventional energy sources. In order to solve this pressing problem, a variety of new energy sources and technology are developed by researchers, such as wind, geothermal, biomass, electrochemical power sources and solar cells. Among these, electrochemical power sources present extraordinary merits due to their extensive application in our daily life. Moreover, all these electrochemical power sources are clean and no hazard chemicals produced. Typically, electrochemical power sources consists of supercapacitors, batteries and fuel cells, which can be employed in application ranging from electric vehicles due to their relatively high efficiencies and environmental friendliness. Particularly, supercapacitors exhibit significant advantages beyond batteries and fuel cells in terms of power density, cycle stability and rapid charge-discharge [2] receiving considerable attention for corresponding potential application in heavy transport, vehicles, memory backup and electronic devices [3-7].

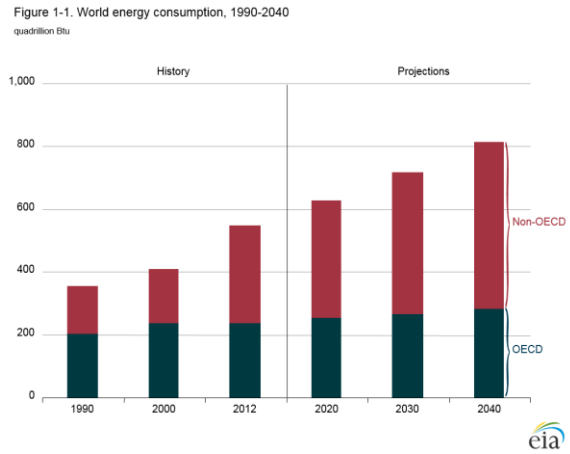

Fig. 1 World energy consumption from 1990 to 2040. Copyright © 2016 U.S. EIA.

Supercapacitor, also called as electrochemical capacitors, can be divided into two major types: pseudocapacitors and symmetric supercapacitors depending on their unique energy storage mechanisms. Pseudocapacitors usually referred as asymmetric capacitors, energy storage originated from reversible redox reactions where happened on the electrodes surface [8]. On contrast, symmetric supercapacitors, also called electrochemical double layer capacitors (EDLCs), store energy *via* reversible ion adsorption and desorption without any faradic reaction [8]. Based on their individual energy storage mechanism, the electrode materials also vary a lot. In regard with electrode materials of pseudocapacitors, metal oxides and composites, *e.g.* manganese dioxide (MnO_2), nickel hydroxide ($Ni(OH)_2$), cobalt oxide (Co_3O_4), ect., [9-12] are extensively used, because of availability of reversible reaction. In terms of EDLCs, carbon materials, such as carbon nano tubes, activated carbon, carbon fiber and graphene are used as electrode materials because of the superior stability of carbon materials in harsh chemical environment [13-16]. Owing to the difference in electrode materials, pseduocapacitors usually possess much higher specific capacitance than that of EDLCs because of its active redox reactions, but much

better cycling stability and life time are showed by EDLCs due to good stability of carbon materials. This work is focused on EDLCs electrode materials.

To obtain high specific capacitance for EDLCs, considerable work has been conducted on developing new carbon materials. As mentioned above, ion sorption and desorption are the energy storage mechanism, thus, the properties of electrode materials-carbon materials are the key factors. Factors of specific surface area (SSA), nanostructures, porosity (micro-, meso-, and macropores), introduction of defects, heteroatom or functional groups, which are in charge of providing accessible active sites [17-19], shortening the diffusion pathways and offering minimized diffusive resistance to mass transport on a large electrode/electrolyte interface [20-22], offering rapid ion transport with improved rate capability [20, 23, 24], and increasing available active sites and effectively modulate their electronic and chemical character [25-28], respectively. Therefore, amount of methods are developed to obtain porous carbon materials with high SSA, and consequently achieve a high specific capacitance for EDLCs.

Among previous reported carbon materials, activated carbon derived from biomass attracted considerable attention because of its abundance, sustainability and low cost [29]. So far, activated carbon derived from banana peel, rice husk, bamboo, human hair, and grape seeds, etc. [30-34] have been reported using as high performance EDLCs electrode materials. In addition, graphene a 2-dimensional single sheet of carbon atoms arranged in a hexagonal network, has become another promising electrode materials for energy storage since it was discovered by scotch tape peeling method in 2004 [35] due to its outstanding physical characteristics of highly ordered, outstanding surface areas (2630 m^2

g^{-1}), high Young's modulus (1 TPa), high thermal conductivity (5000 W mK^{-1}), strong chemical durability and high electron mobility (2.5×105 cm^2 V^{-1} s^{-1}) [36].

In this work, several activated carbon materials are prepared *via* different activation methods and modification technologies, and subsequently using as EDLCs electrode materials. The work is made of 9 sections as following:

Section I Whey-protein-derived nitrogen-doped porous carbon has been prepared by preliminary carbonization at 400 ℃ and final potassium hydroxide (KOH) activation at 700 ℃ combined with catalytic graphitization. Physical characterization indicated that the nitrogen-doped activated electrode material had a large specific surface area (2536 m^2 g^{-1}) and plenty of interconnected cavities, which greatly improved the performance of supercapacitors. Electrochemical measurements demonstrated that the as-prepared activated electrode material had exceptionally high capacitance of 248 F g^{-1} at charge/discharge current density of 0.1 A g^{-1}. Moreover, the prepared supercapacitors exhibited ideal capacitive behavior with nearly no capacitance loss in 6 mol L^{-1} KOH at different charge/discharge current densities ranging from 0.1 to 5 A g^{-1} after 1,000 charge/discharge cycles. The derived energy density was 12.4 Wh kg^{-1} at a power density of 495 W kg^{-1} under operational conditions. These results suggested that the whey-protein-derived porous carbon is a promising supercapacitor electrode material.

Section II Cyanobacteria, as a renewable source of carbon, was used to prepare activated carbon electrodes in supercapacitors. The activation includes a pre-carbonization at 400 ℃ followed by KOH heat treatment at 800 ℃, leading to efficient and high degree of graphitization. The activated carbon electrode consisted primarily of carbon and oxygen, and possessed a large specific surface area of 2184 m^2 g^{-1}, with pore size centered at 27

nm. In 6 mol L^{-1} KOH electrolyte, the electrode exhibited superior specific capacitance of 271 F g^{-1} and 222 F g^{-1} at a charge/discharge current density of 0.1 A g^{-1} and 5.0 A g^{-1}, respectively. The results demonstrated that the activated carbon derived from cyanobacteria can serve as promising electrode material for electrical double-layer capacitors.

Section III N-doped porous carbon materials derived from urea-modified lignin were prepared *via* efficient KOH activation under carbonization. The synthesized N-doped carbon materials, which displayed a well-developed porous morphology with high specific surface area of 3130 m^2 g^{-1}, was used as electrode materials in symmetric supercapacitors with aqueous and solid electrolytes. In consistent with the observed physical structures and properties, the supercapacitors exhibited specific capacitances of 273 and 306 F g^{-1}, small resistances of 2.6 and 7.7 Ω, stable charge/discharge at different current densities for over 5000 cycles and comparable energy and power density in 6 mol L^{-1} KOH liquid and KOH-PVA solid electrolytes, respectively.

Section IV Rod-shape porous carbon was prepared from aniline modified lignin *via* KOH activation and used as electrode materials for supercapacitors. The specific surface area, pore size and shape could be modulated by the carbonization temperature, which significantly affected the electrochemical performance. Unique rod-shape carbon with massive pores and a high BET surface area of 2265 m^2 g^{-1} were obtained at 700 ℃ in contrast to irregular morphology created at other carbonization temperatures. In 6 mol L^{-1} KOH electrolyte, a specific capacitance of 336 F g^{-1}, small resistance of 0.9 Ω and stable charge/discharge at current density of 1 A g^{-1} after 1, 000 cycles were achieved using rod-shape porous carbon as electrodes in an electrical double layer capacitor.

Section V Lignin, an abundant biomass in nature, was modified by pyrrole to produce nitrogen doped porous carbon. The porous carbon was efficiently activated through simultaneous chemical and physical reactions using KOH as activation agent during the heat treatment. Surface area analysis showed that the activated carbon possessed mesopores (~15 nm) and large specific surface area of 2661 m^2 g^{-1} with a cheese-like morphology. Electrochemical double layer capacitors fabricated using the activated carbon as an electrode material showed a specific capacitance of 248 F g^{-1} at low current density of 0.1 A g^{-1} and 211 F g^{-1} at high current density of 10 A g^{-1} in 6 M KOH solution. Charge and discharge for 1,000 cycles at different current densities ranging from 0.1 to 10 A g^{-1} confirmed excellent specific capacitance retention and good cycling stability. This work demonstrated that the nitrogen-doped cheese-like porous activated carbon was a promising electrode material for electric double layer capacitors.

Section VI Nitrogen-doped hierarchical porous carbon has been prepared *via* a direct carbonization of pyrrole modified biomass for using as electrochemical double layers capacitance electrodes materials. The hierarchical porous carbon features high specific area (2959 m^2 g^{-1}) and porosity, which originated from the etching, gasification and intercalation effect during heat treatment. Based on this unique porous structure, specific capacitance of 270 F g^{-1} at low current density of 0.1 A g^{-1} and 232 F g^{-1} at high current density of 10 A g^{-1} was obtained in 6 M KOH electrolyte. Excellent cycles durability was obtained after initial charge/discharge, the high specific capacitance remained nearly unchanged for total 4,000 cycles tested over a broad current density ranging from 0.1 A g^{-1} to 10 A. This study indicates that hierarchical porous carbon derived from pyrrole modified biomass is a promising electrode material for symmetric supercapacitors.

Section VII N incorporated carbon materials are proved to be efficient EDLCs electrode materials. In this work, aniline modified fungus are served as raw materials, N-doped porous activated carbon is prepared *via* efficient KOH activation methods. Porous network with high specific surface area of 2339 m^2g^{-1} are displayed for prepared carbon materials, resulting in high accessible surface area and low ion diffusion resistance which is desired for EDLCs electrode materials. In assembled EDLCs, N-AC based electrode exhibits a specific capacitance of 218 F g^{-1} at current density of 0.1 A g^{-1}. Besides, excellent stability is displayed after continuous 5000 cycles at different current densities ranging from 0.1 to 10 A g^{-1}. The present work reveals a promising candidate of electrode materials for EDLCs.

Section VIII This work demonstrated an efficient plasma exfoliation of graphite oxides to fabricate graphene at room temperature. The microstructure, morphology and composition of the prepared graphene were confirmed by X-ray diffraction, transmission electron microscopy, Raman spectroscopy, and X-ray photoelectron spectroscopy. The plasma exfoliation mechanism was revealed based on the plasma emission spectra. The electrochemical performance of symmetrical electrode supercapacitors made of the plasma exfoliated graphene was tested by cyclic voltammetry, electrochemical impedance spectroscopy, and cycle-life measurement. It was showed that graphite oxide exfoliated by CH_4 plasma led to better specific capacitance and stability than that exfoliated by O_2 and N_2 plasmas. This study provided a new perspective and potentially efficient way to upscaling graphene manufacturing.

Section IX Radio frequency (RF) dielectric barrier discharge plasma was used to exfoliate graphite oxide (GO) into graphene. The GO was synthesized from a modified

Hummers method. The exfoliation occurred swiftly once the RF power and gas pressure reached a level that enabled sufficient energy transfer from the plasma to the GO. X-ray diffraction (XRD) and transmission electron microscopy (TEM) confirmed that graphene or carbon nanosheets were successfully prepared. The plasma exfoliation mechanism was revealed based on the microstructure characterization and optical emission spectroscopy, which indicated that oxygen was released at the moment of exfoliation. Inspired by the success of GO exfoliation, N-doping was realized by treating polypyrrole-modified GO with plasmas. The N concentration in the resulted graphene depended strongly on the plasma gas. Of the gases studied, CH_4 treated polypyrrole-modified GO (GO-PPY-CH_4) contained considerable concentration of N that was beneficial to electrical double layer capacitors (EDLCs). Supercapacitors made of the N-doped graphene exhibited promising capacitive characteristics. Electrochemical measurements showed that the GO-PPY-CH_4 presented an initial specific capacitance of ~312 F g^{-1} under 0.1 A g^{-1} charge/discharge current and ~100% retention after 1000 consecutive cycles under currents ranging from 0.1 to 10.0 A g^{-1} in 6 mol L^{-1} KOH electrolyte. This study demonstrated that the plasma exfoliation was an efficient approach to fabricating graphene and N-doped graphene that had promising potential to be high-performance electrode materials for EDLCs.

Chapter 2 Nickel catalytic graphitized porous carbon as electrode material for high performance supercapacitors©

2.1 Introduction

The increasing demand for high power energy storage devices has attracted significant attention on supercapacitors that feature high power density, long lifetime, and fast charge/discharge [1-3]. Based on their working mechanism, supercapacitors are classified into two major types: pesudocapacitor and electric double-layer capacitors (EDLCs). Pseudocapacitors use rapid reversible redox reactions at the surface of electrode materials and offer high specific capacitance. In pseudocapacitors, metal oxides such as NiO, CoO and MnO_2 are commonly used as the electrodes [4-6]. In contrast, EDLCs store charge electrostatically by forming a double layer of electrolyte ions on the surface of conductive electrodes. Activated carbon-based materials are the most common electrodes in EDLCs. The desired properties for the carbon electrodes are high electrical conductivity, large specific surface area (SSA) with accessible porosity, and low cost [7-9].

Graphene has a theoretical specific capacitance of about 526 F g^{-1}, however, only 25.7% to 39.0% of this potential was achieved in experiments [10]. This large discrepancy has stimulated intensive research activities to improve the specific capacitance of carbon-based materials. In 2009, Dai *et al.* enhanced the performance of carbon based electrocatalysts by introducing nitrogen (N) in carbon-based materials increase electrical conductivity [11]. Inspired by N introduction effects, varieties of doping methods were

developed and applied into EDLCs. One of their approaches to adding nitrogen in carbon-based materials was to use N-rich organic chemicals (pyrrole, aniline, melamine and ethylenediamine) [12-15] to modify the properties of carbon materials, including carbon nanotube (CNT) and graphene. However, these materials were neither eco-friendly nor cost effective. Another strategy to produce N-doped carbon materials was to carbonize the nitrogen containing precursors, such as yogurt, coconut shell, grape seed, distillers dried grains and so forth [16-20]. This approach offered significant advantages in that it did not use toxic chemicals or produce noxious by-products, and had relatively low cost. Nitrogen in the renewable bio-feedstock sources could be easily immobilized in the carbon matrix during heat treatment, which is much easier and safer than carbon coating using nitrogen containing toxic chemicals.

Recently, N-containing biomass as feedstock for N-doped porous carbon materials for high performance EDLCs had attracted great research interest because of the low cost, sustainability and accessibility. N-doped porous carbon materials must be subjected to a high degree of graphitization to achieve excellent EDLCs performance. Conventional graphitization required high temperatures of 2,500-3,000 ℃ [21] and is therefore, energy intensive and inefficient. Alternatively, catalytic graphitization was a more effective method to produce graphitic carbon. In this method, a transition metal (Fe, Co, or Ni) served as catalyst during pyrolysis process, which led to graphitization temperatures below 1,000 ℃ and the potential of low-cost manufacturing [22]. Inspired by the effects of N doping and catalytic graphitization, the authors studied a whey protein as carbon precursor, in combination with $Ni(NO_3)_2$ as catalyst precursor to produce high-performance EDLC. Whey protein is a homogeneous, free flowing, semi-hygroscopic

powder containing a large amount of N, while Ni was well-known by catalytic function. In this work, the authors found that the Ni catalytic graphitization of whey protein was highly effective and the resulting activated carbon exhibited large specific surface areas with superior capacitive performance.

2.2 Material and methods

2.2.1 Preparation of activated carbon

Whey protein (80 *wt*%) in the form of a homogeneous, free flowing and semi-hygroscopic powder was obtained from the Dairy Science Department, South Dakota State University. To prepare the activated carbon, whey protein was mixed with nickel nitrate hexahydrate ($Ni(NO_3)_2 \bullet 6H_2O$, Fisher Scientific) in a mass ratio of 14:1. The mixture was then placed into a steel crucible and heated at 400 ℃ for an hour in a muffle (1100 box furnace, Lindberg/Blue M, Thermo Scientific) under a continuous flow (96 ml min^{-1}) of pure nitrogen gas. After this heat treated material was cooled down, it was mixed with potassium hydroxide (KOH, Fisher Scientific) in a mass ratio of 1:3. To facilitate the mixing process, 20 mL deionized water was added to the mixture. The final mixture was first dried at 110 ℃ for 24 hours and then transferred into muffle to anneal at 700 ℃ for 1 hour under a continuous flow (96 ml min^{-1}) of pure nitrogen gas. These annealed carbon samples were allowed to slowly cool to room temperature and washed with 0.1 mol L^{-1} hydrogen chloride (HCl, Fisher Scientific) at 110 ℃ for 1 hour in a 60 mL polytetrafluoroethylene (PTFE) autoclave to remove the residual KOH and impurities after it was cooled to room temperature. The sample was finally washed several times

with deionized water until the pH reached 7, and was then dried for 12 hours at 105 ℃ overnight in an oven. This final product was called “activated carbon”.

2.2.2 Preparation of original carbon

For comparison, carbon materials were also prepared from whey protein following the same procedure used in the preparation of the activated carbon. The difference was no nickel nitrate and potassium hydroxide. This final product is called “original carbon”.

2.2.3 Preparation of activated carbon without Ni catalyst

Carbon materials were prepared from whey protein following the same procedures used in the preparation of the activated carbon. The difference was no nickel nitrate was introduced. This final product was called “K-activated”.

2.2.4 Fabrication of electrodes

Electrodes were prepared by pressing the slurry of activated or original carbon (80 *wt*%) with acetylene black (10 *wt*%) and PTFE (10 *wt*%) on nickel foam (EQ-bcnf-16m, MTI Corporation) that had a surface area of 1 cm^2. The electrodes were then dried under 60 ℃ for 12 hours in an oven. Afterwards, a sandwich structure was formed by introducing two pieces of microporous polypropylene (PP) separator celgard-3501 between two electrodes, and assembling into a 2032 coin-type cell. The pressing pressure to form the coin cell was 1,000 kg cm^{-2}.

2.2.5 Physical characterization

The crystalline structure of the original and activated carbon samples was investigated by X-ray diffraction (XRD) a Rigaku MiniFlex (Japan) with filtered Cu-K_α radiation (30

kV, 15 mA). Sample composition was analyzed using an SSX-100 system (Surface Science Laboratories, Inc.) equipped with a monochromated Al- K_α X-ray source, a hemispherical sector analyzer (HSA) and a resistive anode detector. For high resolution data, the lowest binding-energy C 1s peak was set at 285.0 eV and used as the reference for all of the other elements. The Raman spectrum was obtained on a Horiba LABRam confocal Raman microscopean with excitation wavelength at 532 nm from a diode pumped solidstate laser. Physisorption analyses with N_2 were carried out at 77 K (liquid nitrogen bath), using a Tristar 3000 Micropore analyzer. The specific surface area was determined by Brunauer -Emmett-Teller (BET) method and the pore size distribution was calculated according to the density functional theory (DFT) method using the nonlocal density functional theory (NLDFT) analysis model for carbon with slit pore model (Micromeritics Inc.). Transmission electron microscope (TEM) was conducted on a JEM-2100 LaB6 STEM.

2.2.6 Electrochemical characterization

Cyclic voltammetry (CV) and electrochemical impedance spectroscopy tests were carried on an electrochemical work station (SP-150, BioLogical, France) in 6 mol L^{-1} KOH electrolyte. The galvanostatic charge/discharge curves were measured using a BTS series battery test system (NEWARE, China).

2.3 Results and discussion

The N_2 sorption-desorption isotherms of original and activated samples were shown in Fig. 2a. The BET specific surface area increased from 146 m^2 g^{-1} to 2536 m^2 g^{-1} after activation at 700 ℃. The KOH corrosion of the bio-carbon created a large number of pores that were responsible for the significant increase in the specific surface area. As

shown in Fig. 2b, the pore size centered on 32 and 21 nm for original and activated samples, respectively, indicating most of pores belong to mesoporous.

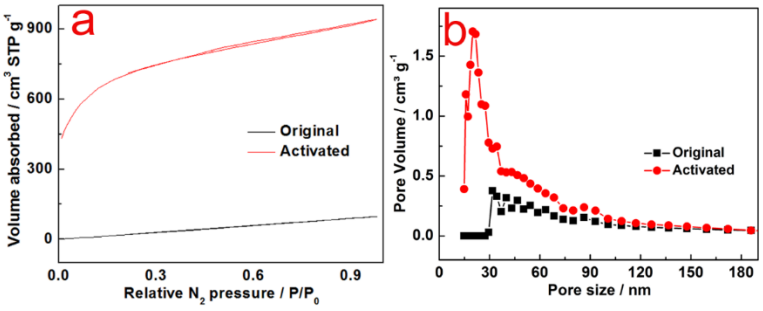

Fig. 2 N_2 sorption-desorption isotherms (a) and pore size distribution (b).

XRD patterns of the original and activated samples are shown in Fig. 3. The original sample exhibited a peak at ~25 °, corresponding to the diffraction from (002) planes of graphite according to the standard pattern for carbon [21]. On the other hand, the activated sample yielded a broad and weak (002) peak, which indicated the presence of amorphous phase. This peak showed a negative shift. Furthermore, the activated sample showed a diffraction peak at 43.5° [22], corresponding to (101) plane. These results clearly indicated that significant changes in the crystal structure and the grain size occurred after activation. The observed changes were attributed to the high-density pores in the activated sample.

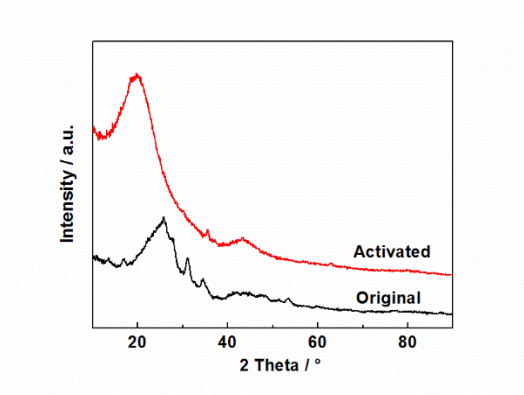

Fig. 3 Wide-angle XRD pattern for original and activated sample.

To further understand the activation effect observed in BET and XRD analysis, TEM studies of both original and activated samples were performed (Fig. 4). The original sample had some degree of graphitization without any porous structure (Fig. 4a and b). On the other hand, the activated sample exhibited a complete different morphology, with a high number of interconnected cavities developed from preferential etching by KOH in the amorphous portions of the carbon as displayed in Fig. 4c and d [23]. These results were in good agreement with the data of XRD and nitrogen adsorption analysis. The pores could serve as reservoirs for electrolyte, and therefore shorten the diffusion distance from the external electrolyte to the interior surfaces of electrode materials [24]. The distinct pore structures were further confirmed using tomography to reconstruct the 3-D structure (see attached supporting information, which is a movie showing the full range pore structures. In addition, selected area electron diffraction (SAED) was used to study the degree of crystallinity. The original sample showed faint light rings caused by a mixture of crystalline and amorphous phases, while the activated sample showed a well-defined dot matrix, indicating good crystallinity with very small crystals.

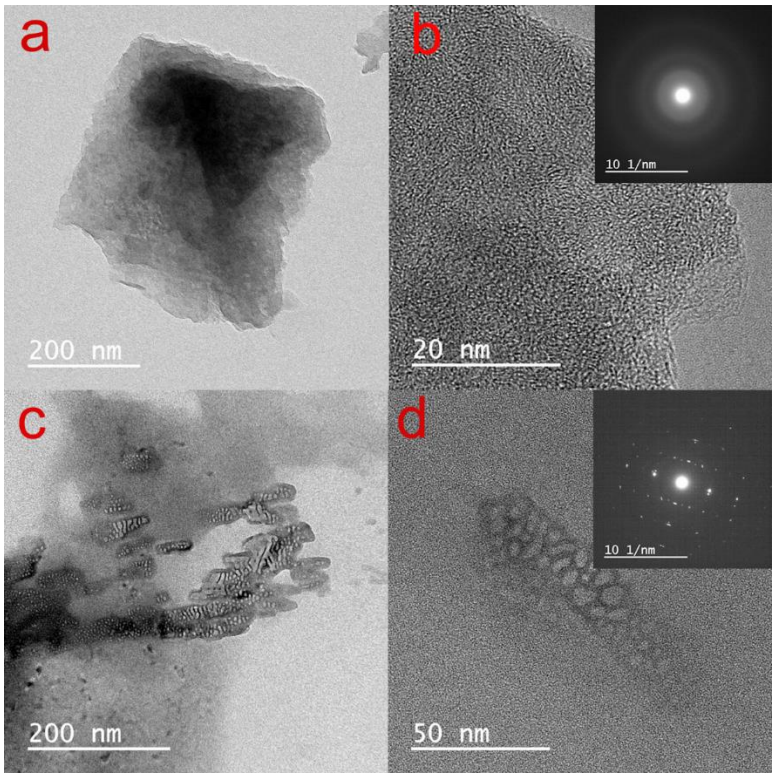

Fig. 4 Different magnifications TEM images of original (a, b) and activated (c, d). Inset in (b) and (d) shows SAED for original and activated, respectively.

The structural difference between the original and activated samples was also confirmed by Raman spectroscopy. As shown in Fig. 5a, the featured *D*-band and *G*-band peaks were displayed in both samples. The *D*-band located at 1340 cm^{-1} was attributed to the disordered graphite with A_{1g} symmetry. The *G*-band centered at 1580 cm^{-1} corresponded to the first-order scattering of the E_{2g} mode of sp^2 carbon domains [25]. Meanwhile, the ratio of intensity between *D*-band and G-band (I_D/I_G) represented the degree of graphitization, a lower value means the higher degree of graphitization [25]. The I_D/I_G values for the original and activated samples were 0.85, and 0.83, respectively, suggesting that there was higher degree of graphitization in the activated sample. This

was likely due to the contribution of $Ni(NO_3)_2$ which acted to catalyze graphitization in the pyrolsis process [26, 27].

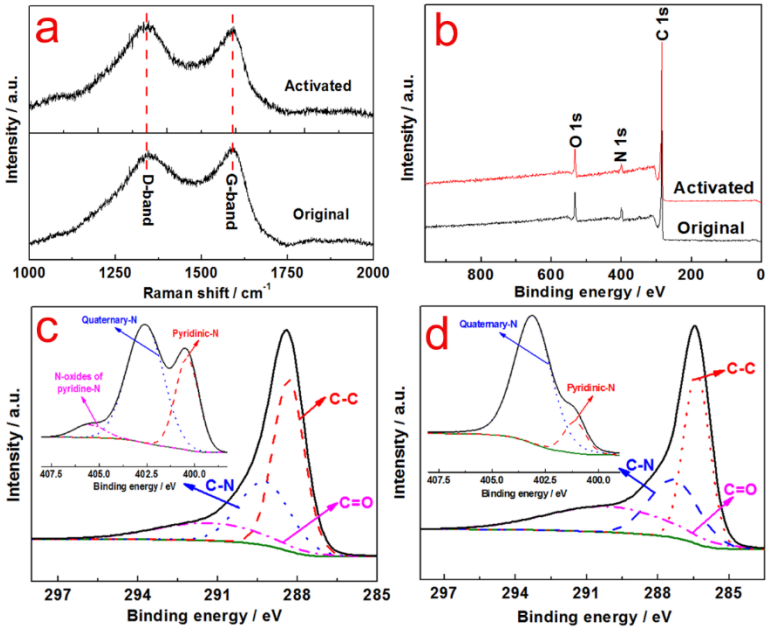

Fig. 5 Raman spectra of original and activated (a); XPS survey spectra (b) of original and activated. C 1s XPS spectra of original (c) and activated (d); Inset in (c) and (d) shows N1s XPS spectra of original and activated, respectively.

To clarify the effects of Ni on the chemical state of N in the original and activated samples, X-ray photoelectron spectroscopy (XPS) measurement (Fig. 5b, c and d) were performed. As shown in Fig. 5b, the full range XPS survey spectra of both samples contained signals from C, N and O, indicating the ingredient of the two samples. Based on the XPS analysis, the atomic content of C, N and O for activated and original sample was 82.8, 7.04, 8.67 and 88.7, 3.5, 7.8, respectively. Since XPS technique was surface analysis, further elemental analysis was performed to evaluate the buck content of N. The results showed that the content of N for the activated sample was 0.41%, which was

lower than that of original sample (2.68%). The bonding configurations of the carbon and nitrogen were characterized by high resolution C 1s and N 1s spectra (Fig 5c and d). For the C 1s spectrum, three characteristic peaks at approximately 285 eV, 285.9 eV and 288 eV were observed and, were assigned to C-C, C-N and C=O bonds, respectively [28]. For N 1s spectrum, N species in activated sample were pretty different from that in the original sample. The high resolution N 1s spectrum of the original sample could be deconvoluted into three peaks, including pyridinic-N (~398.7 eV), quantum-N (~400.9 eV), and N-oxides of pyridine-N (~403.8 eV) [29, 30]. However, only two types of N (pyridinic-N, quantum-N) were observed in the activated carbon samples, implying that the N-oxides of pyridine-N was either lost with the removal of Ni by HCl washing or transformed into quantum-N and pyridine-N. As it has been proved that transition metals Fe and Co could form FeN_x and CoN_x [31, 32] composite during the process of plyolysis under the introduction of N-containing substance rather than Ni. On the other hand, $Ni(NO_3)_2$ decomposed into Ni oxides that was subsequently reduced into metallic Ni by amorporous C at elevated temperatures [33, 34]. Due to random diffusion effect [35], C-Ni interaction [36], mutual action between Ni nanoparticles [37], external forces (e.g. gravity) or a combined role of multiple factors, the Ni nanoparticles deposited on the surface of carbon tended to move in the surface carbon matrix, modifying the amorphous carbon to produce quasi-graphitic nanostructures according to “dissolution-precipitation” mechanism. Meanwhile, unsaturated dangling bonds located at the edge of nascent carbon nanostructures resulted in the formation of an integrated carbon structure. The contribution of Ni in graphitization was likely that the N-oxides of pyridine-N was transformed into quantum-N, also named as graphitic-N. This tranformation was

expected to enhance the performance of EDLC, because a report indicated that the pyridine-N configurations induced pseudocapacitance enhancement while the quantum-N configuration improved the conductivity of carbon materials [30].

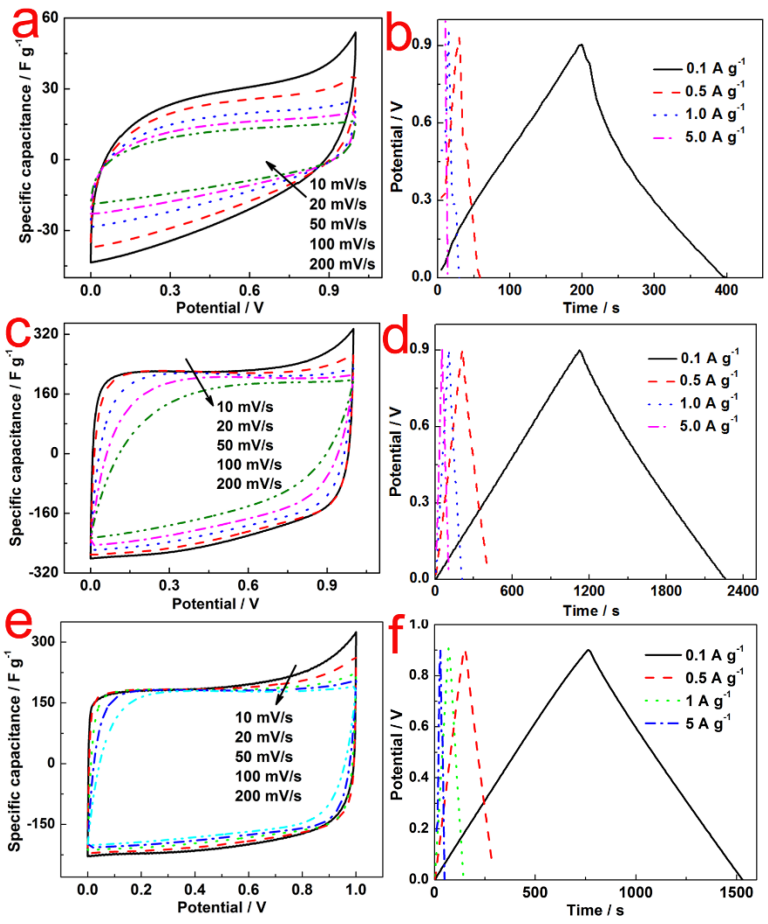

Fig. 6 CV curves of (a) original, (c) activated and (e) K-activated electrodes at various scanning rates ranging from 10 to 200 mV s^{-1}; Galvanostatic charge/discharge curves of (b) original, (d) activated and (f) K-activated electrodes at different current density ranging from 0.1 to 5 A g^{-1}.

The electrochemical properties of the original and activated samples were measured in 6 mol L^{-1} KOH electrolyte with a two-electrode cell system at room temperature using a

SP-150 BioLogical electrochemical work station. Fig. 6a, c and e showed the CV measurement results of the original, activated and K-activated electrodes at various scanning rates ranging from 10 to 200 mV s^{-1}. The CV curve of the activated electrode exhibited a typical rectangular shape at all scanning rates in contrast to that of the original. These results implied that, due to the contribution of Ni catalytic graphitization, the activated electrode possessed a better capacitive performance and electrical conductivity than that of the original electrode.

The specific capacitance of the original and activated electrodes was calculated by the following equation [16]:

$$C = \frac{2I\Delta t}{m\Delta v} \quad (1)$$

where C, I, Δt, m, Δv are the specific capacitance, the charge/discharge current, the corresponding charge or discharge time, the mass of active materials on single electrode, and the total corresponding potential change, respectively. As shown in Fig. 6a, c and e, the activated electrode had specific capacitance of 200 - 248 F g^{-1} from 10 mV s^{-1} to 200 mV s^{-1}, which is pretty better than that of K-activated (153 - 168 F g^{-1}) and original electrode (20 - 44 F g^{-1}). In addition, compared with other carbon based electrode materials, such as hierarchical porous carbon (294 F g^{-1}) [38], N-doped porous carbon (245 F g^{-1}) [39], N-Doped ordered mesoporous carbon (227 F g^{-1}) [40], and N-modified few-layer graphene 227 (F g^{-1}) [41], the prepared activated electrode materials exhibited comparable or even better performance at similar measurement condition for symmetric supercapacitors.

The galvanostatic charge/discharge curves of original and activated electrodes at different current densities of 0.5, 1.0, 2.0 and 5.0 A g^{-1} were shown in Fig. 6b, d and f, respectively. For the activated electrode, the shape of the curves was almost typical isosceles triangular and highly linear, indicating that the electrode material had ideal capacitive characteristics and excellent electrochemical reversibility. In contrast, the charge/discharge performance of the K-activated and original electrodes deteriorated sharply at increased current density.

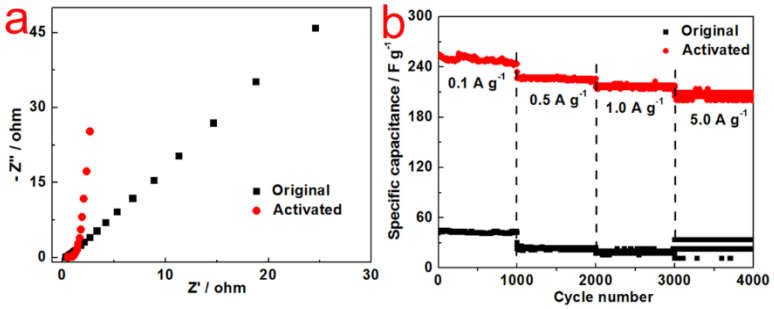

Fig. 7 Nyquist plots of (a) original and activated electrodes; (b) Cycle life of the (b) original and activated electrodes in 6 mol L^{-1} KOH electrolyte at different current density ranging from 0.1 to 5 A g^{-1}.

Fig. 7a showed the electrochemical impedance spectroscopy results measured in the range from 0.1 to 100 kHz in the two-electrode cell. The *x*-intercept donated as equivalent series resistance (ESR) R_s, a semicircle and a 45° phase shift line appeared at the high and low frequency region, respectively. Typically, the resistance consisted of bulk electrolyte resistance, interfacial resistance and apparent resistance of intra-particle pores; the first two terms were associated with the electrolyte and the last term was associated with both the electrolyte and electrode materials [42]. The activated electrode displayed slightly larger R_s value (0.55 Ω *vs* 0.34 and 0.13 Ω for original and K-activated

electrodes, respectively), but smaller semicircle at the high frequency region and a more s line at the low frequency region than that of original and K-activated electrodes, suggesting the activated electrode generally had better conductivity than original and K-activated electrodes. These results were attributed to i) the pores serving as ion-buffering reservoirs that shortened the ion diffusion distance from the external electrolyte to the interior surfaces; ii) the thinner walls of carbon framework enhanced the diffusivity of the ions in the pores [21, 24].

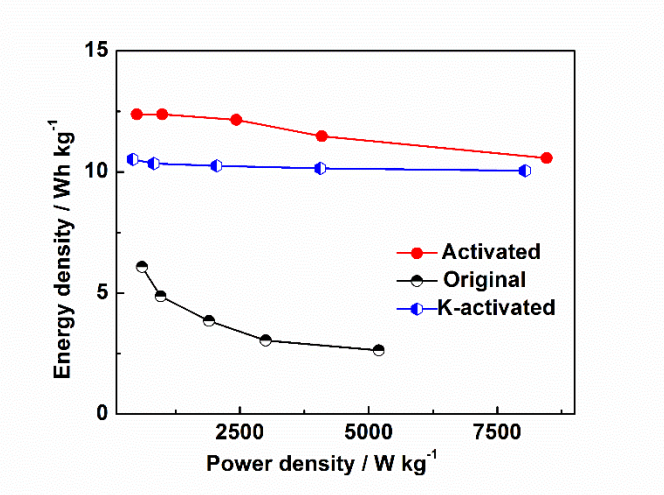

Fig. 8 Ragone plots of the original, K-activated and activated electrodes.

The long-term stability of the EDLC was verified through cycle-life tests, which were conducted in 6 mol L^{-1} KOH electrolyte at different current densities ranging from 0.1 to 5 A g^{-1}. As shown in Fig. 7b, after 4,000 cycles at different current densities, the activated electrode retained 84% of its specific capacitance upon increasing the current density from 0.1 A g^{-1} to 5 A g^{-1}, which behaved much better than original and K-activated electrodes. Within 1,000 cycles at different current densities, the activated electrode did not exhibited capacitance loss and the specific capacitance was much larger than that of original and K-activated electrode. The high specific capacitance and good

stability were due to the enhanced conductivity and large amount of interconnected pores, as verified by the TEM characterization.

To demonstrate the operational characteristics, the energy and power densities were calculated according to the following equations [38]:

$$E = \frac{1}{2} C(\Delta \mathrm{V})^2 \tag{2}$$

$$P = \frac{E}{t} \tag{3}$$

where E is the average energy density (Wh kg^{-1}), C is the specific capacitance of the symmetric supercapacitor, $\Delta \mathrm{V}$ is the voltage range, P is the average power density (W kg^{-1}) and t is the discharge time, respectively. Ragone plots of the original, K-activated and activated electrodes was shown on Fig. 8. The energy density of the activated electrode reached 12.4 Wh kg^{-1} at a power density of 495 W $kg^{-1}$and still remained 10.6 Wh kg^{-1} at a power density of 8.5 kW kg^{-1}, which was higher than that of original (6.1 Wh kg^{-1} at 600 W kg^{-1} and 2.65 Wh kg^{-1} at 5.2 kW kg^{-1}) and K-activated (10.5 Wh kg^{-1} at 420.8 W kg^{-1} and 10.5 Wh kg^{-1} at 8.1 kW kg^{-1}) electrodes. The above results indicated that Ni catalytic graphitization greatly boosted the electrochemical performance and EDLCs devices with excellent electrochemical stability and cyclability could be obtained using the activated carbon electrode.

2.4 Conclusion

In summary, high performance EDLC electrode materials were derived from whey protein by the combination of efficient KOH activation and Ni catalytic graphitization during pyrolysis. The prepared carbon electrodes had high specific surface area, high porosity, and N doping. These characteristics led to efficient diffusion of charges and

increased electrical conductivity, which contributed to large specific capacitance of 248, 227, 217 and 210 F g^{-1} at current densities of 0.1, 0.5, 1.0, and 5.0 A g^{-1}, respectively. Furthermore, the activated electrodes possessed excellent cyclic stability with specific capacitance retention of ~100% after 1,000 charge/discharge cycles at each current density. Moreover, higher energy density of 12.4 Wh kg^{-1} was achieved at a power density of 495 W kg^{-1} for the prepared electrodes. These results confirmed that the whey-protein-based activated electrode is a potential candidate for high performance EDLCs.

Chapter 3 Pyrolytic cyanobacteria derived activated carbon as high performance electrode in symmetric supercapacitor©

3.1 Introduction

Carbon materials are widely used as electrode materials in electric double layer capacitors (EDLC) [37], due to their high electric conductivity and excellent tolerance to various electrolytes. EDLC, stores energy by reversible adsorption of ions at the interface between electrolyte and active electrode materials. Currently, carbon black, single and multiwall carbon tubes and graphene are the predominant materials used in EDLC [38, 39]. However, these materials have several drawbacks, such as low specific surface area (SSA) and high cost, which limit their potential applications. The capacitance of EDLC is closely related to three factors: i) accessible SSA of the electrode; ii) type of the electrolyte; and iii) effective thickness of the double layer. These factors are illustrated in the formula below [40]:

$$C = \frac{\varepsilon_r \varepsilon_0 A}{d} \tag{4}$$

where C (F) is the capacitance of the EDLC, ε_r (F m^{-1}) is the dielectric constant of electrolyte, ε_0 (F m^{-1}) is the dielectric constant of vacuum, d (m) is the effective thickness of the double layer, and A (m^2) is the electrode surface area. It should be noted that only the surfaces that are accessible to the electrolyte ions can contribute to charge storage. Therefore, optimization of the pore size, pore structure, surface properties and conductivity of the electrode materials is required [40].

Carbon materials derived from biomass are promising candidates for EDLC electrodes due to their materials' abundance, low cost, sustainability and possible large SSA. Activated carbon produced from biomass can be divided into two groups: physically activated and chemically activated. Physically activated carbon is obtained by treating biomass with steam or CO_2 under a prescribed temperature, while chemically activated carbon is prepared by exposing biomass to activating agent (*e. g.* KOH, H_3PO_4, $ZnCl_2$) at high temperatures [41-44]. Physical activation typically results in activated carbon with larger SSA. Chemical activation typically results in activated carbon with greater amount of surface functional groups. Both of these characteristics would enhance EDLC performance. Therefore, various naturally abundant biomass and bio-waste have been studied for supercapacitor electrodes [45, 46].

Cyanobacteria are phototrophic bacteria that exist in many ecosystems across the planet. They have existed on Earth for approximately 3.5 billion years, and are a key contributor to global photosynthesis. However, not all cyanobacterias are beneficial to environment and human health; some cyanobacteria grow and expand too fast , destroying fresh water and creating toxins [47]. In recent years, the rapid and efficient photosynthetic system of cyanobacteria has been re-directed by metabolic engineering to produce third-generation biofuels and long-chain hydrocarbon intermediates [48, 49]. Furthermore, cyanobacteria has been recognized as the most promising source of biomass for producing next generation biofuel because it can be easily grown in recirculating photobioreactors fed with CO_2 and powered by sunlight [50, 51] without competing for crop land and fresh water [52]. In most current and proposed cyanobacteria bioenergy or biofuel platforms, cyanobacteria biomass is left as waste after harvesting lipid based biodiesel or volatile

biofuels. Therefore, utilization of cyanobacteria biomass as feedstock for advanced materials or other high value products must be developed. Due to the abundance and accessibility of cyanobacteria, it is attractive to verify the suitability of converting this biomass into active carbon for energy storage. To our knowledge, no research has been attempted to use cyanobacteria for supercapacitors electrodes but seaweeds and microalgae [53, 54]. The goal of this work was to evaluate cyanobacteria as a renewable source of carbon to create EDLC electrodes and transform the waste into efficient energy storage materials. In this work, we first activated cyanobacteria biomass *via* KOH chemical treatment, and then used the activated carbon to prepare EDLC electrode. We systematically evaluated the materials structures and properties (*e. g*. SSA, pore size, electric conductivity, and surface functional groups) that accounted for the promising EDLC performance.

3.2 Experimental

3.2.1 Preparation of activation and original carbon

All reagents were purchased from Fisher Scientific Incorporation. Cyanobacteria cell mass was obtained from Biology and Microbiology department of South Dakota State University. To prepare the activated carbon, 10 g dried cyanobacteria powder was heated to 400 ℃ for 1 h in a muffle furnace (1100 box furnace, Lindberg/Blue M, Thermo Scientific Inc.) using N_2 as inert carrier gas (flow rate was 96 ml min^{-1}) to complete the pre-carbonization. After the carbonized material was cooled to room temperature, it was mixed with activation agent KOH in a mass ratio of 1:3 in a steel crucible. To obtain a uniform mixture, 30 mL deionized water was also added. The mixture was left in the crucible and dried in an oven with stirring every 20 mins at 110 ℃ for 24 h. Then, the

crucible was transferred into a muffle and annealed at 800 ℃ for 1 hour under a N_2 flow rate of 96 ml min^{-1}. Afterwards, the activated carbon was washed with deionized water to remove the extra KOH for several times till pH equals 7. After this, the sample was hydrothermally treated with 0.1 mol L^{-1} HCl at 110 ℃ for 1 h in a 50 mL polytetrafluoroethylene (PTFE) autoclave to remove the residual KOH and other impurities. Finally, the material was washed several times with deionized water again till to pH stabilized at 7. The obtained material was dried at 105 ℃ for 12 h in an oven and denoted as activated carbon (AC). For comparison, the original carbon (OC) materials were also prepared in the same way, except the KOH treatment was omitted.

3.2.2 Preparation of electrodes

Electrodes were prepared by mixing 80 *wt*% AC or OC with 10 *wt*% acetylene black (that to improve the conductivity, and 10 *wt*% PTFE served as binder, and then pressing onto nickel foam current collector (EQ-bcnf-16m, MTI Corp.) of a surface area of 1 cm^2. The electrodes were dried at 60 ℃ overnight in an oven. Afterwards, a sandwich structure was formed placing two pieces of microporous PP separator celgard-3501 between two electrodes in a cell 2032 coin-type system. Finally, the cell was pressed under a pressure of 1,000 kg cm^{-2} to finish the assembly.

3.2.3 Physical characterization

X-ray photoelectron spectra (XPS) was obtained using a SSX-100 system (Surface Science Laboratories, Inc.) equipped with a monochromated Al K_α X-ray source, a hemispherical sector analyzer (HSA) and a resistive anode detector. For high resolution data, the lowest binding-energy C 1s peak was set at 285.0 eV and used as the reference for all of the other elements. Raman spectrum was obtained on a Horiba LABRam

confocal Raman microscopean with excitation wavelength at 532 nm from a diode pumped solidstate laser. Isothermal adsorption analyses with N_2 were carried out at 77 K (liquid nitrogen bath), using Tristar 3000 Micropore analyzer. The specific surface area was determined by the Brunauer-Emmett-Teller (BET) method and the pore size distribution was calculated by the density functional theory (DFT) method using NLDFT analysis for carbon with slit pore model (Micromeritics Inc.) Transmission Electron Microscope (TEM) (Talos F200X, FEI Inc.) equipped with energy-dispersive X-ray spectroscopy (EDX) was used to study the morphology, microstructure, and elemental mapping of the materials at an acceleration voltage of 80 kV.

3.2.4 Electrochemical characterization

Cyclic voltammetry (CV) and electrochemical impedance spectroscopy measurements were performed on an electrochemical work station (SP-150, BioLogical, France) in 6 mol L^{-1} KOH electrolyte. The galvanostatic charge/discharge curves were obtained from BTS series battery test system (NEWARE, China).

To evaluate the specific capacitance in the two-electrode system, the following equation [55] was used:

$$C = \frac{2I\Delta t}{m\Delta v} \tag{5}$$

where C (F g^{-1}) is the specific capacitance, I (A) is the charge/discharge current, Δt (s) is the corresponding charge or discharge time, m (g) is the mass of active materials on single electrode, and Δv (V) is the total corresponding potential change.

3. 3 Results and discussion

Fig. 9a shows the N_2 sorption-desorption isotherms of AC and pore size distribution in the inset. The AC exhibited an extremely large BET SSA (up to 2184 m^2 g^{-1}) and desirable pore structure. The large SSA means there is a large accessible surface area for the electrolyte, while the narrow pore size distribution (which concentrates at 27 nm) can serve as ion-buffering reservoir and allow the smooth transform of ions [56]. Fig. 9b presents the Raman spectra of AC. Two featured peaks correspond to *D* band (1340 cm^{-1}) and *G* band (1585 cm^{-1}) and these were relate to i) the breaking of the A_{1g} symmetry caused by structural disorder and defects and ii) the in-plane bond –stretching motion of a pair of sp^2 carbon atoms with E_{2g} symmetry, respectively [57].

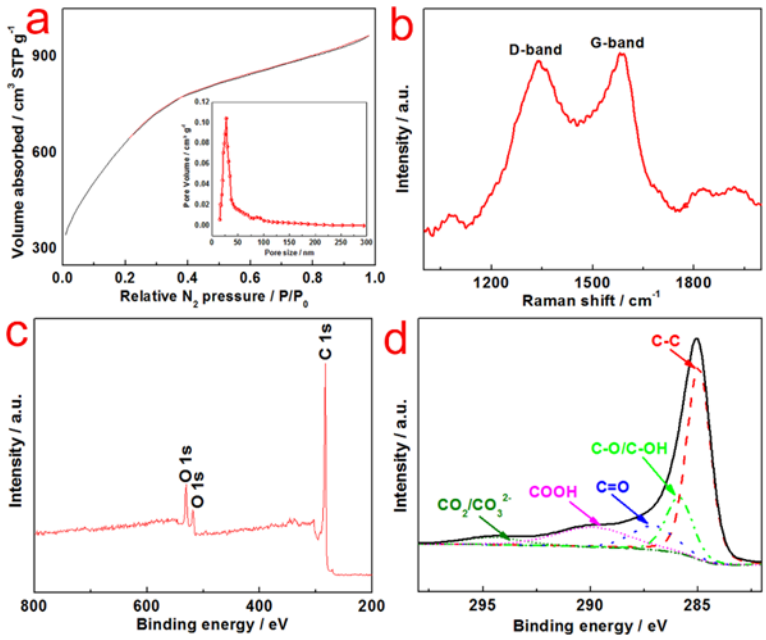

Fig. 9 N_2 sorption-desorption isotherms (a), Raman spectra (b), XPS survey spectra (c) and C 1s XPS spectra of AC (d). The inset in (a) is the pore size distribution plot.

XPS survey was employed to confirm the contained elements and corresponding existing forms. As shown in Fig. 9c, the signals of C and O were detected. The high-resolution XPS spectra of the C 1s region is illustrated in Fig. 9d. The different binding energies indicated that the C atoms were linked to one O atom by a single bond, a double bond, or two oxygen atoms [58]. Deconvolution of the C 1s spectra showed the most pronounced peak being graphite-like carbon (C-C). The peaks located at different binding energies were attributed to different oxygen-containing groups *e.g.*, C-O/C-OH (~286 eV), C=O (~287 eV), COOH (~289 eV), and CO_2/CO_3^{2-} (~294 eV) [59]. These surface functional groups can improve the hydrophilic nature of the AC, thus allowing easy access of the electrolyte to the narrow pores size, which concentrated at 27 nm.

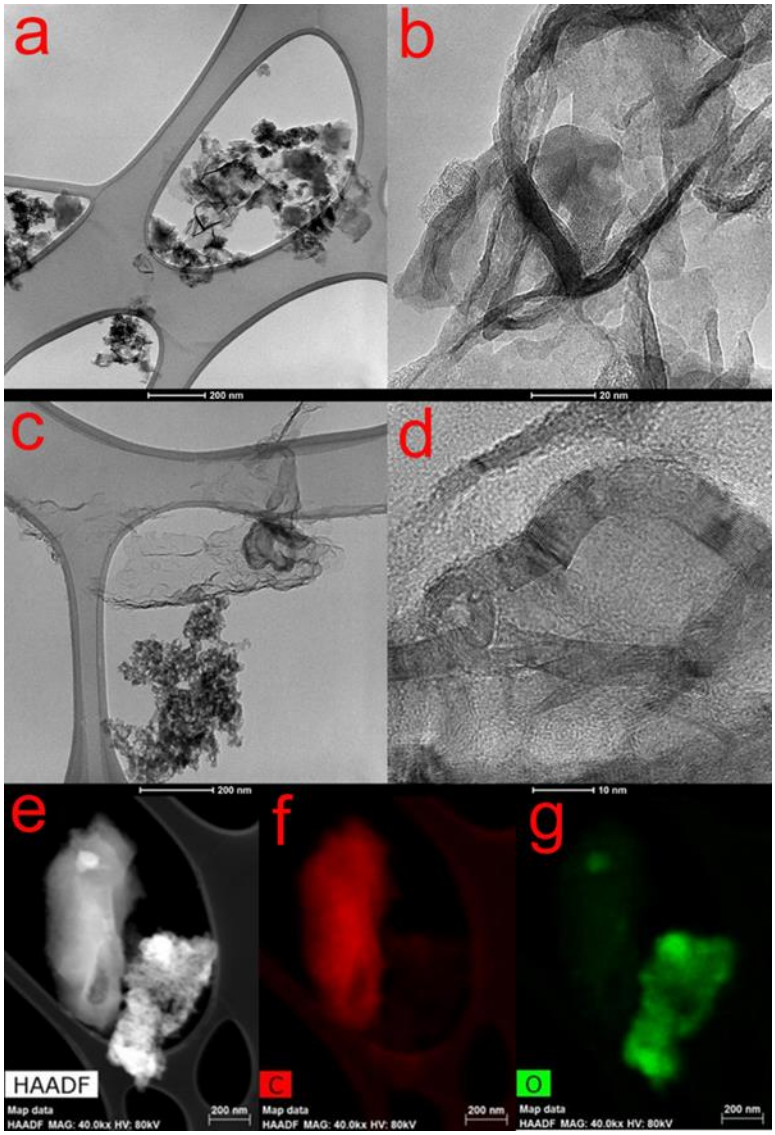

Fig. 10 TEM images of different magnifications for OC (a, b) and AC (c, d), and HAADF-STEM image of spatially resolved EDX elemental maps (e-g) depicting the spatial distribution of the constituting elements within AC: carbon and oxygen maps.

The morphology and content of the AC and OC samples were investigated by TEM. Fig. 10a and b showed that the OC structure had disordered structures that appear overlapped. In contrast, the AC exhibited a narrower pore size distribution, and consisted mostly of graphite (Fig. 10c) and pores (Fig. 10d). The fringes of the graphite crystallite were also

distinctly presented in Fig. 10d, indicating a high degree of graphitization. The significant difference between OC and AC can be assigned to the contribution of KOH, as K and K compounds become intercalated into the carbon lattices of the carbon matrix during activation, resulting in the expansion of the carbon lattices[60]. EDX elemental mapping (Fig. 10e, f and g) depict the spatial distribution of the constituting elements within AC. Both C and O are distributed in the sample, and the ingredients are consistent with the result of XPS survey.

To evaluate the electrochemical performance of the prepared electrodes in assembled supercapacitor. CV, galvanostatic charge/discharge, electrochemical impedance spectroscopy (EIS) and cycle life tests were conducted in a 6 mol L^{-1} KOH electrolyte. The CV curves of OC and AC at various scanning rates ranging from 10 to 300 mV s^{-1} were shown in Fig. 11a and c, respectively. In contrast to OC, AC displayed more rectangular shape, which is an indication of a typical EDLC behavior. A high specific capacitance of 271 F g^{-1} (calculated based on formula 1) was reached at low scan rate of 10 mV s^{-1}, and a capacitance remained as large as 222 F g^{-1} even at a high scan rate of 300 mV s^{-1} for AC electrode. The specific capacitance was much higher than OC at either low or high scanning rate. Therefore, the activation was effective and cause changes (such as specific surface area, porous structure, and degree of graphitization) that greatly facilitated an improvement in the specific capacitance improvement. In addition, compared to the performance of N-doped carbon materials derived from biomass, the AC still exhibited outstanding performance even without N doping (as shown in Table 1).

Table 1 Comparison of specific capacitance of different carbon materials.

Electrode materials	Electrode system	Specific capacitance	Current density	Electrolyte	Reference
N-doped graphene hollow nanospheres	3	381 F g^{-1}	1 A g^{-1}	6 M KOH	[61]
N-Doped ordered mesoporous carbon	3	227 F g^{-1}	0.2 A g^{-1}	6 M KOH	[62]
Porous N-doped hollow carbon spheres	3	213 F g^{-1}	0.5 A g^{-1}	6 M KOH	[63]
N-doped porous carbon	2	245 F g^{-1}	0.05 A g^{-1}	6 M KOH	[64]
N-modified few-layer graphene	3	227 F g^{-1}	1 A g^{-1}	6 M NaOH	[65]
Hierarchical N-doped porous carbon	3	198 F g^{-1}	1 A g^{-1}	6 M KOH	[43]
N-doped porous carbon nanofibers	3	202 F g^{-1}	1 A g^{-1}	6 M KOH	[66]
AC	2	271/222 F g^{-1}	0.1/1 A g^{-1}	6 M KOH	This work

Fig. 11b and d showed the galvanostatic charge/discharge plots at different current densities of 0.1, 0.5, 1.0, and 5.0 A g^{-1} for OC and AC electrodes, respectively. For both materials, the charging and discharging curves were symmetric at the tested current densities, demonstrating that they possesses excellent capacitive reversibility as EDLC electrode. It is noteworthy that there was apparently a large internal resistance drop (*IR* drop) from 0.9 to 0.8 V for both OC and AC electrodes at 0.1 A/g. However, as compared

to OC, AC produced more symmetrical triangle shaped galvanostatic charge-discharge curves with a lower *IR* drop, indicating lower internal resistance and less heat produced from wasted energy during charge /discharge [67].

The electrochemical impedance spectroscopy (EIS) (Fig. 11e) was measured in a frequency range from 100 mHz to 100 kHz to further characterized the resistance for OC and AC. The resistance consisted of bulk electrolyte resistance (0.27 and 0.35 Ω), interfacial resistance (0.57 and 0.3 Ω), and apparent resistance of intra-particle pores (4.1 and 0.7 Ω) [68] for OC and AC electrodes, respectively. These values were determined from the *x*-axis value from the intercept, semicircle and 45° region, respectively. As the resistance rooted from electrolyte, interfaces and pores and was of great importance in energy storage devices, smaller resistance implied better electrical conductivity of the carbon matrix and suitable pore structure for ion transference.

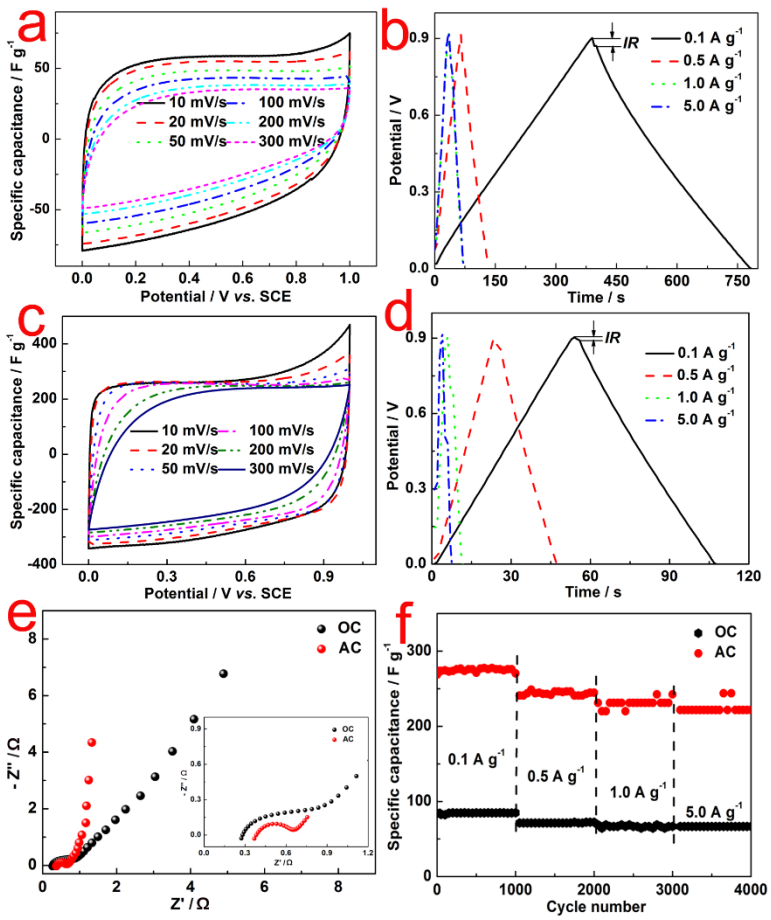

Fig. 11 CV curves (a, c) at various scanning rates ranging from 10 to 300 mV s^{-1}, galvanostatic charge/discharge curves (b, d) at different current density ranging from 0.1 to 5 A g^{-1}, Nyquist plot (e), and cycle life plot (f) at different current density ranging from 0.1 to 5 A g^{-1} for OC and AC electrodes in 6 mol L^{-1} KOH electrolyte, respectively.

Then stability of supercapacitors was yet another significant index to access their performance. The OC and AC electrode at different current densities ranging from 0.1 to 5 A g^{-1} was assessed by the cycle life test (Fig. 11f). The specific capacitance in 1,000 cycles was recorded for each charge/discharge current density. After 1,000 cycles, both OC and AC showed almost 100% retention of specific capacitance at individual charge/discharge current density, indicating superior stability of AC as EDLC electrodes.

However, the specific capacitance of AC was far higher than that of OC. The electrochemical measurements confirmed that cyanobacteria based AC is a promising EDLC electrode material.

3. 4 Conclusions

We have successfully derived activated carbon from cyanobacteria (a bio waste material) *via* chemical activation and demonstrated that the activation carbon can be used as high performance electrodes in supercapacitors. The electrodes resulted in a high specific capacitance of 271 F g^{-1} at a charge/discharge current density of 0.1 A g^{-1}, which is even better than the nitrogen doped carbon electrode. The specific capacitance retention ratio was maintained at almost 100% at each individual charge/discharge current density ranging from 0.1 to 5 A g^{-1}, implying good stability. Considering its extraordinary electrochemical performance in supercapacitors, transformation of bio-waste to energy storage material in this work can inspire more applications into other fields like non-precious electrocatalyst of fuel cell.

Chapter 4 Symmetric supercapacitors using urea-modified lignin derived N-doped porous carbon as electrode materials in liquid and solid electrolytes©

4.1 Introduction

With increasing consumption of energy, considerable attention was paid to new sustainable energy technologies, such as Li-ion batteries, fuel cells, solar cells and supercapacitors. Of these devices, supercapacitors have attracted extensive attention due to their fast charge/discharge rate, long lifetime, and high power density [69-72]. Depending on the working principles, supercapacitors can be divided into two major types: asymmetric supercapacitors and symmetric capacitors. Asymmetric supercapacitors are also referred as pseudocapacitors, which achieve energy storage through a reversible redox Faradic reaction between the electrolyte and electroactive species on the electrode surface. While the accumulation and release of electrostatic charge in the electrical double layer formed at the electrode-electrolyte interface lead to symmetric capacitors, which are also called electrical double layer capacitors (EDLCs). Differing from pseudocapacitors, in which metal oxides (such as NiO, MnO_2, Co_3O_4 and WO_3) [73-76] are widely used as electrode materials, carbonaceous materials are served as electrode materials of EDLCs. As a result, EDLCs have the potential to overcome the common drawbacks of pseudocapacitors, such as unstable cyclicity, poor electrical conductivity and high-cost materials [77].

Achieving high performance EDLCs requires the electrode materials to possess high specific surface area (SSA), porous structure and sustainability. These requirements ensure large accessible contact area between the electrolyte and electrode, suitable

reservoirs to facilitate electrolyte diffusion and channels to smoothly transport ions, and low cost devices, respectively [78, 79]. Traditional carbon materials, such as carbon nanotubes, graphite, carbon fiber, etc., cannot satisfy current demands for specific capacity. Thus, developing new porous carbon materials is a pressing issue to achieve high capacitance EDLCs. To obtain high SSA and porous structures, a variety of methods have been studied, including chemical and physical activation. In comparison with physical activation, chemical activation has more advantages. Generally, chemicals such as KOH, $ZnCl_2$, K_2CO_3 and KCl, etc., are mixed with biochar or carbon materials and pyrolyzed at high temperatures under inert atmosphere [80-82]. At high temperatures, multiple chemical and physical reactions occur, which produce porous structures through etching and gasification effect [83]. Among the reported chemical activation methods, KOH activation is considered the most efficient way.

In addition to the electrode material, electrolyte is another important factor that affects the performance of EDLCs. Conventional supercapacitors use liquid electrolyte, which results in two major issues [84]: 1) high standard safety encapsulation materials are required, leading to large volume and low package energy; and 2) liquid electrolyte supercapacitors suffer from leakage risk; the harsh electrolyte (acid, base and organic [85-87]) is harmful to the environment and even rises fire. These issues restrict the applications of EDLCs. Recently, all-solid supercapacitors using ion gel electrolyte, such as polyvinyl alcohol (PVA)-H_2SO_4, PVA-H_3PO_4, and PVA-KOH, are reported [88-90]. For all-solid supercapacitors, the ion gel not only serve as separator, but also as electrolyte. Wide electrochemical window (0-3.5 V), excellent thermal stability, non-volatility, nonflammability, and non-toxicity are offered by ion gel electrolyte.

Consequently, ion gel electrolyte provides a good solution to the common short-circuit problem in liquid electrolyte EDLCs.

A few recent studies indicated that introducing heteroatoms, such as N and B [91-95] can boost the specific capacitance of EDLCs. Inspired by this idea, the authors speculated that using N-rich chemicals to modify biomass *via* pyrolytic chemical activation would lead to N-contained carbon materials. Consequently, using the N-doped porous carbon as EDLCs' electrode materials would produce high-performance supercapacitors due to the bi-contribution of porous network and N introduction. Although biomass-derived carbon materials are abundant and cheap, N-containing biomass is limited. Therefore, combining N-containing chemicals with biomass can be a promising way to produce carbon materials suitable for supercapacitor electrodes. An attractive example is urea modified lignin. Lignin is a biopolymer representing nearly 30% of the organic carbon on Earth. Over 50 million tons of lignin are produced every year [96, 97], which eventually becomes industrial solid waste and is burned. While urea is widely used as fertilizer because it contains up to 46.67wt% N. Both urea and lignin are cheap, abundant and accessible. Hence, urea-modified lignin can be an ideal raw material to prepare N-doped porous carbon for using as electrode materials in EDLCs.

In this work, N-doped porous carbon was derived from urea modified lignin *via* efficient KOH activation under pyrolysis. The prepared porous activated carbon was subsequently used as EDLCs electrodes in liquid and solid electrolytes, respectively. A variety of physical characterization techniques were employed to confirm the N-rich porous material, which was essentially important to achieving high capacitance. Electrochemical measurement was used to analysis the performance of EDLCs made of the N-rich porous

carbon, which yielded high specific capacitance, excellent stability, low resistance and long life cycle in both electrolytes.

4.2 Experimental

4.2.1 Preparation of activated carbon

Solvent lignin was mixed with urea (Fisher Scientific Inc. USA) in a mass ratio of 1 to 2 first. Proper amount of deionized water was added, while keeping stirring till the urea was dissolved. Then the mixture was placed into an oven at 110 ℃ to dry. The dried powder was transferred into a steel crucible and heated for one hour at 400 ℃ with a heating rate of 10 ℃ min^{-1} in a muffle furnace (1100 box furnace, Lindberg/Blue M, Thermo Scientific Inc.) under the protection of nitrogen (flow rate was 96 ml min^{-1}). After the pre-carbonized material was cooled to room temperature, it was mixed with potassium hydroxide (KOH, Fisher Scientific Inc.) in a mass ratio of 1:3 in a steel crucible that contained 30 mL deionized water. The crucible was placed in an oven and dried at 110 ℃ for 24 h. Then, the crucible was transferred into a muffle and activated at 800 ℃ for 1 h with a heating rate of 10 ℃ min^{-1} under N_2 protection (flow rate was 96 ml min^{-1}). Afterwards, the carbonized solids were washed with 30 mL 0.1 mol L^{-1} HCl (Fisher Scientific Inc. USA) at 110 ℃ for 1 h in a 60 mL polytetrafluoroethylene (PTFE) autoclave to remove the residual KOH and impurities. Finally, the carbon solid was washed with deionized water until the pH stabilized at 7. The material was then dried at 105 ℃ for 12 hours in an oven. The carbonized samples were denoted as L-U.

4.2.2 Preparation of solid electrolyte

PVA (Fisher Scientific Inc. USA) (6 g) with molecular weight of 86000 was added into 100 ml beaker with 60 ml deionized water. The mixture was heated to 100 ℃ and stirred

for 2 h till the PVA was completely dissolved and the mixture became transparent liquid. After that, the temperature was reduced to 85 ℃, while keeping stirring. Then, 6 g KOH was dissolved into 20 ml deionized water and added into the above mixture. Keeping stirring at 85 ℃ till the subsequent mixture became transparent and homogeneous liquid. The prepared homogeneous liquid was poured into a petri dish immediately and the thickness was around 0.5 mm. The petri dish was horizontally placed in atmosphere with a porous cover for 3 days to evaporate the extra water. The prepared thin solid electrolyte was donated as KOH-PVA.

4.2.3 Preparation of electrodes

Electrodes were prepared by mixing the L-U (80 *wt*%) with acetylene black (10 *wt*%) and PTFE (10 *wt*%), and then pressing onto a nickel foam (EQ-bcnf-16m, MTI Corp.) of 1 cm^2 surface area (the loading mass on each nickel foam was ~4 mg). The electrodes were dried at 60 ℃ for 12 h in an oven. Afterwards, a sandwich structure was formed by placing two pieces of microporous Polypropylene (PP) separator celgard-3501 between two electrodes in a coin cell 2032 type system. Finally, the cell was pressed under a pressure of 1000 kg cm^{-2} to finish the assembly. In terms of the all-solid supercapacitors, the same procedure and parameters described above was followed but the separators were substituted by one piece of KOH-PVA with a diameter of 1 cm and thickness ~0.5 mm,

4.2.4 Physical characterization

The surface analysis was performed on a Kratos Axis Ultra high performance X-ray photoelectron spectroscopy (XPS) (Kratos Analytical Ltd.). For high resolution data, the lowest binding-energy C 1s peak was set at 285.0 eV and used as the reference for other elements. Raman spectra were obtained on a Horiba LABRam confocal Raman

microscopy system with excitation wavelength of 532 nm from a diode pumped solid state laser. Isothermal adsorption analysis with dry N_2 was carried out at 77 K (liquid nitrogen bath), using ASAP2020 (Micromeritics Inc.) micropore analyzer. The specific surface area was determined by the Brunauer-Emmett-Teller (BET) method and the pore size distribution was calculated according to the density functional theory (DFT) method using non-local density functional theory (NLDFT) analysis for carbon with slit pore model. A transmission electron microscope (TEM) (JEM-2100 LaB6, JEOL) equipped with energy-dispersive X-ray spectroscopy (EDX) was used to study the morphology and microstructure at an acceleration voltage of 200 kV.

4.2.5 Electrochemical characterization

Cyclic voltammetry (CV) and electrochemical impedance spectroscopy tests were measured on an electrochemical work station (SP-150, BioLogical, France) in 6 mol L^{-1} KOH electrolyte. The galvanostatic charge/discharge curves were obtained from a battery test system (BTS series, NEWARE, China).

4.3 Results and discussion

The morphology and microstructure of L-U were examined by TEM. Fig. 12a showed the images of L-U with different magnification. Plenty of pores with different sizes were observed in low magnification images (Fig. 12a and b), which were dispersed on the carbon chunk randomly. In high resolution images (Fig. 12c and d), hierarchical pore structures were displayed. The macro pores went through the whole carbon chunk, while meso and micro pores were shown around the holes walls. These penetrated pores with different sizes were believed to be originated from KOH activation contribution. As reported by *Kaskel* [83], raw carbon materials were etched due to redox reactions to form

the pores, the produced gas further boosted the formation of porosity and intercalated metallic K in carbon lattice resulted in the expansion of carbon lattices. All these synergistic effects contributed to form porous carbon materials. In addition, the elemental mapping was conducted to confirm the distribution of elements (Fig. 13). It was found that C, O and N elecments were dispersed uniformly in L-U, which would keep the L-U working as superior EDLCs electrodes considering the contribution of N.

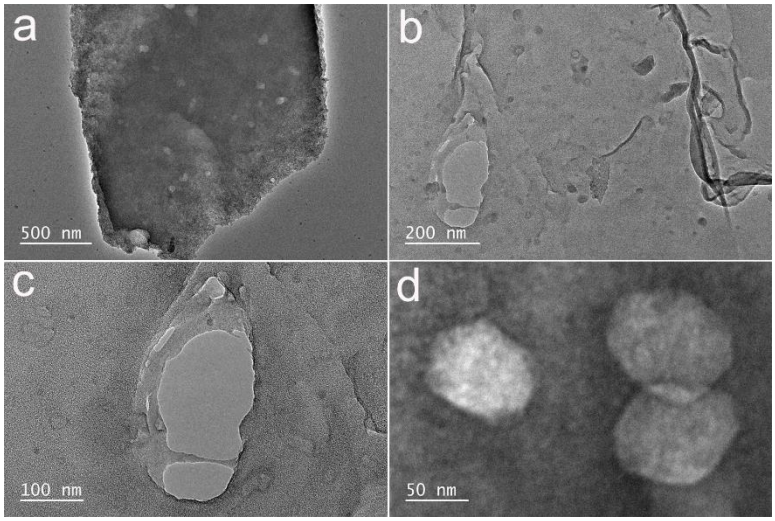

Fig. 12 Different magnifications TEM images of L-U.

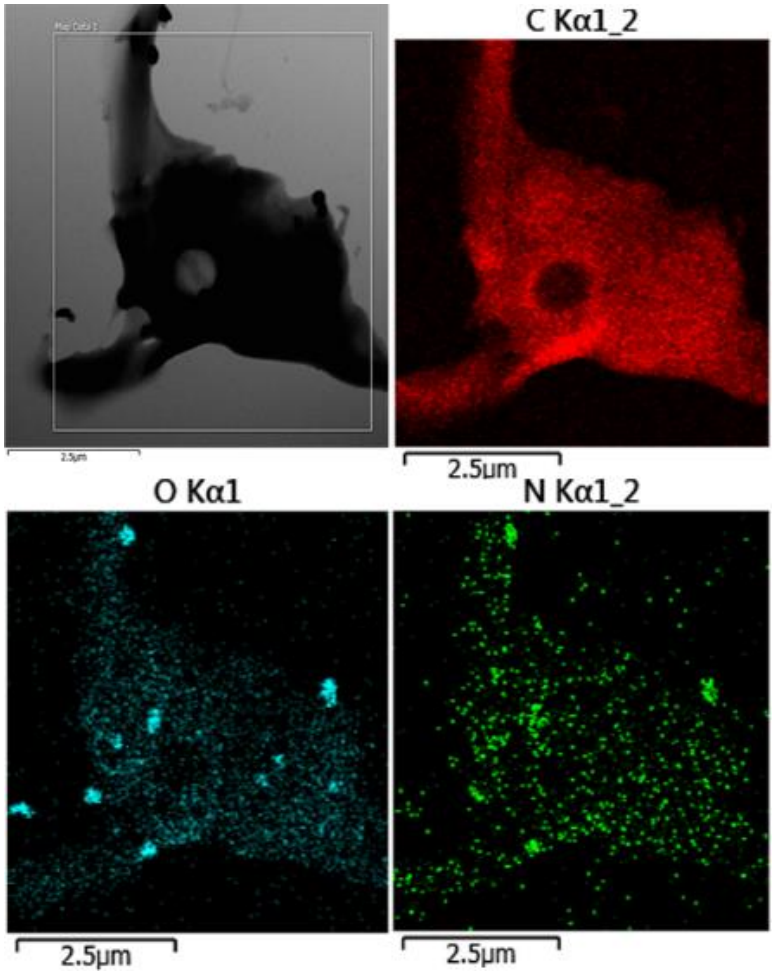

Fig. 13 Elemental mapping of L-U.

The porous structure observed in TEM images implied that the prepared L-U would possess a high surface area. To verify the specific surface area (SSA) and pore size distribution, N_2 sorption-desorption isotherms were employed (Fig. 14a). According to the classification of the International Union of Pure and Applied Chemistry [98], the isotherm belongs to the type I curve. The BET SSA and pore volume reached ~3130 $m^2 g^{-1}$ and 1.67 $cm^3 g^{-1}$, respectively, which was expected to provide large contact area and space between the electrodes and electrolyte. The pore size distribution analysis showed that most of the pores had sizes around 27 nm and there were fewer micropores and

macropores. Such a pore size distribution was reflected by a very weak hysteresis loop at a relative pressure of P/P0 > 0.9 and a steep increase in the adsorbed volume at a very low relative pressure (P/P0 < 0.05), respectively [99, 100]. It is worth to note that all these pores would serve as channels for electrolyte ion transport and result in low resistance. Meanwhile, the pores acted as electrolyte reservoirs to shorten the distance of electrolyte ion transmission [78]. All these features were supposed to improve the capacitance performance of the L-U based EDLCs electrodes.

Raman spectroscopy was carried out to analyze the carbon structure (Fig. 14b). Two characteristic peaks located at ~1348 and 1590 cm^{-1} were observed, which corresponded to *D-band* and *G-band*, respectively. The *D-band* was associated with A_{1g} symmetry assigned to local defects and disorder carbon with sp^3 bonding, while the *G-band* was related to the bond stretching of sp^2-hybridized carbon atoms in rings and chains according to the zone center E_{2g} mode. In addition, the ratio of the intensity of the *D* peak to the *G* peak (I_D/I_G) was used to evaluate the degree of graphitization in carbon materials [101, 102]. The intensity ratio of the signals I_D/I_G for L-U was 0.91, which was smaller than 1, indicating high graphitization degree was obtained.

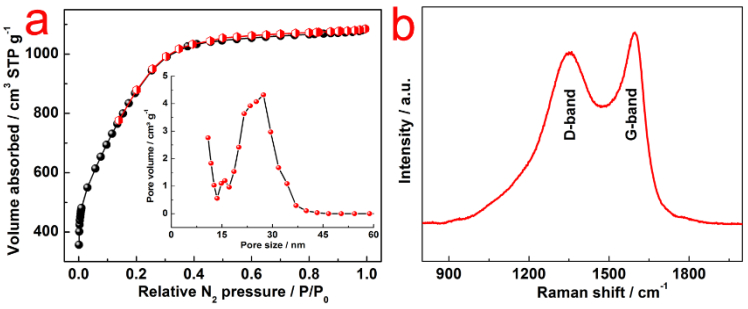

Fig. 14 N_2 sorption-desorption isotherms (a) and Raman spectra (b) of L-U.

The elemental composition and chemical states were investigated by XPS (Fig. 14). In XPS survey analysis (Fig. 15a), signals of C, O and N were detected with atomic contents of 90.4%, 8.4% and 1.3%, respectively. This result was consistent with the TEM elemental mapping and confirmed that N was successfully incorporated *via* thermal annealing. The chemical states of N were studied due to their significant effect on EDLCs performance (Fig. 15b). N 1s spectrum was deconvoluted into two peaks located at binding energy *ca.* 398.9 and 401.2 eV, which were attributed to pyridinic-N and quaternary-N, respectively [103]. It was reported that N introduction would improve the conductivity and pyridinic-N could lead to great pseudocapacitance effect, both would improve the capacitance performance [103, 104].

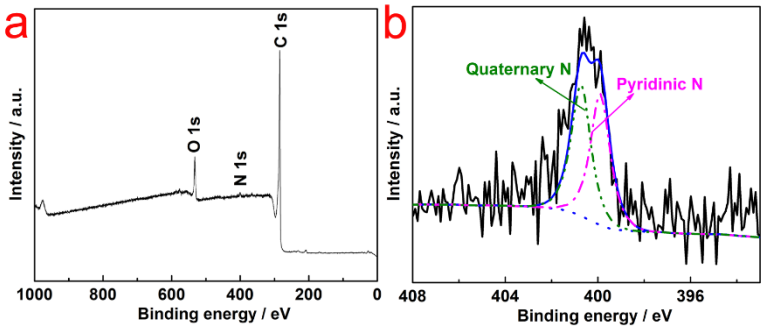

Fig. 15 XPS survey (a) and high resolution N 1s (b) XPS spectra of L-U.

The capacitive performance was further evaluated using the following equation [55] in the two-electrode system:

$$C = \frac{2I\Delta t}{m\Delta v} \tag{6}$$

where C is the specific capacitance, I is the charge/discharge current, Δt is the corresponding

charge or discharge time, *m* is the mass of active materials on single electrode, and Δv is the total corresponding potential change.

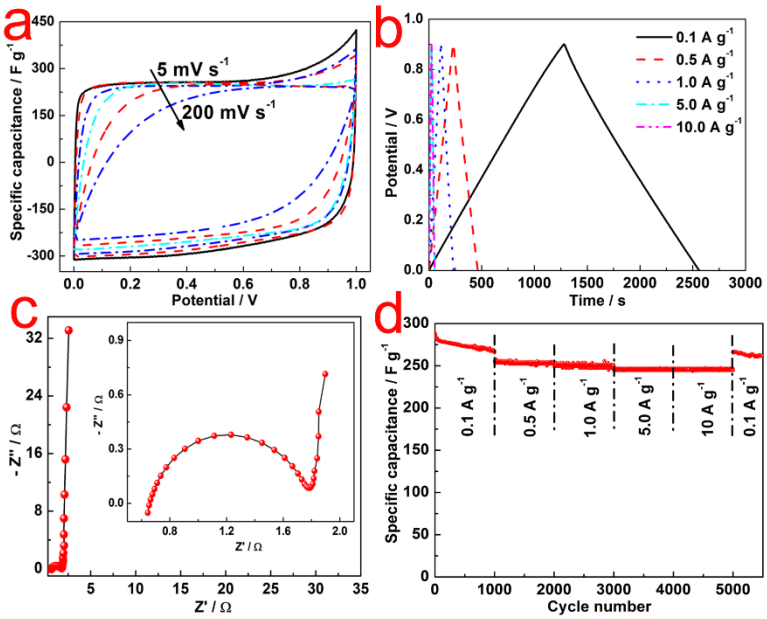

Fig. 16 CV curves (a) at different scanning rate ranging from 5 to 200 mV s^{-1}, galvanostatic charge/discharge (b) nyquist plots (c) and cycle life (d) at current density from 0.1 to 10 A g^{-1} of L-U electrodes in 6 mol L^{-1} KOH electrolyte.

Fig. 16a showed the CV curves at different scanning rate ranging from 5 to 200 mV s^{-1} of L-U electrodes in 6 mol L^{-1} KOH electrolyte. At different scanning rates, all the CV curves appeared rectangular shape, indicating the excellent capacitance behaviors of L-U. The calculated specific capacitances were 258, 255, 251, 249, 245, and 232 F g^{-1}, respectively, which kept 90% retainability with the increasing scanning rates, demonstrating the high specific capacitance of L-U electrodes, as well as potential stability.

The galvanostatic charge/discharge curves of activated electrodes at current densities from 0.1 to 10 A g^{-1} of L-U electrodes in 6 mol L^{-1} KOH electrolyte are shown in Fig. 16b. A symmetric triangle curve with no obvious Ohmic drop (IR_{drop}) was observed under all different current densities, implying less energy loss or heat produced during the charge/discharge process [67].

Impedance was considered another important factor of EDLCs electrodes. The EIS measurement was performed and shown by Nyquist plot scanned from 100 kHz to 10 mHz in Fig. 16c. The impedance curve consisted of an *x*-intercept at high frequency range (0.6 Ω), a semi-circle at medium frequency range (1.2 Ω) and vertically linear spike at low frequency range (0.8 Ω), which could be assigned to bulk electrolyte resistance, interfacial impedance between electrode and bulk solution, and the impedance that is associated with intra-particle pores, respectively [105-107]. The lower resistance implied the higher conductivity, which was necessary as EDLCs electrode materials.

To access the stability of assembled EDLCs, cycle life at current density from 0.1 to 10 A g^{-1} of L-U electrodes in 6 mol L^{-1} KOH electrolyte was performed (Fig. 16d). At each current density ranging from 0.1 to 10 A g^{-1}, the specific capacitance of 1000 charge/discharge cycles was recorded. The specific capacitances were 273, 253, 250, 245 and 245 F g^{-1} under current densities of 0.1, 0.5, 1.0, 5.0 and 10.0 A g^{-1}, respectively. An exception of a little degradation (93%) at initial 1000 cycles at 0.1 A g^{-1} appeared, almost 100% capacitance retention was obtained after each individual 1000 cycles at other current densities. Moreover, the specific capacitance restored to 267 F g^{-1} after 5000 cycles at current density of 0.1 A g^{-1}, which was close to the specific capacitance of 273 F g^{-1} obtained at initial 1000 cycles at the same current density. These results suggested

the prepared L-U electrode materials possessed superior stability in KOH aqueous electrolyte.

To evaluate the electrochemical performance of L-U electrodes in KOH-PVA solid electrolyte, CV test (Fig. 17a), galvanostatic charge/discharge (Fig. 17b) nyquist plots (Fig. 17c) and cycle life (Fig. 17d) were conducted at the identical testing conditions employed in aqueous electrolyte. In the CV measurements, the specific capacitances were 296, 282, 273, 268, 263, and 226 F g^{-1} at scanning rates of 5, 10, 20, 50, 100 and 200 mV s^{-1}, respectively, which was larger than that of L-U in 6 mol L^{-1} KOH in general but with slightly faster degradation.

Symmetric triangle curves with no IR_{drop} were shown as that of L-U in 6 mol L^{-1} KOH, indicating the good capacitive performance in KOH-PVA solid electrolyte.

In impedance analysis, a little larger resistance of bulk electrolyte resistance (1.2 Ω), interfacial impedance between electrode and bulk solution (1.2 Ω), and the impedance that is associated with intra-particle pores (1.2 Ω) were obtained, which might arise from the increase in the interface resistance between the electrodes and electrolytes since the solid electrolyte was difficult to diffuse into the inner layer of the electrodes [108].

In addition, specific capacitances of 306, 284, 276, 260 and 251 F g^{-1} were obtained under current densities of 0.1, 0.5, 1.0, 5.0 and 10.0 A g^{-1}, which were much higher than that of using 6 mol L^{-1} KOH electrolyte. In addition, excellent retention (almost 100%) at each individual 1000 cycles was displayed for each current density. After 5000 cycles, a comparable specific capacitance of 294 F g^{-1} was restored, revealing the excellent stability in KOH-PVA solid electrolyte.

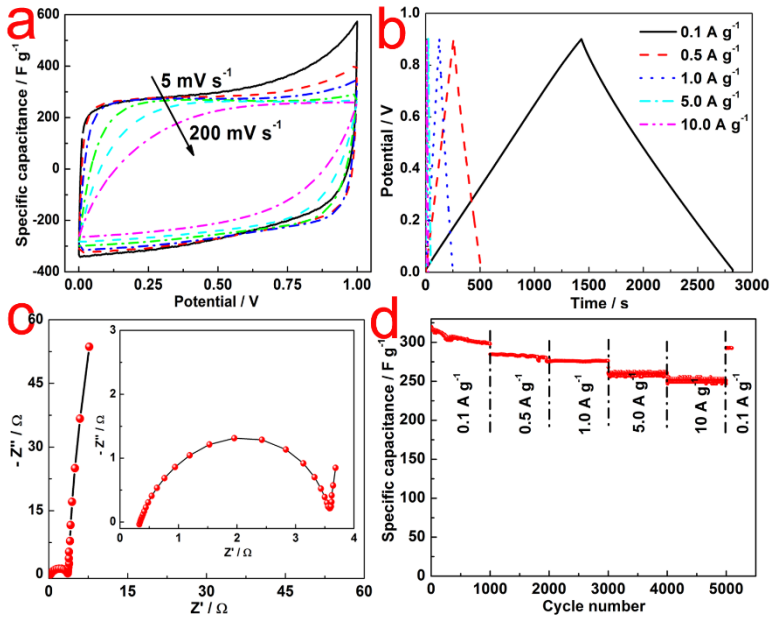

Fig. 17 CV curves (a) at different scanning rate ranging from 5 to 200 mV s^{-1}, galvanostatic charge/discharge (b) nyquist plots (c) and cycle life (d) at current density from 0.1 to 10 A g^{-1} of L-U electrodes in PVA-KOH solid electrolyte.

To demonstrate the operational characteristics, the energy and power densities in both the electrolyts were calculated according to the following equations [38]:

$$E = \frac{1}{2} C(\Delta V)^2 \tag{7}$$

$$P = \frac{E}{t} \tag{8}$$

where E is the average energy density (Wh kg^{-1}), C is the specific capacitance of the symmetric supercapacitor, ΔV is the voltage range, P is the average power density (W kg^{-1}) and t is the discharge time, respectively. As shown in Fig. 18, Ragone plots of L-U electrodes displayed slightly higher energy density of ~17 Wh kg^{-1} in PVA-KOH solid electrolyte than that of ~15 Wh kg^{-1} in 6 mol L^{-1} KOH electrolyte,. In addition,

comparable higher power density at different current density was exhibited for L-U electrodes in PVA-KOH solid electrolyte than in 6 mol L^{-1} KOH electrolyte.

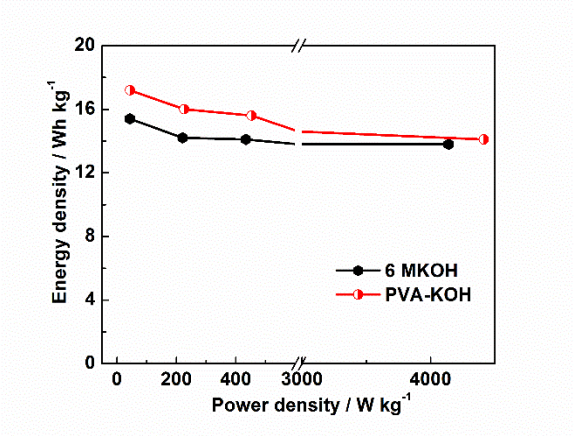

Fig. 18 Ragone plots of L-U electrodes in 6 L^{-1} KOH electrolyte and PVA-KOH solid electrolyte, respectively.

4.4 Conclusions

A supercapacitor electrode material with excellent performance has been prepared by the carbonization of urea-modified lignin under the activation of KOH. The resulting N-doped carbon materials exhibited porous structure with extraordinarily large SSA (3130 m^2 g^{-1}), which greatly enhanced the electrochemical performance. High specific capacitances of 273 and 306 F g^{-1} were obtained at a charge/discharge current density of 0.1 A g^{-1} for L-U electrode in 6 mol L^{-1} KOH aqueous and KOH-PVA solid electrolytes, respectively. With increasing in the current density and cycle number, good retention was kept for prepared porous N-doped materials in both electrolytes, demonstrating the excellent stability and reliable lifetime. Comparable energy and power density were obtained in both electrolytes. The excellent electrochemical performance of L-U indicated that it was a promising electrode material for EDLCs.

Chapter 5 Rod-shape porous carbon derived from aniline modified lignin for symmetric supercapacitors©

5.1 Introduction

Supercapacitors, also known as electrochemical capacitors have received considerable attention because of their high power density, fast charge/discharge capability and long cycle life [109-111]. Supercapacitors can be classified into two major categories based on the energy storage mechanism: electrical double layer capacitor (EDLC) and pseudocapacitor [112]. Energy stored in an EDLC is proportional to the electrostatic charge accumulated at the electrode/electrolyte interface. Therefore, the specific capacitance depends on the electrode surface area accessible to the electrolyte. On the other hand, pseudocapacitors store energy *via* the Faradaic reactions that occurr between the electrode materials and electrolyte. Pseudocapacitors usually use metal oxides/hydroxides (e.g. MnO_2, NiO, $Ni(OH)_2$, Co_3O_4) electrodes and possess higher specific capacitance than EDLCs that use carbon as electrode materials [113-117]. Pseudocapacitors are expected to find broader applications if their cycle stability can be improved, electrical conductivity can be increased, and the material cost can be reduced [118, 119].

Carbon-based materials are the primary electrode materials for EDLC. Porous carbon, such as activated carbon (AC), mesoporous carbon and graphene [41, 62, 120] have been commonly used in EDLC. EDLC electrode materials should possess the following characteristics: i) high specific surface area that provides sufficient accessible surface to the electrolyte; ii) proper pore size that allows the electrolyte ions to transfer smoothly

with short diffusion pathways; iii) excellent electrical conductivity to minimize resistive loss during charge/discharge; iv) sustainable and wide availability with low cost. The preparation of mesoporous carbon usually involves complex synthetic procedures in most cases, while graphene suffers from high cost although it could be obtained in labs after a series of harsh chemical treatments. Alternatively, activated carbon derived from abundant, renewable biomass feedstock can be produced sustainably at low cost [29]. So far, carbon materials derived from biomass such as rice husk, coffee grounds, grape seed, cornstalk, banana peel [34, 82, 121-123], have been explored as electrode materials in EDLC and promising electrochemical performance has been demonstrated.

Recent research showed that introducing nitrogen into activated carbon could induce additional pseudo-capacitance *via* reversible redox reactions and improve the wettability between the electrodes and electrolytes [124]. As a result, the capacitance performance of EDLC was greatly promoted. Therefore, biomass derived carbon materials with nitrogen may be promising electrode materials for EDLC. Since biochar typically contains low nitrogen content, we hypothesize that combination of nitrogen rich compounds with biomass will lead to biochar with high nitrogen content. Furthermore, there may be opportunities to tune the physicochemical properties of the nitrogen rich biochar, such as morphology, surface area, and conductance. Regarding the source of nitrogen, aniline appears a promising candidate because it is easy to polymerize, and the polymer can be grown into different shapes such as wires, tubes and spheres [63, 125, 126] by controlling the synthetic conditions.

Herein, we present aniline modified lignin as the raw materials to prepare rod-shape porous carbon as EDLC electrode materials. It is shown that the chemical activation plays

a key role in achieving large specific surface area, uniform pore size distribution and good conductivity, which lead to excellent electrochemical performance.

5.2 Experimental

5.2.1 Preparation of activated carbon

Solvent lignin (3 g), aniline (1.5 ml) and 30 ml ethanol were added into a flask with 30 ml ethanol, followed by stirring at 80 ℃ until the ethanol was evaporated. Then the mixture was heated at 400 ℃ for one hour with a heating rate of 10 ℃ min^{-1} for 1 h in a muffle furnace (1100 box furnace, Lindberg/Blue M, Thermo Scientific Inc.) under the protection of nitrogen (flow rate was 96 ml min^{-1}). After the precarbonized material was cooled to room temperature, it was mixed with potassium hydroxide (KOH, Fisher Scientific Inc.) in a mass ratio of 1:3, in a steel crucible also containing 30 mL deionized water. The crucible was placed in an oven and dried at 110 ℃ for 24 h. Then, the crucible was transferred into a muffle and activated at 600 ~900 ℃ for 1 h with a heating rate of 10 ℃ min^{-1} under N_2 protection (flow rate was 96 ml min^{-1}). Afterwards, the carbonized solids were washed with 30 mL 0.1 mol L^{-1} HCl (Fisher Scientific Inc.) at 110 ℃ for 1 h in a 60 mL polytetrafluoroethylene (PTFE) autoclave to remove the residual KOH and impurities. Finally, the carbon solid was washed several times with deionized water until the pH stabilized at 7. The material was then dried at 105 ℃ overnight in an oven. The carbonized samples were denoted as PL-600, PL-700, PL-800 and PL-900, corresponding to the activation temperature of 600 ℃, 700 ℃, 800 ℃, and 900 ℃, respectively. In addition, the carbon material derived from lignin (L) with the same method at 700 ℃ but without KOH was used as control sample.

5.2.2 Preparation of electrodes

Electrodes were prepared by mixing the activated carbon PL-600, PL-700, PL-800, PL-900 and L (80 *wt*%) with acetylene black (10 *wt*%) and PTFE (10 *wt*%), and then pressing onto a surface area of 1 cm^2 nickel foam (EQ-bcnf-16m, MTI Corp.). The electrodes were dried at 60 ℃ overnight in an oven. Afterwards, a sandwich structure was formed by placing two pieces of microporous PP separator celgard-3501 between two electrodes in a coin cell 2032 type system. Finally, the cell was pressed under a pressure of 1,000 kg cm^{-2} to finish the assembly.

5.2.3 Physical characterization

X-ray photoelectron spectroscopy (XPS) was performed on an SSX-100 system (Surface Science Laboratories, Inc.) equipped with a monochromated Al K_α X-ray source. For high resolution data, the lowest binding-energy C 1s peak was set at 285.0 eV and used as the reference for all of the other elements. Raman spectra were obtained on a Horiba LABRam confocal Raman microscopean with excitation wavelength of 532 nm from a diode pumped solidstate laser. Isothermal adsorption analyses with N_2 were carried out at 77 K (liquid nitrogen bath), using Tristar 3000 Micropore analyzer. The specific surface area was determined by the Brunauer-Emmett-Teller (BET) method and the pore size distribution was calculated according to the density functional theory (DFT) method [127] using NLDFT analysis for carbon with slit pore model (Micromeritics Inc.). Elemental analysis was conducted using Perkin Elmer 2400 II for C, H and N analysis and LECO Tru Spec Micro was used to analyze O with oxygen module. A transmission electron microscope (TEM) (JEM-2100 LaB6, JEOL) equipped with energy-dispersive X-ray spectroscopy (EDX) was used to study the morphology, microstructure, and elemental

mapping of the materials at an acceleration voltage of 80 kV. Additionally, a Technai Spirit G2 Twin (FEI Company) TEM operating at 120 kV was used to acquire some of the micrographs.

5.2.4 Electrochemical characterization

Cyclic voltammetry (CV) and electrochemical impedance spectroscopy tests were measured on an electrochemical work station (SP-150, BioLogical, France) in 6 mol L^{-1} KOH electrolyte. The galvanostatic charge/discharge curves were obtained from a battery test system (BTS series, NEWARE, China).

5.3 Results and discussion

TEM images of PL-700 with different magnifications are shown in Fig. 19. In contrast to the chunk shape for the L sample (Fig. 20a), this PL-700 material has rod-shape morphology (Fig. 19a and b) with large amount of pores. In high resolution images (Fig. 19c and d), the pores with different size can be observed clearly. The pores were closely distributed in the surface, but not connected with each other. The walls were so thin that it was damaged when irradiated by TEM beam (Fig 21a and b). Meanwhile, pores were also observed in samples PL-600 (Fig. 22a), PL-800 (Fig. 24a), and PL-900 (Fig. 25a). Different from PL-700, the pores in the other samples were obviously aggregated. This difference in the morphology of the activated carbon samples was primarily due to the activation temperature. Aniline monomer can be easily polymerized, and polyaniline can grow into different shapes, such as rods or spheres, even at room temperature. At high temperatures, the activation agent KOH reacted with carbon, producing gases (CO, H_2O and CO_2), forming pores and leaving behind potassium salts (K, KOH and K_2CO_3) [83]. The interconnected cavities in the porous carbon might serve as reservoirs for the

electrolyte, Thus, the pores with different size provided channels for ion transport and the thin walls led to short transport distance, resulting in small inner pore ions transferring resistance [128]. These characteristics were expected to promote the supercapacitor performance, as will be discussed later. In addition, elemental mapping was performed and shown a homogeneous distribution of elements (C, N and O) in all activated samples (Fig. 22, 23, 24 and 25).

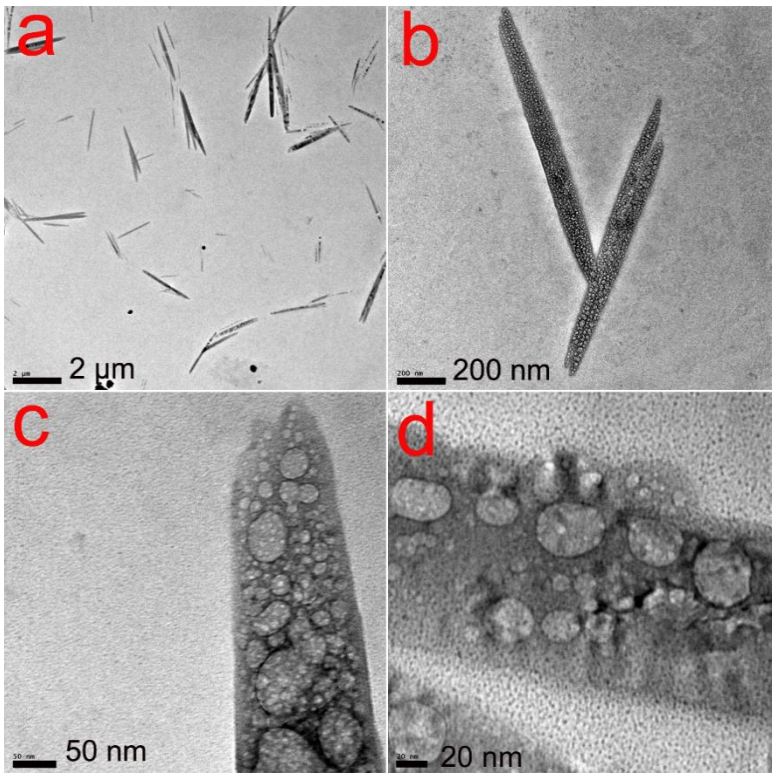

Fig. 19 Different magnifications TEM images of PL-700.

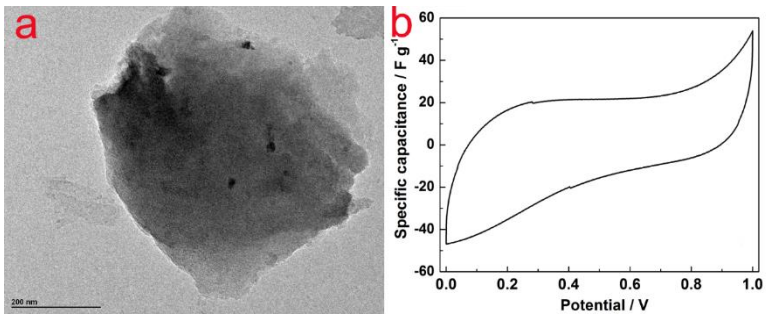

Fig. 20 TEM image of L (a) and CV curves (b) at scanning rate 20 mV s^{-1} of L electrodes in 6 mol L^{-1} KOH electrolyte.

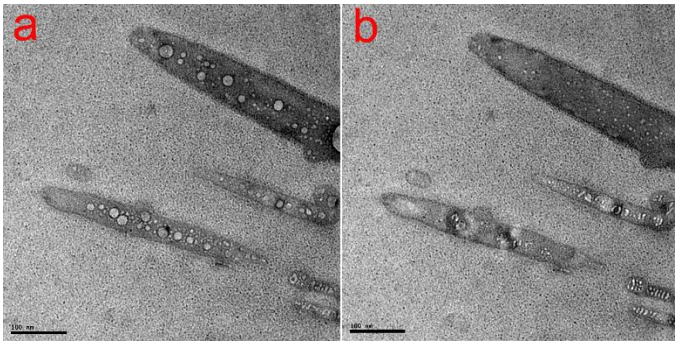

Fig. 21 Pore walls before (a) and after (b) damaged.

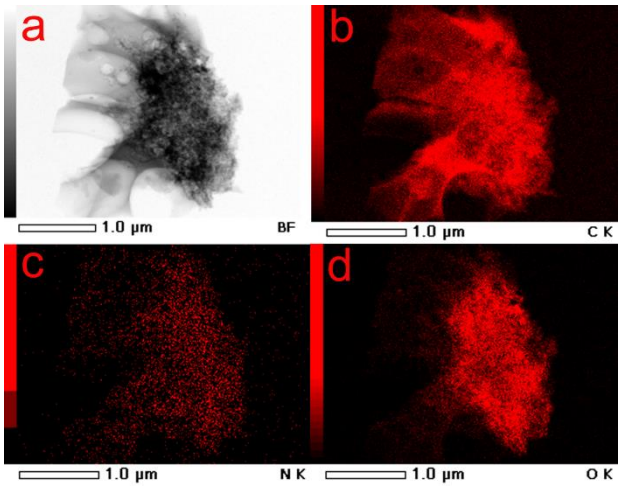

Fig. 22 Elemental mapping of PL-600.

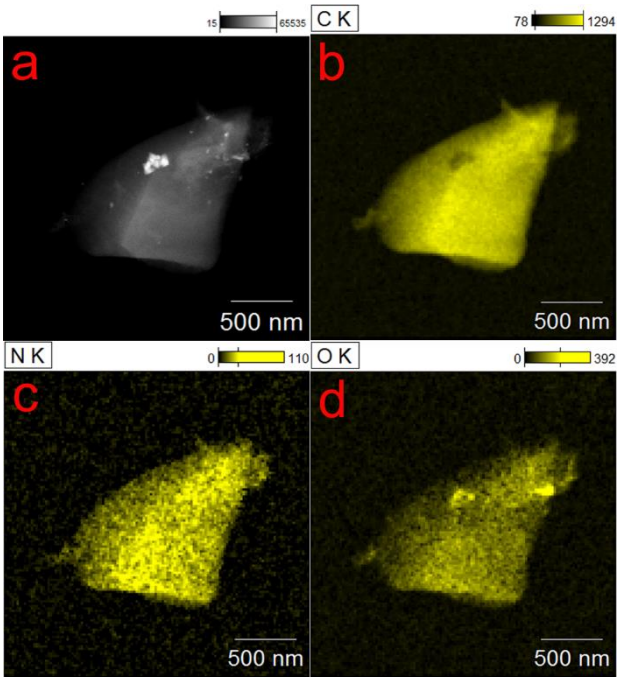

Fig. 23 Elemental mapping of PL-700.

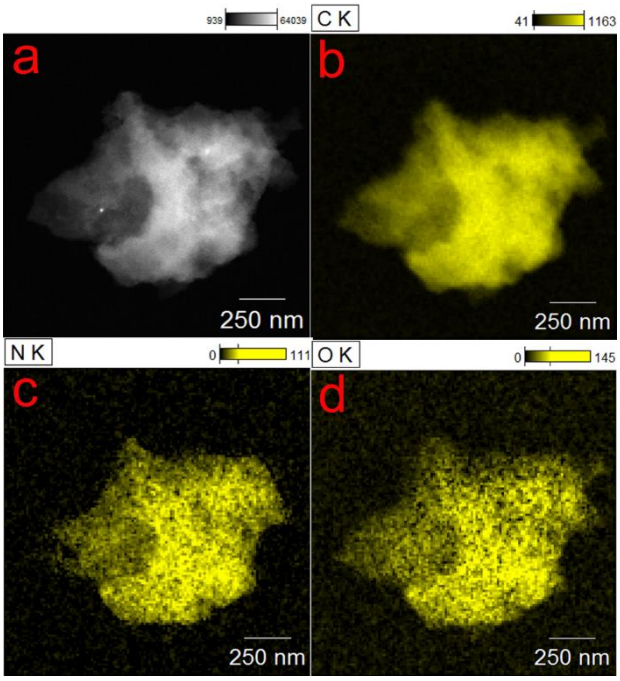

Fig. 24 Elemental mapping of PL-800.

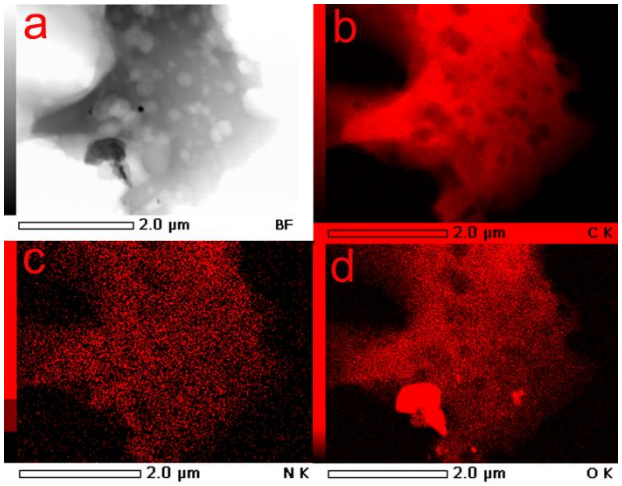

Fig. 25 Elemental mapping of PL-900.

N_2 sorption/desorption was conducted to characterize the surface area and pores size distribution (Fig. 26a and b). The BET specific surface area were 1886, 2265, 2467, and 2014 m^2 g^{-1} for samples PL-600, PL-700, PL-800 and PL-900, respectively, and showed dependence on the activation temperature. Interestingly, the pore size distribution (Fig. 2 6b) for all the samples showed similar pore width centered at 27 nm. The similar pore structure was probably resulted from using the equal amount of KOH and biomass for all samples activation. The samples possessed higher BET specific surface area with proper pore sizes are expected to be a promising EDLC electrode material. Raman spectra of the samples are shown in Fig. 26c. Two apparent peaks in the spectra were found, corresponding to the *D* band at 1346 cm^{-1} and *G* band at 1585 cm^{-1}. The *G* band revealed the formation of graphitic carbon. The *D* band reflected the degree of disorder which was associated with defects in hexagonal graphitic layers. The relative intensity ratio of *D* and G bands (I_D/I_G) was also used to evaluate degree of crystallinity, the smaller value means the higher degree of graphitization and less disordered nature of carbon [129, 130]. The I_D/I_G values were estimated to be 1.33, 1.10, 1.07 and 1.04 for the samples activated at 600 ℃, 700 ℃, 800 ℃ and 900 ℃, respectively. The values decreased as the temperature

increased, indicating the degree of graphitization was enhanced and electrical conductivity would be promoted.

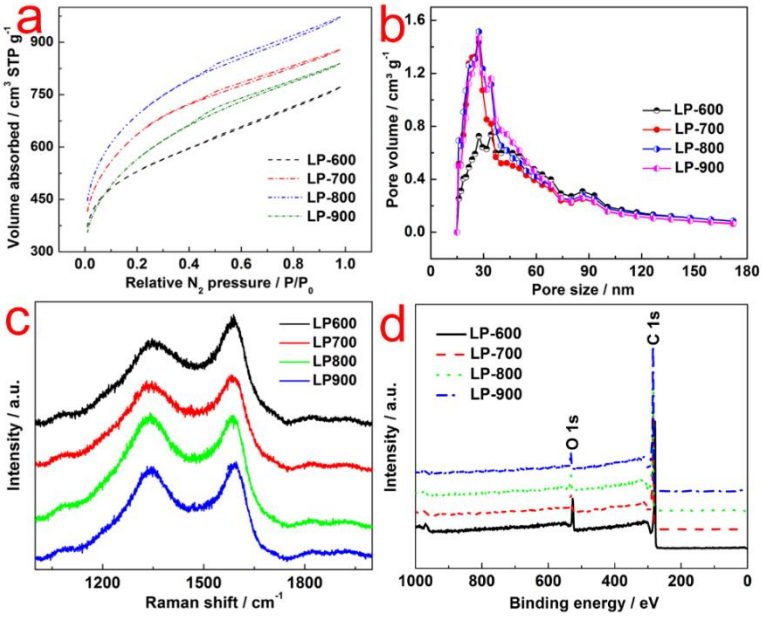

Fig. 26 N_2 sorption-desorption isotherms (a) and pore size distribution (b), Raman spectra (c) and XPS survey spectra (d) of PL-600, PL-700, PL-800, and PL-900.

To clarify the surface chemical compositions of the obtained samples, XPS measurement was employed. As expected, C (285 eV), O (532 eV) signals were detected, however, no N signal was detected in the XPS survey spectra for all four samples (Fig. 26d). This result appeared inconsistent with the results of element mapping in TEM and given the N-containing raw material we used. Elemental analysis was subsequently carried out to analyze the compositions of the samples. As presented in Table 2, N was indeed detected along with C and O in all four samples. The content of N was found to be 0.64 *wt*%, 0.29 *wt*%, 0.26 *wt*% and 0.33 *wt*% for PL-600, PL-700, PL-800, and PL-900, respectively. Considering the XPS result, it was likely that N was accumulated below the surface because this surface analysis technique had a detection depth only *ca*. 10 nm. Introducing

nitrogen into activated carbon has proven to be effective in improving the materials conductivity and subsequently promoting the capacitance performance [131]. Therefore, it is important to confirm the existence of nitrogen. The presence of N was expected to induce additional pseudo-capacitance *via* reversible redox reactions and improve the wettability between the electrodes and electrolytes [124].

Table 2 Elemental analysis of PL-600, PL-700, PL-800 and PL-900.

Sample	Carbon (*wt*%)	Hydrogen (*wt*%)	Nitrogen (*wt*%)	Oxygen (*wt*%)
PL-600	74.52	2.91	0.64	21.93
PL-700	87.28	1.19	0.29	11.24
PL-800	91.88	1.21	0.26	6.65
PL-900	91.70	0.60	0.33	7.37

To evaluate the specific capacitance in the two-electrode system, the following equation [104] was used:

$$C = \frac{I\Delta t}{\Delta V M} \times 2 \qquad (9)$$

where C (F g^{-1}) is the specific capacitance, I (A) is the discharge current, Δt (s) is the discharge time, Δv (V) is the voltage change (excluding the iR drop) within the discharge time, and M (g) is the total mass of the active materials on the two electrodes, factor 4 is to adjust the capacitance of the cell and the combined mass of two electrodes to the capacitance and mass of a single electrode [132].

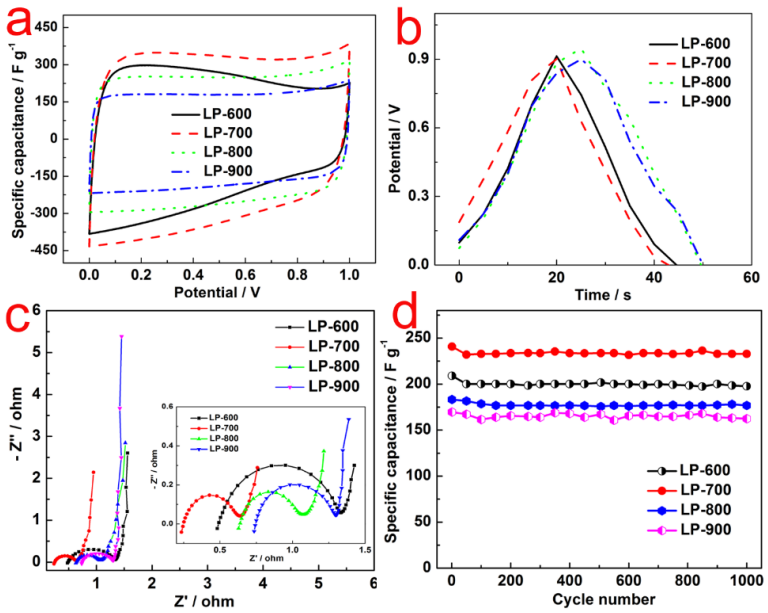

Fig. 27 CV curves (a) at scanning rate 20 mV s^{-1}, galvanostatic charge/discharge (b) nyquist plots (c) and cycle life (d) at current density 1.0 A g^{-1} of PL-600, PL-700, PL-800 and PL-900 electrodes in 6 mol L^{-1} KOH electrolyte.

Fig. 27a showed the CV curves of PL-600, PL-700, PL-800, and PL-900 at a scanning rate of 20 mV s^{-1}. The CV curves tended to be regular rectangle with the increase in the activation temperature, indicating materials have promising potential as EDLC electrodes. The sample PL-700 exhibited the largest specific capacitance of 333 F g^{-1}, which was significantly larger than that of 21, 269, 247, 179 F g^{-1} for L, PL-600, PL-800 and PL-900, respectively. In addition, PL-700 behaved better than PL-600, PL-800 and PL-900 at different scanning rates (5, 10, 20, 50, 100 and 200 mV s^{-1}), as shown in Fig. 28. Although PL-700 exhibited the highest specific capacitance among these four samples, it was not the sample with the largest specific surface area or N content. This seems not in consistent with the expected contribution from N and porous structure. The most possible reason was that the PL-700 sample had larger effective specific surface area that provided

better accessibility to the electrolyte and facilitated efficient ion transport with lower resistance [133]. In addition, it is well known that introducing N enhances the electrical conductivity of carbon and produces pseudocapacitance effect to improve the specific capacitance. Furthermore, among the four types of N-groups (pyridinic N, pyrrolic N, quaternary N, and pyridinic N-oxide) formed after carbonization [134], only pyridinic N and pyrrolic N contributed to enhancing specific capacitance [43]. Although N was not detected by XPS in our samples due to the special structure of the samples mentioned above, it was still quite likely that PL-700 possessed more pyridinic N and pyrrolic N than the other samples.

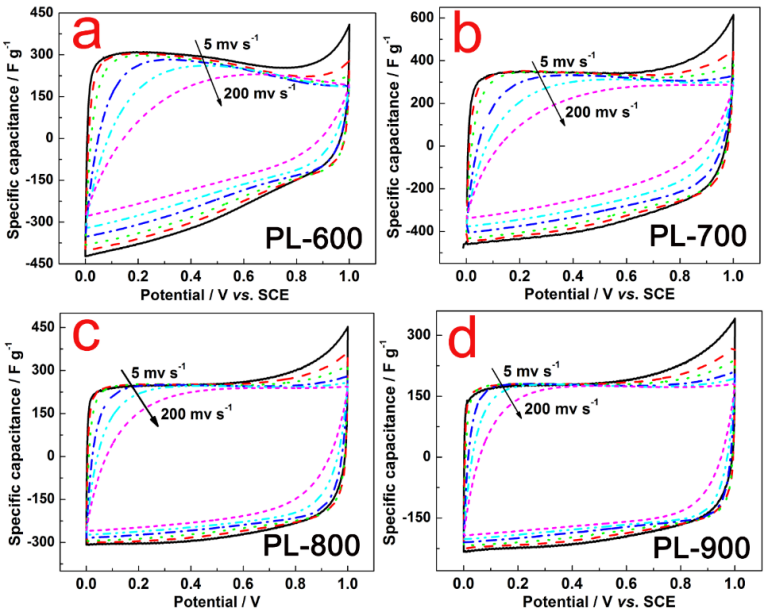

Fig. 28 CV curves of PL-600, PL-700, PL-800 and PL-900 at different scanning rate (5, 10, 20, 50, 100 and 200 mV s^{-1}).

The galvanostatic charge/discharge curves of activated electrodes at current density of 1.0 A g^{-1} was shown in Fig. 27b. As other samples, PL-700 also displayed a symmetric

triangle curve and no obvious Ohmic drop (IR_{drop}) was observed, which was an indicative of good capacitive performance [67].

Impedance was considered as an important index to access the electrode materials for EDLC. The EIS measurement was performed in the range from 0.1 to 100 kHz in the two-electrode cell to characterize the resistance (as shown in Fig. 27c). At the low frequency region, a straight line could be observed, which represented the contact resistance. The steeper line indicates better behavior of the electrodes [43]. In the high frequency region, all the samples exhibited an obvious semicircle for which the smaller radius means the lower ESR (inset in Fig. 27c). This behavior indicates equivalent series resistance (ESR) referring to electrode conductivity and the charge-transfer resistance in the electrode materials. The PL-700 exhibited the steepest straight line and smallest radius at low and high frequencies, demonstrating the excellent electrochemical characteristics.

The cyclic stability of the electrodes was measured by charge/discharge at a constant current density of 1.0 A g^{-1}, as shown in Fig. 27d. After 1, 000 charge/discharge cycles, all the samples showed almost 100% retention of capacitance. Still, PL-700 maintained the largest specific capacitance and steady cycle life compared to other samples. Therefore, it was a very promising EDLC electrode material.

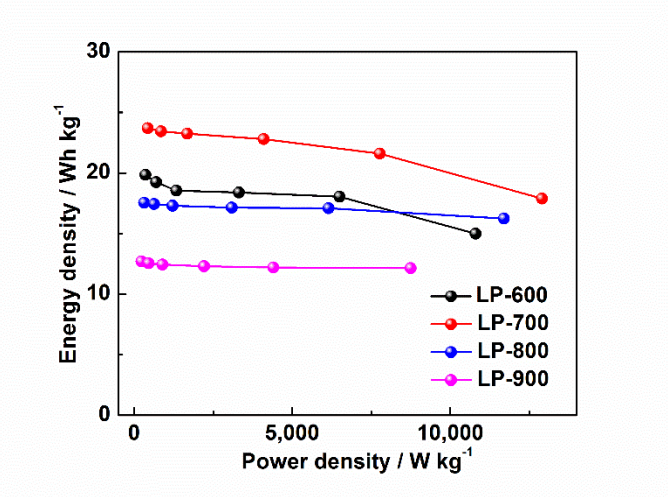

Fig. 29 Ragone plots related to energy and power densities of PL-600, PL-700, PL-800 and PL-900 electrodes.

To demonstrate the operational characteristics, the energy and power density were calculated according to the following equations [135]:

$$E = \frac{1}{2} C(\Delta V)^2 \tag{10}$$

$$P = \frac{E}{t} \tag{11}$$

where E is the average energy density (Wh kg^{-1}), C is the specific capacitance of the symmetric supercapacitor, ΔV is the voltage range, P is the average power density (W kg^{-1}) and t is the discharge time, respectively. Fig. 29 depicted the Ragone plots for PL-600, PL-700, PL-800 and PL-900 at different scan rates. The energy density of PL-700 was considerably larger than that of the others at all scan rates. Besides, there was no large decrease in the energy density at higher power density. Thus, the PL-700 electrode presented excellent operational characteristics due to the steady energy density output at various power density.

5.4 Conclusion

The rod-shape porous carbon derived from aniline modified lignin has been successfully prepared *via* KOH activation. The activation temperature determines the microstructure and morphology of the resulting carbon. The materials activated at 700 ℃ exhibited high specific surface area with inconnected cavities, which lead to the highest specific capacitance of 336 F g^{-1}, smallest resistance of 0.9 Ω and excellent stability in electrochemical performance as compared to the materials activated at different temperatures (600, 800, and 900 ℃). The PL-700 also exhibited remarkable operational characteristics in terms of power and energy density. The superior performance of PL-700 indicates that it is a promising electrode material for EDLC.

Chapter 6 Nitrogen-modified biomass-derived cheese-like porous carbon for electric double layer capacitors©

6.1 Introduction

The increasing demand in energy has become the biggest challenge of the world due to limited conventional fossil fuels (coal, petrol and natural gas, etc.) and environmental concerns. It is pressing to develop sustainable energy technologies to fill the growing needs. Energy storage is a critical component in sustainable energy infrastructure. Hence, recent research has been focused on developing environmentally friendly energy storage devices, such as Li-ion batteries and supercapacitors [136-138]. Among energy storage devices, supercapacitors, also called electrochemical capacitors or ultracapacitors, are considered the promising candidate due to their fast charge/discharge rate, high power and energy density, and long lifetime [139-141]. Based on the charge storage mechanism, supercapacitors can be classified into two types: electric double layer capacitors (EDLCs) and pseudocapacitors [8]. EDLCs achieve energy storage and release *via* ion adsorption and desorption to the electrical double layers when a voltage is applied or removed [8]. In contrast, the fast and reversible electrochemical reactions occurring on the electrodes are the key processes to achieve energy storage in pseudocapacitors [8].

Completely different electrode materials are required in these two types of supercapacitors due to their distinct working principles. In EDLCs, activated carbon with large specific surface area (SSA) (> 2000 m^2 g^{-1}) and porosity is desired electrode material [142]. In pseudocapacitors, transition metal oxides (NiO, CoO and Mn_xO_y) [143-146] are widely used due to their essential redox reactions in electrolyte. In comparison

with EDLCs, pseudocapacitors offer larger specific capacitance, but suffer from degradation of capacitance and low cycle stability [77]. On the other hand, EDLCs possess the merits of abundant resources, low cost and high stability [77, 147, 148]. Therefore, searching for suitable carbon electrodes is the key to developing superior EDLCs.

In general, activated carbon with large SSA and porosity is necessary for achieving high capacitance EDLCs, as it provides enough space and channels for ion adsorption and desorption during charge and discharge [19]. A variety of methods, such as chemical activation, template modification, physical activation and combined activation, have been developed to prepare highly efficient electrode carbon. Among these methods, heat treatment under the assistance of chemicals (KOH, $ZnCl_2$, and H_3PO_4) [82, 83, 149] is an efficient way to produce porous carbon. The added chemicals react with biochar during the heat treatment process and generate gases (e.g. CO_2, CO, and H_2) [83]. This etching and subsequent gas emission (called chemical activation and physical activation) make synergetic contribution to large SSA and porosity [83].

Recent research revealed that, in addition to large SSA and porosity, introducing heteroatoms, especially nitrogen (N) atoms, into carbon framework could significantly enhance the performance of EDLCs [66]. This idea was originally developed for improving the conductivity of carbon material used for oxygen reduction reaction (ORR) electrocatalyst in fuel cells [150]. Porous carbon with improved conductivity through N doping also benefited EDLCs. Furthermore, it was noted that the N-doped structure could provide pesudocapacitance originated from the faradaic interactions between the ions of the electrolytes and the carbon electrode surface [124, 151, 152]. As a result, doping

porous carbon with nitrogen is considered an effective strategy to enhancing EDLCs electrode performance.

In this respect, synthesizing N-doped carbon with large SSA and porosity is expected a promising approaching to preparing high performance EDLCs electrode. Inspired by this idea, we report herein an effective nitrogen-doping method to dramatically enhance the EDLCs performance. Lignin, which is an abundant biomass in nature, was modified by N-rich pyrrole and then activated *via* combined chemical activation and physical activation. The chemical activation was responsible for large SSA, while physical activation created porous structures, leading to cheese-like morphology. Owing to the contribution of large SSA, porosity and N doping, the prepared activated carbon showed high specific capacitance, superior rate performance, and excellent cycle stability. Hence, the N-doped porous carbon developed in this work is a promising candidate for EDLCs electrode.

6.2 Experimental

6.2.1 Preparation of electrode materials

3 g solvent lignin was added into flask with 30 ml ethanol (C_2H_5OH) and ultrasonicated for 30 min to dissolve the lignin. Then, 1.5 ml pyrrole (C_4H_5N, Fisher Scientific Inc.) was added, followed by stirring at 80 ℃ until the ethanol was evaporated. The mixture was pre-carbonized by baking at 400 ℃ for one hour with a heating rate of 10 ℃ min^{-1} in a muffle furnace (1100 box furnace, Lindberg/Blue M, Thermo Scientific Inc.) under the protection of nitrogen (flow rate was 96 ml min^{-1}). After the pre-carbonized material was cooled down to room temperature, it was mixed with potassium hydroxide (KOH, Fisher Scientific Inc.) in a mass ratio of 1:3, in a steel crucible containing 30 mL deionized

water. The crucible was placed in an oven and dried at 110 ℃ for 24 h. Then, the crucible was transferred into a muffle and activated at 700 ℃ for 1 h with a heating rate of 10 ℃ min^{-1} under N_2 protection (flow rate was 96 ml min^{-1}). Afterwards, the carbonized solid was washed with 30 mL 0.1 mol L^{-1} HCl (Fisher Scientific Inc.) at 110 ℃ for 1 h in a polytetrafluoroethylene (PTFE) autoclave to remove the residual KOH and impurities. Finally, the carbon solid was washed several times with deionized water until the pH stabilized at 7. The material was then dried at 105 ℃ overnight in an oven. The carbonized samples were denoted as KPL.

For comparison, samples prepared with the same procedure but without KOH were denoted as PL, and raw lignin directly carbonized with the same procedure of PL was denoted as L.

6.2.2 Assembly of supercapacitors

Electrodes were prepared by mixing the prepared carbon KPL, PL and L (80 *wt*%) with acetylene black (10 *wt*%) and PTFE (10 *wt*%), and then pressing onto a surface area of 1 cm^2 nickel foam (EQ-bcnf-16m, MTI Corp.). The electrodes were dried at 60 ℃ for 12 h in an oven. Afterwards, a sandwich structure was formed by placing two pieces of microporous Polypropylene (PP) separators (celgard-3501) between two electrodes in a 2032 type coin cell system. The separators were pre-soaked in 6 M KOH solution for 30 min before using. Finally, the cell was pressed under a pressure of 1,000 kg cm^{-2} to finish the assembly.

6.2.3 Physical characterization

The surface analysis was performed on a Kratos Axis Ultra high performance x-ray photoelectron spectroscopy (XPS) (Kratos Analytical Ltd.). For high resolution data, the lowest binding-energy C 1s peak was set at 285.0 eV and used as the reference for other elements. Raman spectra were obtained on a Horiba LABRam confocal Raman microscopean with excitation wavelength of 532 nm from a diode pumped solid state laser. Isothermal adsorption analysis with dry N_2 was carried out at 77 K (liquid nitrogen bath), using ASAP2020 (Micromeritics Inc.) micropore analyzer. The specific surface area was determined by the Brunauer-Emmett-Teller (BET) method and the pore size distribution was calculated according to the density functional theory (DFT) method using non-local density functional theory (NLDFT) analysis for carbon with slit pore model. A transmission electron microscope (TEM) (JEM-2100 LaB6, JEOL) equipped with energy-dispersive X-ray spectroscopy (EDX) was used to study the morphology and microstructure at an acceleration voltage of 80 kV.

6.2.4 Electrochemical characterization

Cyclic voltammetry (CV) and electrochemical impedance spectroscopy tests were measured on an electrochemical work station (SP-150, BioLogical, France) in 6 mol L^{-1} KOH electrolyte. The galvanostatic charge/discharge curves were obtained from a battery test system (BTS series, NEWARE, China).

6.3 Results and discussion

The morphology of prepared samples L, PL and KPL are shown in Fig. 30. Both L and PL exhibited similar chunk structure, and no obvious pores were observed. Conversely, the KPL had a cheese shape with plenty of pores of various sizes, implying possible high

SSA and porosity. Examining the synthetic process led to the conclusion that the significant difference in morphology was caused by the synergetic effects of chemical and physical activation. In detail, the activation agent KOH reacted with carbon at high temperatures and new carbon framework and pore network were formed via etching. At the same time, gases were produced, which promoted porosity by gasification effect. Moreover, intercalating metallic K into the carbon matrix resulted in the expansion of carbon lattice [83, 153]. Once the intercalated K and K compounds were removed by washing, more micropores formed as the expanded carbon matrix could not return to the original non-porous structure [83]. To confirm the porous structure of the KPL sample, SEM was employed (Fig. 30d). Similar to the TEM image, pores were observed on the surface of the KPL samples. Considering ion adsorption and desorption and ion transport during the process of charge and discharge, the porous structure not only provided large surface area (micro and mesopores) , but also served as reservoirs (macropores) for the electrolyte [23, 154]. In addition, the mesoporoes provided ion transportation channels to shorten transport distance with low transport resistance [78]. All these features were expected to promote the EDLCs performance.

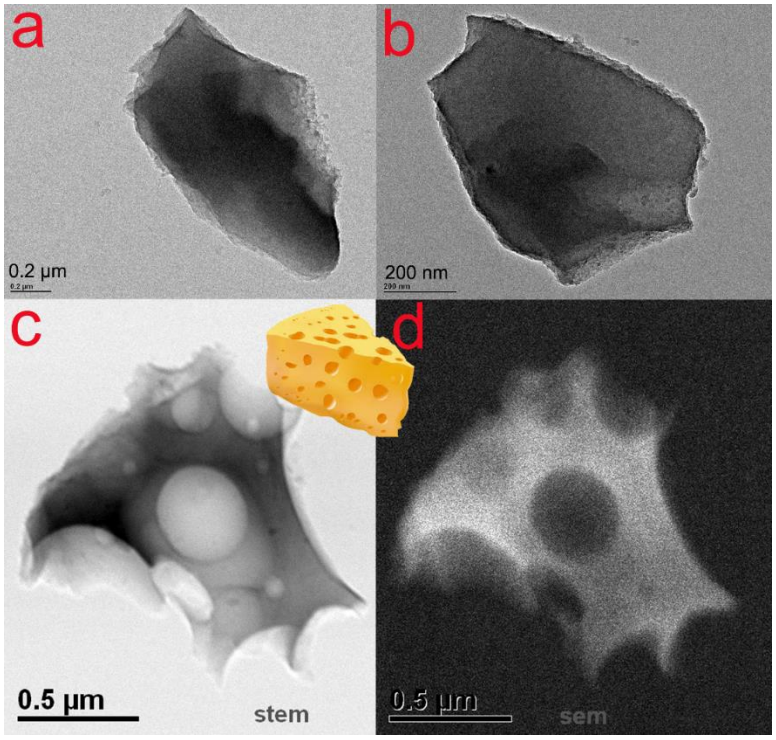

Fig. 30 TEM images of L (a), PL (b) and KPL (c); SEM image of KPL (d).

Based on the TEM and SEM results, the surface area and pores size distribution were further studied by N_2 sorption/desorption (Fig. 31a). The as-prepared KPL exhibited type I isotherm according to IUPAC classification for mesoporous materials and showed high BET SSA (2661 m^2 g^{-1}). The mesoporous morphology was further supported by pore size distribution based on NLDFT analysis. As shown in the insert in Fig. 31a, the pore size centered at ~15 nm. From the pore size contribution, it was expected that the ordered mesopore channels (2-50 nm) facilitated the diffusion of the electrolyte ions, and a noticeable volume of micropores (<2 nm) could provide abundant adsorption sites for the ions [155]. The graphitic structure of the prepared samples was confirmed by Raman spectra (Fig. 31b). Two distinct peaks located at ~1350 and 1580 cm^{-1} were displayed for all three samples, which were attributed to D-band and G-band, respectively. The *D*-band was related to the presence of disordered carbon structures, while the *G*-band was

associated with the vibration of sp^2-hybridized carbon atoms in a graphitic layer [129]. The intensity ratio of D and G band (I_D/I_G) is well known to be an indicator of graphitization degree, a small I_D/I_G value means high degree of graphitization [129, 130]. The I_D/I_G values of L, PL and KPL were determined to be 0.98, 0.96 and 1.0, respectively, suggesting the equivalent degree of graphitization due to the same temperature and time used for heat treatment.

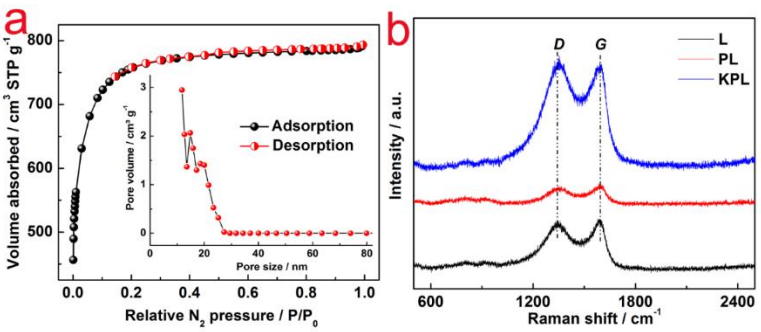

Fig. 31 (a) N_2 sorption-desorption isotherms of L. The insert in (a) shows pore size distribution; (b) Raman spectra of L, PL and KPL.

In order to confirm the surface atom bonding state, XPS measurement was conducted for L, PL and KPL (Fig. 32, Fig. 33 and Fig. 34). In XPS survey spectra (shown in Fig. 32a), both C and O signals were detected in all three samples, but N signals were only detected in sample PL and KPL. This result confirmed that N was not incorporated in the raw materials. High resolution C 1s spectra of KPL showed signals of C-C, C-O/C-OH, C=O/C-N, COOH, and CO_2/CO_3^{2-} bond and functional groups at binding energy of 285.1, 286.3, 287.7, 289.2, and 291.1 eV, respectively [58, 156]. These signals were also detected in the other two samples. In addition, a very weak signal of C-F bond at 293.5 eV was detected for samples L and PL, which possibly originated from impurities. Moreover, three types of O species (O-I, O-II and O-III) were observed for L, PL, and

KPL (Fig. 33b, Fig. 34c and Fig. 32d). Peaks at around 531, 532 and 535 eV were attributed to C=O groups (carbonyl/quinone), carbonyl oxygen atoms (phenol/ether) and oxygen atoms (carboxylic groups COOH and/or chemisorbed O_2/H_2O), respectively [157]. This result matched well with the C 1s analysis. These functional groups were expected to enhance the wettability of the activated carbon electrodes and offer more accessible surface area for ion adsorption and desorption in aqueous KOH electrolyte. Therefore, the specific capacitance of EDLCs would increase due to efficient surface utilization.

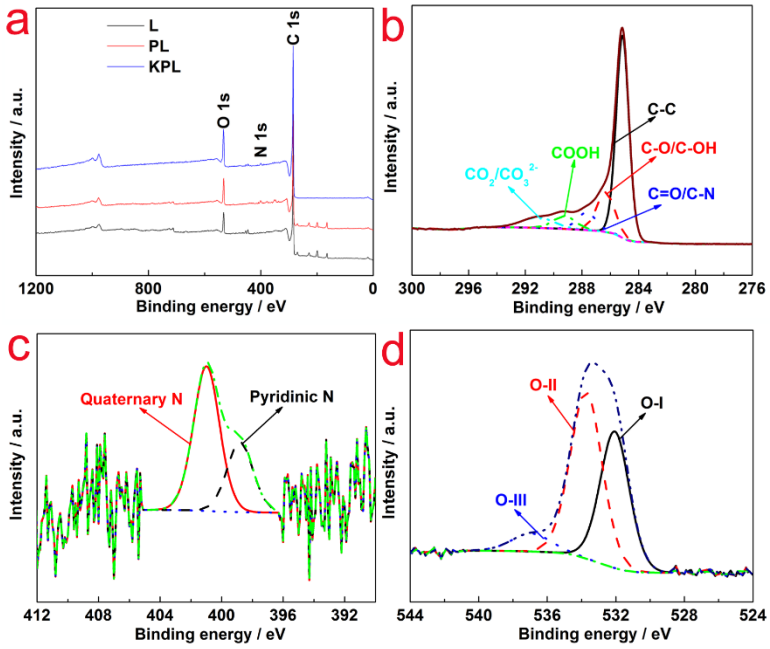

Fig. 32 XPS survey spectra of L, PL and KPL (a); C 1s (b), N 1s (c) and O 1s (d) XPS spectra of KPL.

The N species were further characterized by high resolution N 1s spectra for PL and KPL. The spectra were deconvoluted into two peaks at 398.8 and 401 eV, corresponding to pyridinic-N, and quaternary-N, respectively (Fig. 32a and Fig. 34b) [158, 159].

Accordingly, the atomic content of pyridinic-N in KPL was found to be 32.61%, which was higher than that of 28.10% for PL. N played a critical role in improving EDLC performance. In addition to enhance the conductivity of the carbon material, pyridinic-N has been proven been able to nduce pesudocapacitance behavior between the ions of electrolytes and the carbon electrode surface [160, 161]. Specifically, pyridinic-N could be oxidized into pyridine nitrogen/oxidized pyridine nitrogen. On contrast, pyridine nitrogen/oxidized pyridine nitrogen could be reduced into pyridinic-N [160, 161]. These reaction are similar in the pesudocapacitors.

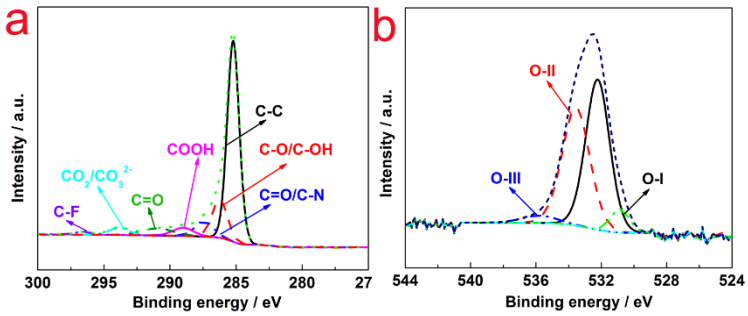

Fig. 33 C 1s (a), and O 1s (b) XPS spectra of L.

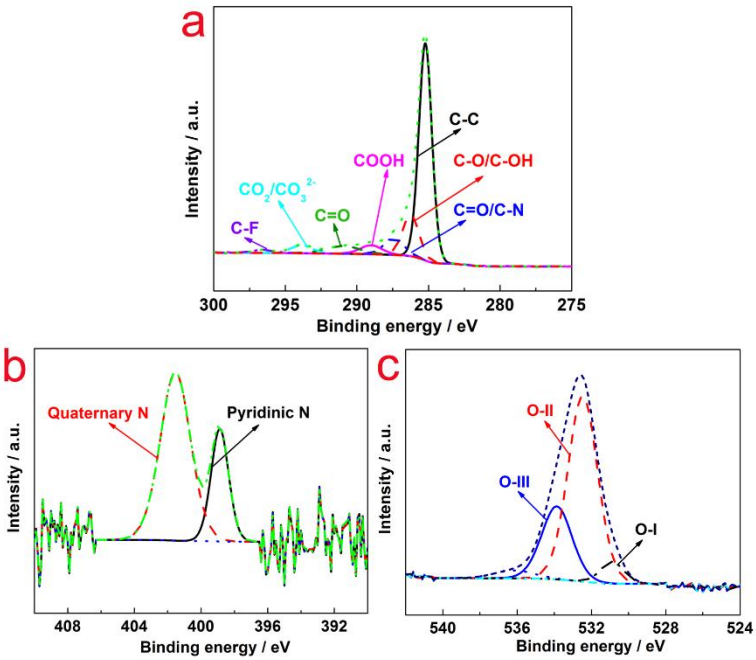

Fig. 34 C 1s (a), N 1s (b) and O 1s (c) XPS spectra of PL.

Fig. 35a, c and e depicts the CV curves of the L, PL and KPL EDLC cells at various scanning rates of 5, 10, 20, 50, 100, 200, and 300 mV s^{-1} between 0 and 1.0 V. The CV curves of KPL appeared rectangular, which clearly distinguished from that of distorted rectangular shape for L and PL, and indicated excellent characteristics of double-layer capacitance. In addition, KPL exhibited the largest area of loop, revealing the highest capacitance. Furthermore, KPL still remained a typical rectangular CV curve at a scan rate as high as 300 mV s^{-1}, which implied efficient charge transfer and electrolyte diffusion within porous carbon materials [162]. To more accurately evaluate the specific capacitance in the two-electrode system, the following equation [55] was used:

$$C = \frac{2I\Delta t}{m\Delta v} \qquad (12)$$

where C is the specific capacitance, I is the charge/discharge current, Δt is the corresponding charge or discharge time, m is the mass of active materials on single electrode, and Δv is the total corresponding potential change. The calculated largest specific capacitance for L and PL were 50 and 60 F g^{-1} even if the CV curves were assumed to be ideal rectangular. However, the specific capacitance of KPL reached 278, 276, 270, 269, 267, 265 and 258 F g^{-1} at scanning rate of 5, 10, 20, 50, 100, 200 and 300 mV s^{-1}, respectively. Such a high specific capacitance was attributed to the large specific surface area, cheese-like porous structure, and high degree of graphitization as analyzed above.

Fig. 35b, d and f present the galvanostatic charge/discharge plots at different current densities of 0.1, 0.5, 1.0, 5.0 and 10.0 A g^{-1} for L, PL and KPL electrodes, respectively.

Both sample L and PL showed a comparable symmetric triangle curve with obvious Ohmic drop (IR_{drop}) at either low or high current density. Conversely, KPL displayed a symmetric triangle curve and no obvious IR_{drop} was observed, which was an indication of good capacitive performance. The small IR_{drop} implied that the internal resistance of the KPL was much smaller than that of L and PL, and less energy would be wasted to produce unwanted heat during charging and discharging [67]. Thus, the KPL possessed much better capacitance behavior than L and PL.

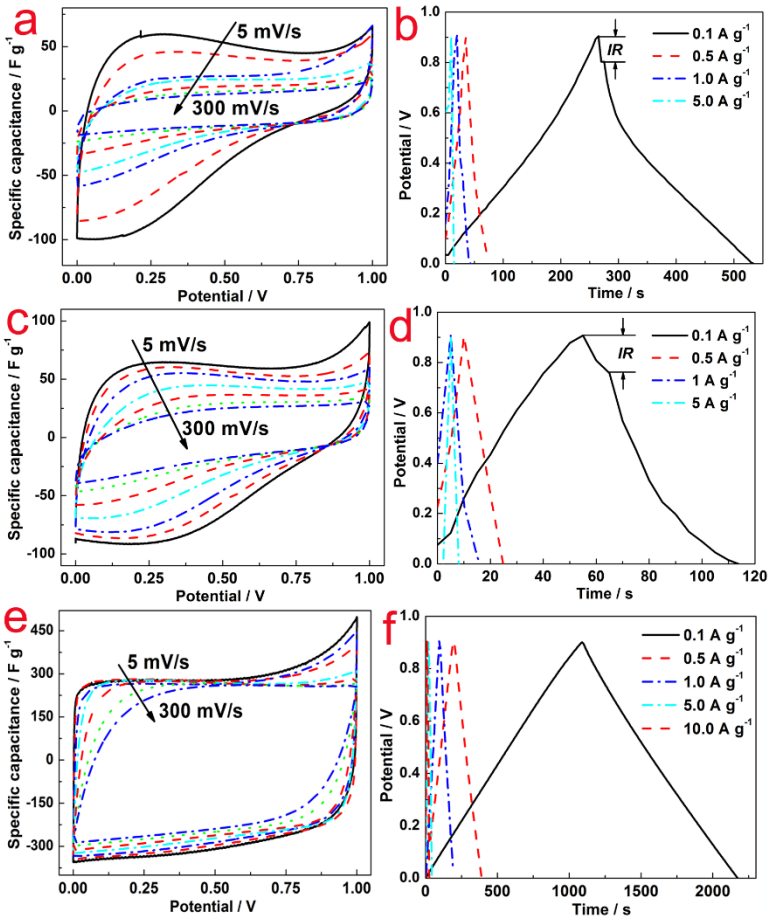

Fig. 35 CV curves of L (a), PL (c) and KPL (e) electrodes at various scanning rates ranging from 10 to 300 mV s^{-1}; and galvanostatic charge/discharge curves of L (a), PL (c) and KPL (e) electrodes at different current densities ranging from 0.1 to 10 A g^{-1}.

Furthermore, electrochemical impedance spectroscopy (EIS) was conducted in a frequency range from 100 mHz to 100 kHz to investigate the ion-transport behavior and electrical resistance (Fig. 36). Significantly, the Nyquist plot of KPL was composed of a semicircle (inset in Fig. 35a) in high frequency range and a straight slope line in low frequency, suggesting good capacitive behavior of the porous material and sufficient electrolyte penetration into the electrode, respectively [157]. On the contrast, no porous structures were found in L and PL, and consequently no featured capacitive behavior was observed. In addition, KPL exhibited extremely smaller general resistance (2.5 Ω), compared to L (>150 Ω) and PL (>150 Ω), though the carbonization occurred at the same temperature. As mentioned above, the difference in resistance could be attributed to the porous structures that provided short ion transportation distance and small transferring resistance, which boosted EDLCs capacitance.

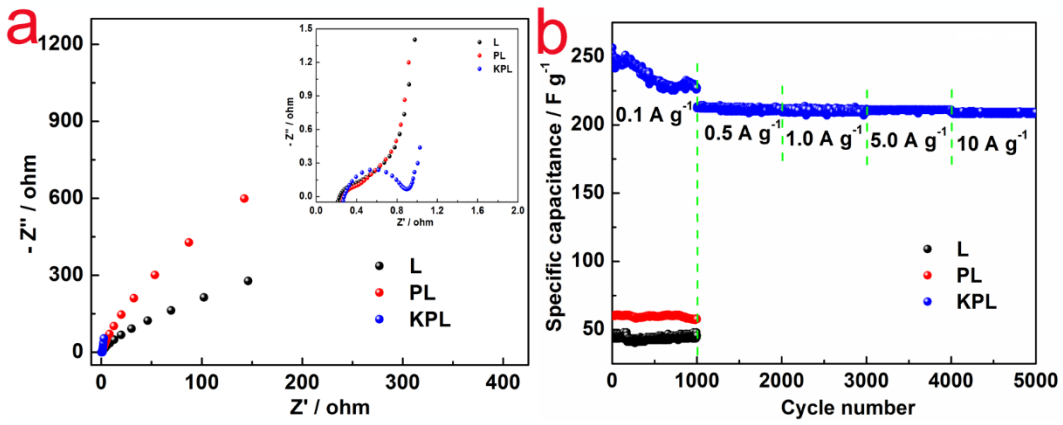

Fig. 36 Nyquist plots of (a) L, PL and KPL electrodes; (b) Cycle life of L, PL and KPL electrodes in 6 mol L^{-1} KOH electrolyte at different current density ranging from 0.1 to 10 A g^{-1}.

Cycle life is another important index for the electrode of EDLCs. Hence the stability of the cells assembled using L, PL and KPL were evaluated by constant current charge and

discharge at different current densities ranging from 0.1 to 10 A g^{-1} (Fig. 36b). It was found that KPL displayed much larger specific capacitance (~248 F g^{-1}) than L (~40 F g^{-1}) and PL (~60 F g^{-1}) at current density of 0.1 A g^{-1} after 1,000 cycles. After subsequent 1,000 cycles at different current densities, almost 100% retention of specific capacitance was achieved, except a little bit decrease in the first 1000 cycles at 0.1 A g^{-1}. Moreover, specific capacitance of 211 F g^{-1} at high current density of 10 A g^{-1} was achieved, which degraded 15% only compared to initial 248 F g^{-1} at 0.1 A g^{-1}. These results indicated the superior stability of KPL as EDLC electrodes. As shown in Table 3, the performance of KPL-based EDLCs was comparable or better than those using carbon materials derived from other biomass when the same type of electrolyte was used.

Table 3 Comparison of specific capacitance of different carbon materials.

Electrode materials	Electrode system	Specific capacitance	Current density	Electrolyte	Reference
N-doped graphene hollow nanospheres	3	381 F g^{-1}	1 A g^{-1}	6 M KOH	[61]
Cyanobacteria derived activated carbon	2	271/222 F g^{-1}	0.1 /1A g^{-1}	6 M KOH	[163]
N-doped porous carbon	2	245 F g^{-1}	0.05 A g^{-1}	6 M KOH	[64]
N-Doped ordered mesoporous carbon	3	227 F g^{-1}	0.2 A g^{-1}	6 M KOH	[62]
Hierarchical N-doped	3	198 F g^{-1}	1 A g^{-1}	6 M KOH	[43]

porous carbon					
N-modified few-layer graphene	3	227 F g^{-1}	1 A g^{-1}	6 M NaOH	[65]
Porous N-doped hollow carbon spheres	3	213 F g^{-1}	0.5 A g^{-1}	6 M KOH	[63]
N-doped porous carbon nanofibers	3	202 F g^{-1}	1 A g^{-1}	6 M KOH	[66]
N-doped cheese-like porous carbon	2	248 F g^{-1}	0.1 g^{-1}	6 M KOH	This work

6.4 Conclusions

This work shows that N-doped carbon can be derived from pyrrole modified lignin. Simultaneous chemical and physical activation using KOH during the heat treatment can effectively create porous N-doped carbon. The activated carbon possesses cheese-like morphology with large specific surface area of 2661 m^2 g^{-1} and mesopores of ~15 nm. Benefited from these characteristics, EDLCs prepared using the N-doped porous activated carbon show high specific capacitance of 248 F g^{-1} at low current density of 0.1 A g^{-1} and 211 F g^{-1} at high current density of 10 A g^{-1} in 6 M KOH solution. The EDLCs also exhibit excellent cycle stability for continuous 1,000 cycles at different current densities. This work indicates that the pyrrole-modified KOH-activated lignin is a promising electrode material for EDLCs.

Chapter 7 Pyrrole modified biomass derived hierarchical porous carbon as high performance symmetrical supercapacitor electrodes©

7.1 Introduction

Supercapacitors are promising energy storage devices due to their long life cycle, high power and energy density, and excellent stability. Based on their working principles, supercapacitors can be divided into two major types: pesudocapacitors and electrochemical double layer capacitors (EDLCs). Pesudocapacitors store energy storage *via* faradic redox reactions where occurs on the surface of electrode materials immersed into an electrolyte [164]. The EDLCs, also referred as symmetric supercapacitors, store energy via electric charge accumulation at the electrode/electrolyte interface [165]. Pesudocapacitors use metal oxides as electrode materials. Among the available metals oxides, RuO_2 displayed excellent capacitance performance but are expensive [166]. To overcome this drawback, alternative metal oxides (such as NiO, MnO_2, Co_3O_4 and WO_3 [146, 167-169]) have been developed. However, the capacitance is still limited by poor conductivity, low power density and poor rate capability [77]. On the other hand, carbon has been used as electrode material for EDLCs due to its stable physicochemical properties, good conductivity, low cost, and abundant source. A well accepted opinion is that carbon material with high specific surface area (SSA) and porosity is particularly suitable for EDLC electrodes. The high SSA can provide enough accessible contact area between the electrolyte and electrode surface, and the porous structure can serve as reservoir and facilitate the electrolyte diffusion from exterior into interior of the electrode material. Porous carbon electrodes have been demonstrated with very high specific

capacitance in carbon EDLCs [78, 79]. As a result, considerable effort has been made to create ideal porous carbon for EDLCs. Among those reported approaches, KOH activation under pyrolysis is considered an efficient way because the chemical activation produces a porous network by etching the physical activation further develops the pores through gasification, and the metallic K expands the carbon lattice by intercalation effect [83, 170]. Based on these synergistic effects, various activated carbon materials with large SSA and high porosity have been developed for EDLCs.

However, the specific capacitance achieved using porous carbon was still not high enough. The relatively low conductivity of porous carbon appeared to be one limiting factor. It was found recently that introducing heteroatom, such as N, B, and S [66, 171, 172], was a promising way to improve the EDLCs performance. Among these dopants, N exhibited more advantages than others because it not only improved conductivity, but also enhanced surface wettability and induced pseudo-capacitance [103, 104, 173]. In addition, the cost of activated carbon is also a big concern for mass production. Compared with conventional carbon nanomaterials (carbon nanotubes, carbon fibers, and graphene), biomass-derived activated carbon is very attractive because of its availability, low cost and sustainability [34, 128, 162, 174]. As a consequence, using N-modified biomass as carbon precursor is expected to be a good strategy to prepare high performance EDLCs.

Herein, the authors report a kind of hierarchical activated carbon derived from pyrrole modified fungus *via* efficient KOH activation. The KOH induced physical and chemical activation, created hierarchical porous structure with high SSA. Meanwhile, N composite was converted into beneficial N species during the pyrolysis process. The activated

carbon was then used to prepare electrodes for EDLCs, which exhibited high specific capacitance, excellent stability, and long life time.

7.2 Experimental

7.2.1 Preparation of activated carbon

Dried fungus (3 g), prepared from pullulans, was mixed with pyrrole (1.5 ml) and 30 ml ethanol in a beaker, followed by stirring at 80 ℃ until the ethanol was evaporated. Then the mixture was heated at 400 ℃ for one hour with a heating rate of 10 ℃ min^{-1} in a muffle furnace (1100 box furnace, Lindberg/Blue M, Thermo Scientific Inc.) under the protection of nitrogen (flow rate was 96 ml min^{-1}). After the precarbonized material was cooled to room temperature, it was mixed with potassium hydroxide (KOH, Fisher Scientific Inc.) in a mass ratio of 1:3 in a steel crucible that contained 30 mL deionized water. The crucible was placed in an oven and dried at 110 ℃ for 24 h. Then, the crucible was transferred into a muffle and activated at 800 ℃ for 1 h with a heating rate of 10 ℃ min^{-1} under N_2 protection (flow rate was 96 ml min^{-1}). Afterwards, the carbonized solids were washed with 30 mL 0.1 mol L^{-1} HCl (Fisher Scientific Inc.) at 110 ℃ for 1 h in a 60 mL polytetrafluoroethylene (PTFE) autoclave to remove the residual KOH and impurities. Finally, the carbon solids was washed several times with deionized water until the pH stabilized at 7. The material was then dried at 105 ℃ overnight in an oven. The carbonized samples were denoted as KPF.

For comparison, samples prepared using the same procedure but without KOH were denoted as PF, and raw fungus directly carbonized with the same procedure as PF but without adding pyrrole was denoted as F.

7.2.2 Preparation of electrodes

Electrodes were prepared by mixing the F, PF or KPF (80 *wt*%) with acetylene black (10 *wt*%) and PTFE (10 *wt*%), and then pressing onto a nickel foam (EQ-bcnf-16m, MTI Corp.) of 1 cm^2 surface area. The electrodes were dried at 60 ℃ for 12 h in an oven. Afterwards, a sandwich structure was formed by placing two pieces of microporous Polypropylene (PP) separator celgard-3501 between two electrodes in a coin cell 2032 type system. Finally, the cell was pressed under a pressure of 1,000 kg cm^{-2} to finish the assembly.

7.2.3 Physical characterization

The surface analysis was performed on a Kratos Axis Ultra high performance X-ray photoelectron spectroscopy (XPS) (Kratos Analytical Ltd.). For high resolution data, the lowest binding-energy C 1s peak was set at 285.0 eV and used as the reference for other elements. Raman spectra were obtained on a Horiba LABRam confocal Raman microscopy system with excitation wavelength of 532 nm from a diode pumped solid state laser. Isothermal adsorption analysis with dry N_2 was carried out at 77 K (liquid nitrogen bath), using ASAP2020 (Micromeritics Inc.) micropore analyzer. The specific surface area was determined by the Brunauer-Emmett-Teller (BET) method and the pore size distribution was calculated according to the density functional theory (DFT) method using non-local density functional theory (NLDFT) analysis for carbon with slit pore model. A transmission electron microscope (TEM) (JEM-2100 LaB6, JEOL) equipped with energy-dispersive X-ray spectroscopy (EDX) was used to study the morphology and microstructure at an acceleration voltage of 200 kV.

7.2.4 Electrochemical characterization

Cyclic voltammetry (CV) and electrochemical impedance spectroscopy tests were measured on an electrochemical work station (SP-150, BioLogical, France) in 6 mol L^{-1} KOH electrolyte. The galvanostatic charge/discharge curves were obtained from a battery test system (BTS series, NEWARE, China).

7.3 Results and discussion

To observe the morphology of F, PF and KPF, TEM and SEM were conducted (Fig. 37). As can be seen (Fig. 37a and b), samples F and PF were strongly aggregated chunks. On contrast, hierarchical and porous structure clearly appeared in the KPF (Fig. 37c and d). In addition, the pore structures was examined by high resolution TEM (Fig. 37e and f), revealing large amount of pores with different sizes. Such a porous network was believed to be originated from KOH activation during the pyrolysis process. As mentioned above, synergistic effects, including etching, gasification and intercalation effect were responsible for pore network formation, porosity enhancement, and lattice expansion, respectively [83]. Such hierarchical morphology could provide large SSA. Moreover, from electrochemical perspective, a smaller resistance and shorter diffusion pathways were created by channels connected with pores of different sizes to facilitate the ion transport [78, 79], and were expected to lead to an improvement in capacitance performance as EDLCs electrodes.

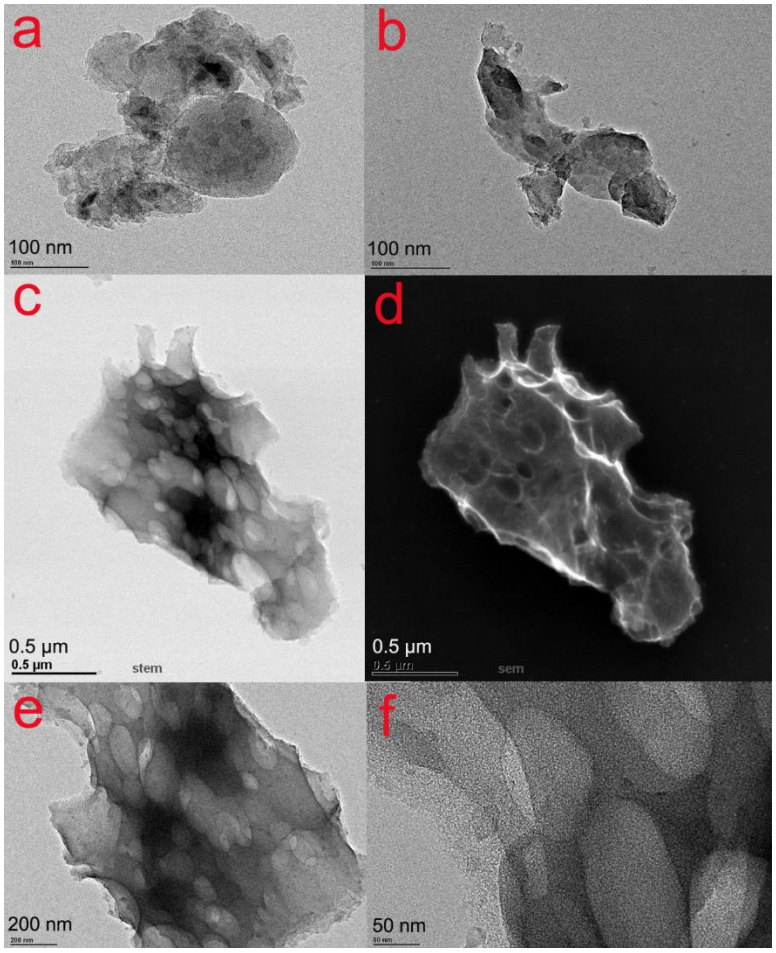

Fig. 37 TEM images of F (a), PF (b) and KPF (c, e and f); SEM image of KPF (d).

To verify the speculation on high SSA and pore structure observed in TEM images, N_2 adsorption/desorption isotherm measurement was performed (Fig. 38a). The plot showed a typical type I isotherm according to IUPAC classification and high SSA up to 2959 m^2 g^{-1}. The inset in Fig. 38a depicted pore size distribution of KPF. A strong peak located at 15 nm was showed, indicating the pore network mainly consisted of mesopores, while micropore and macropore took a small percentage. Among these three kinds of pores, mesopores were believed to offer lower ion-transport resistance *via* mesoporous channels [78, 155, 175-177]. Micropores would impose a long diffusion distance (> 5 mm) and a high ion-transport resistance led to a large electrode-potential drop (IR_{drop}) and a low ion-

accessible surface area at high current values [67]. Macropores played a role as ion-buffering reservoirs, which would lead to a decreased diffusion distance [78]. Raman spectrum was used to characterize the carbon structures of KPF. As shown in Fig. 38b, two characteristic peaks located at around 1340 cm^{-1} and 1580 cm^{-1} were presented, which were assigned to *D*-band and *G*-band, respectively [102]. The *D*-band was related with the vibration of the carbon atoms with dangling bonds in plane terminations of the disordered structure, while *G*-band reflected the vibration of sp^2-bonded carbon atoms [101, 102].

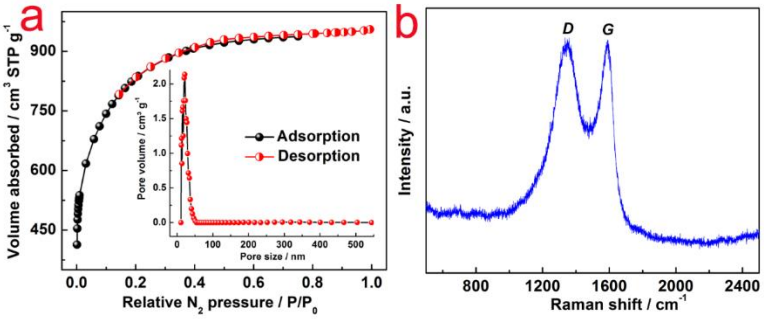

Fig. 38 (a) N_2 sorption-desorption isotherms of KPF. The insert in (a) shows pore size distribution; (b) Raman spectra of KPF.

XPS was employed to characterize the carbon, oxygen and nitrogen chemical states in the KPF sample (Fig. 39). As shown in Fig. 39a, the high resolution C 1s spectrum was deconvoluted into five peaks at binding energy of *ca.* 285.2, 286.3, 287.5, 289.1 and 291.0 eV, corresponding to C-C, C-O/C-OH, C=O/C-N, COOH, and CO_2/CO_3^{2-} bonds and functional groups, respectively [58, 156]. In addition, high resolution spectrum of O1s was deconvoluted into three peaks (Fig. 39b), which were assigned to O-I, O-II and O-III at *ca.* 531 eV, 532 eV, and 535 eV, respectively. The three species O represented C=bond quinone type groups for O-I, C-OH phenol groups and/or C-O-C ether groups

for O-II, and chemisorbed oxygen for COOH carboxylic groups and/or water for O-III, respectively. However, it was believed that only O-I represented the pseudo-capacitance effect [157]. Besides, two peaks were detected at binding energy *ca.* 398.9 and 401.2 eV for N species, and were attributed to pyridinic-N, and quaternary-N, respectively (Fig. 39c). As reported previously [103, 104], N introduction would improve the conductivity and pyridinic-N could lead to great pseudocapacitance effect, both of which would enhance the capacitance performance.

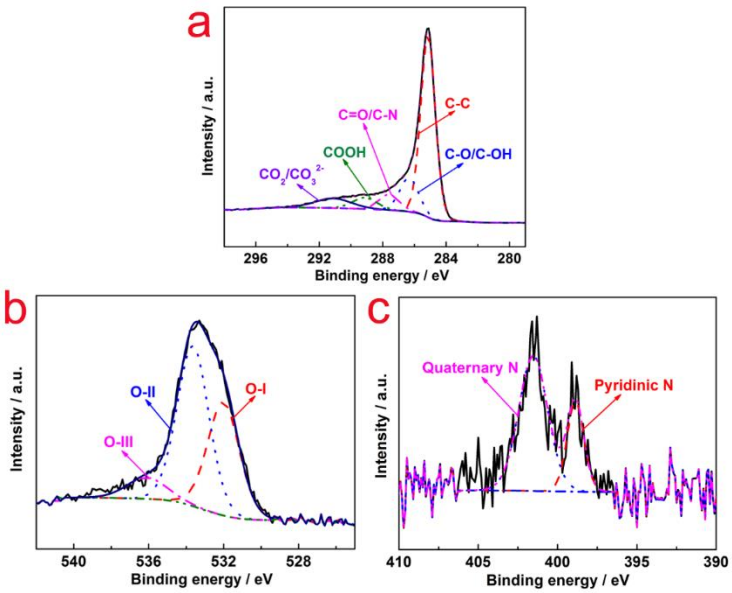

Fig. 39 High resolution C 1s (a), O 1s (b) and N 1s (c) XPS spectra of KPF.

To verify the performance of prepared electrode materials, electrochemical measurements were employed. As presented in Fig. 40a c and e, the CV tests were conducted at various scanning rates ranging from 5 to 300 mV s^{-1} for F, PF and KPF, respectively. The F and PF electrodes exhibited distorted rectangular shapes even at low scanning rate, while typical rectangular shape was observed for KPF electrode. In addition, the KPF electrodes retained rectangular shape CV curves when the scanning rate increased from 5

mV s^{-1} to high 300 mV s^{-1}. These results indicated the high capacitive performance with rapid charging-discharging characteristics due to efficient charge transfer and electrolyte diffusion within the porous KPF [162].

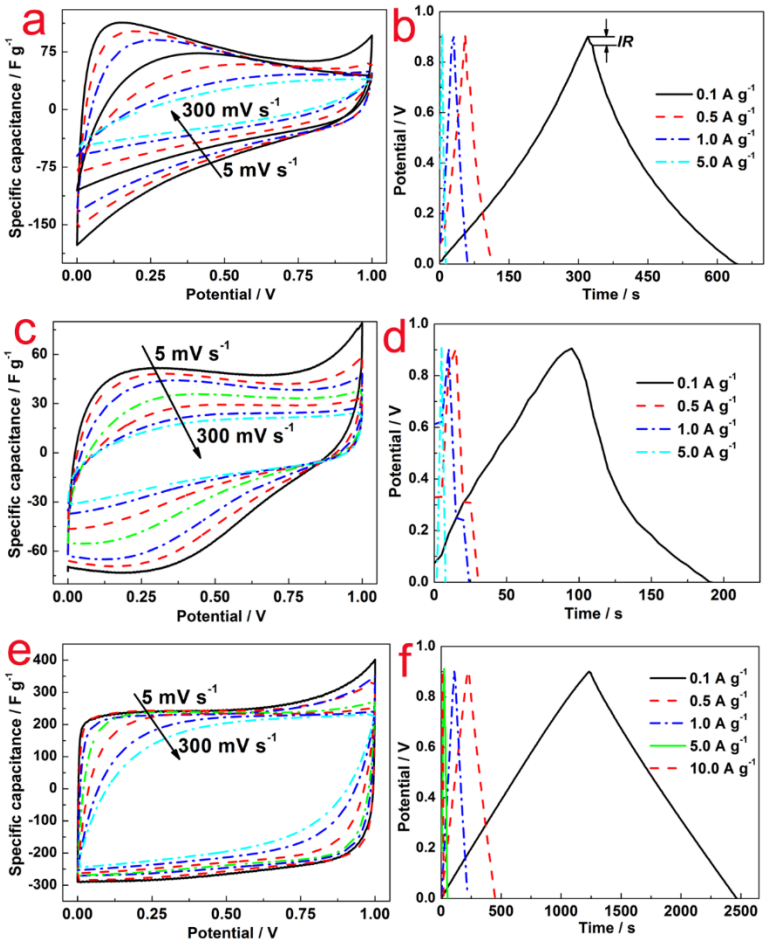

Fig. 40 CV curves of F (a), PF (c) and KPF (e) electrodes at various scanning rates ranging from 5 to 300 mV s^{-1}; and galvanostatic charge/discharge curves of F (b), PF (d) and KPF (f) electrodes at different current densities ranging from 0.1 to 10 A g^{-1}.

The capacitive performance was further evaluated using the following equation [55] in the two-electrode system:

$$C = \frac{2I\Delta t}{m\Delta v} \quad (13)$$

where C is the specific capacitance, I is the charge/discharge current, Δt is the corresponding charge or discharge time, m is the mass of active materials on single electrode, and Δv is the total corresponding potential change. As can be observed in Fig. 40a and c, the specific capacitance was only around 60 F g^{-1} for both F and PF electrodes. On contrast, high specific capacitance of 245, 243, 238, 234, 233, 223 and 204 F g^{-1} was obtained at scanning rate of 5, 10, 20, 50, 100, 200 and 300 mV s^{-1} for KPF, respectively. Combining the physical measurements results, it was deduced that the high specific capacitance could be attributed to large specific surface area, hierarchical porous structure, and high degree of graphitization of KPF.

Galvanostatic charge/discharge measurements were performed at different current densities ranging from 0.1 to 10 A g^{-1} for F, PF and KPF (Fig. 40b, d and f). Differing from the comparable symmetric triangle shape and an obvious IR_{drop} for F and PF electrodes, KPF displayed a symmetric triangle shape, suggesting a very small internal resistance and less energy being wasted during charge/discharge process [67].

Fig. 41a shows Nyquist plots that was obtained from KPF electrodes in 6 mol L^{-1} KOH electrolyte. In general, the total resistance (~2.5 Ω) consisted of bulk electrolyte resistance (R_1), interfacial impedance between electrode and bulk solution (R_2), and the impedance associated with intra-particle pores (R_3), corresponding to x-intercept at the highest frequency region, semicircle at the middle frequency region and spike at the low frequency region, respectively [106]. R_1 and R_2, related to the electrolyte solution, while

R_3 depended on both electrode materials and electrolytes. This result was in consistent with the expected low resistance, hierarchical structure and high SSA confirmed above.

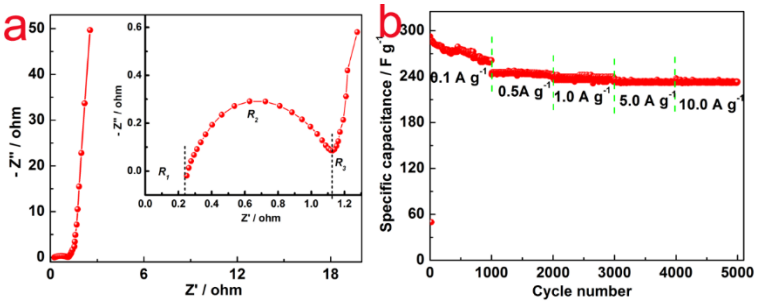

Fig. 41 (a) Nyquist plots of KPF electrodes; (b) Cycle life of KPF electrodes in 6 mol L^{-1} KOH electrolyte at different current density ranging from 0.1 to 10 A g^{-1}.

As another significant parameter of EDLCs performance, cycling life of KPF electrodes was recorded in 6 mol L^{-1} KOH electrolyte at different current density ranging from 0.1 to 10 A g^{-1}. As shown in Fig. 41b, large specific capacitance of 270, 243, 235, 233 and 232 F g^{-1} were obtained at current density of 0.1, 0.5, 1.0, 5.0 and 10.0 A g^{-1} for each individual 1,000 cycles, respectively. Apart from a little bit degradation in the first 1,000 cycles at current density of 0.1 A g^{-1}, excellent cycle stability (almost 100% retention) was displayed, which demonstrated the excellent stability of KPF as electrode materials for EDLCs.

7.4 Conclusions

N-doped hierarchical porous carbon has been successfully prepared from pyrrole modified abundant fungus as high-performance electrodes for EDLCs. The prepared KPF carbon exhibited extraordinarily large SSA (2959 m^2 g^{-1}) and porosity, which served as ion diffusion channels and electrolyte reservoir contributed to capacitance enhancement. Large specific capacitance of 270 F g^{-1} at low current density of 0.1 A g^{-1} and 232 F g^{-1} at

high current density of 10 A g^{-1} was obtained in 6 M KOH solution. In addition, excellent cycle stability for continuous 1,000 cycles at different current densities was achieved for assembled EDLCs. This work demonstrated the pyrrole modified biomass derived porous carbon was a promising electrode material for electric energy storage.

Chapter 8 Porous carbon derived from aniline-modified fungus for symmetrical supercapacitor electrodes©

8.1 Introduction

Supercapacitors have attracted considerable attention due to their high power density, rapid charge/discharge capacity, long life cycle, and excellent stability [16, 178, 179]. Generally, supercapacitors can be classified into two major types based on the working mechanisms: pseudocapacitors and electrical double-layer capacitors (EDLCs). Different from pseudocapacitors, which depends on reversible Faradaic reactions occurred at the surface of electrode materials, EDLCs store electrical energy by electrostatic accumulation of charges in the electric double-layer near the electrode/electrolyte interfaces [180]. Likewise, transition metal oxides, hydroxides and their compounds are used as electrode materials for pseudocapacitors [146, 167, 181], while carbon materials are suitable for EDLCs electrodes. Although pseudocapacitors possess high specific capacitance and energy density, the low conductivity of the electrode materials, poor rate capability, and high cost greatly restrict their applications [182]. In the contrast, carbon materials exhibit excellent conductivity and high physicochemical properties with low cost, leading to superior rate capability and long life cycle for EDLCs.

So far, carbon materials used for EDLCs electrodes included carbon nanotubes, activated carbon, graphene and carbon fibers [163, 183-185]. Of these materials, activated carbon is considered a promising candidate for EDLCs electrode material owing to high specific surface area (SSA), large porosity, and excellent conductivity; factors that are important

for EDLCs performance. Activated carbon are typically prepared *via* physical or chemical activation to produce porous structure with high SSA and wide pore size distribution (micropore, mesopore, and macropores). It is believed that high SSA will provide enough contact area between the electrodes and electrolyte, while pores with different sizes will serve as ion channels and reservoirs of electrolyte to shorten the ion diffusion distance. Both of these factors contribute to capacitance performance [186]. However, the capacitance performance of activated carbon based electrodes is still limited and higher specific capacitance is greatly desired.

In recent years, introducing heteroatoms (P, N and B) into activated carbon was found to be efficient to improve EDLCs performance because of the induced pseudo-capacitance *via* reversible redox reaction and the improved wettability [92, 187, 188]. In particular, N-doped carbon materials have received considerable attention and a variety of methods were explored to introduce nitrogen. Although carbonizing biomass that contains nitrogen appeared an efficient approach to achieving N-doped carbon, low-cost N-containing biomass species are very limited and the N concentration is low after pyrolysis. Alternatively, using N-rich chemicals to modify low-cost biomass becomes more attractive to preparing N-doped porous carbon *via* combined pyrolytic chemical activation.

In this work, N-rich aniline was used to modify fungus and the modified raw material was subsequently activated by KOH to obtain N-doped porous carbon. The activated porous carbon exhibited high SSA and desired porosity suitable for EDLC electrode materials. The performance of supercapacitors prepared with the N-doped porous carbon is reported.

8.2 Experimental

8.2.1 Preparation of activated carbon

Fungus (3 g), aniline (1.5 ml) and 30 ml ethanol were added into a flask with 30 ml ethanol, followed by stirring at 80 ℃ until the ethanol was evaporated. Then the mixture was heated at 400 ℃ for one hour with a heating rate of 10 ℃ min^{-1} for 1 h in a muffle furnace (1100 box furnace, Lindberg/Blue M, Thermo Scientific Inc.) under the protection of nitrogen (flow rate was 96 ml min^{-1}). After the precarbonized material was cooled to room temperature, it was mixed with potassium hydroxide (KOH, Fisher Scientific Inc.) in a mass ratio of 1:3, in a steel crucible also containing 30 mL deionized water. The crucible was placed in an oven and dried at 110 ℃ for 24 h. Then, the crucible was transferred into a muffle and activated at 800 ℃ for 1 h with a heating rate of 10 ℃ min^{-1} under N_2 protection (flow rate was 96 ml min^{-1}). Afterwards, the carbonized solids were washed with 30 mL 0.1 mol L^{-1} HCl (Fisher Scientific Inc.) at 110 ℃ for 1 h in a 60 mL polytetrafluoroethylene (PTFE) autoclave to remove the residual KOH and impurities. Finally, the carbon solids was washed several times with deionized water until the pH stabilized at 7. The material was then dried at 105 ℃ overnight in an oven. The carbonized samples were denoted as N-AC. Raw fungus and dried mixture of fungus and aniline were carbonized following the same procedures of N-AC preparation but in the absence of KOH, the products were donated as C and N-C, respectively.

8.2.2 Preparation of electrodes

Electrodes were prepared by mixing the prepared carbon samples C, N-C and N-AC (80 *wt*%) with acetylene black (10 *wt*%) and PTFE (10 *wt*%), and then pressing onto a

surface area of 1 cm^2 nickel foam (EQ-bcnf-16m, MTI Corp.). The electrodes were dried at 60 ℃ for 12 h in an oven. Afterwards, a sandwich structure was formed by placing two pieces of microporous PP separator celgard-3501 between two electrodes in a coin cell 2032 type system. Finally, the cell was pressed under a pressure of 1,000 kg cm^{-2} to finish the assembly.

8.2.3 Physical characterization

X-ray photoelectron spectroscopy (XPS) was performed on an SSX-100 system (Surface Science Laboratories, Inc.) equipped with a monochromated Al K_α X-ray source. For high resolution data, the lowest binding-energy C 1s peak was set at 285.0 eV and used as the reference for all of the other elements. Raman spectra were obtained on a Horiba LABRam confocal Raman microscopean with excitation wavelength of 532 nm from a diode pumped solidstate laser. Isothermal adsorption analyses with N_2 were carried out at 77 K (liquid nitrogen bath), using ASAP2020 Micropore analyzer. The specific surface area was determined by the Brunauer-Emmett-Teller (BET) method and the pore size distribution was calculated according to the density functional theory (DFT) method using NLDFT analysis for carbon with slit pore model. Elemental analysis was conducted using Perkin Elmer 2400 II for C, H and N analysis and LECO Tru Spec Micro was used to analyze O with oxygen module. A transmission electron microscope (TEM) (JEM-2100 LaB6, JEOL) equipped with energy-dispersive X-ray spectroscopy (EDX) was used to study the morphology and microstructure of the materials at an acceleration voltage of 200 kV.

8.2.4 Electrochemical characterization

Cyclic voltammetry (CV) and electrochemical impedance spectroscopy tests were measured on an electrochemical work station (SP-150, BioLogical, France) in 6 mol L^{-1} KOH electrolyte. The galvanostatic charge/discharge curves were obtained from a battery test system (BTS series, NEWARE, China).

8.3 Results and discussion

Fig. 42a and b show TEM images of C and N-C, respectively. The C and N-C samples displayed chunk shape without pores. On the other hand, the N-AC sample exhibited a lot of pores with diverse sizes as observed in STEM and SEM image of N-AC (Fig. 42d). The porous structure could also be observed in a tomography video. Such a significant difference was attributed to KOH activation since this was the only difference in preparing the materials. As reported by *Kaskel* [83], etching, gasification and K intercalation were responsible for pore formation, porosity perfection and lattice expansion during the activation process, respectively. Therefore, both chemical activation and physical activation were involved in creating the porous structure, leading to high SSA and porosity of N-AC.

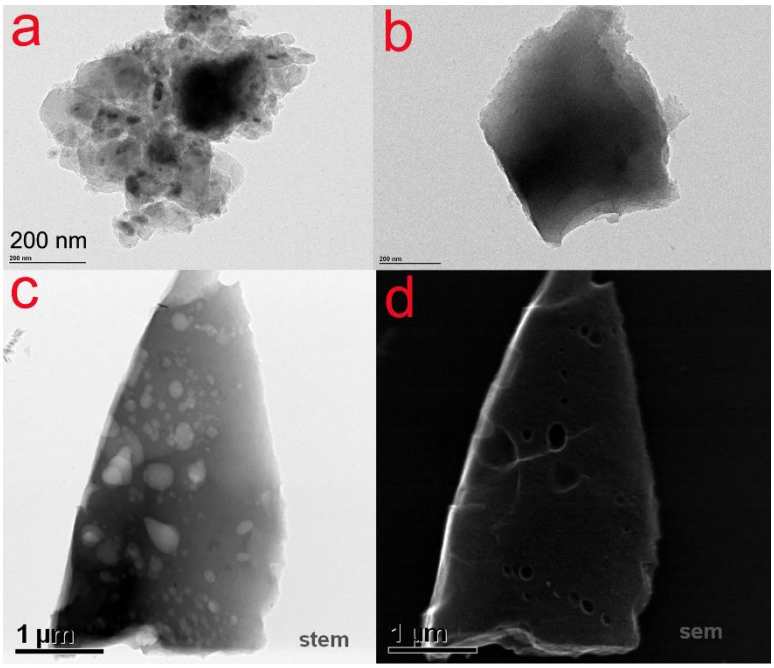

Fig. 42 TEM images of C (a) and N-C (b) STEM (c) and SEM (d) image of N-AC.

To evaluate the surface area and pore structure of N-AC, N_2 sorption-desorption isotherm was conducted (Fig. 43a). High SSA of 2339 m^2g^{-1} was obtained for N-AC, which offered karge contact surface area between the electrodes and electrolyte. In addition, the pore size distribution suggested that the pore sizes centered at 27 nm and 34 nm with some micropores and macropores, which would serve as reservoirs and channels for the electrolyte [186]. Eventually, these features were expected to improve the capacitance. Raman spectra of C, N-C and N-AC was employed to further characterize the carbon structure. As presented in Fig. 43b, two characteristic peaks located at ~1346 and 1580 cm^{-1} were revealed, which was assigned to *D-band* and *G-band*, respectively. The *D-band* reflected degree of disordered graphite with A_{1g} symmetry, while *G-band* was associated E_{2g} mode of sp^2 carbon domains [57]. Meanwhile, the intensity of ratio between *D-band* and *G-band* represented the degree of graphitization, lower value indicated higher graphitization. Same ratio value of 0.96 was obtained for all the three

samples, implying that they had similar degree of graphitization, which could be attributed to the same carbonization temperature (800 ℃) and process time.

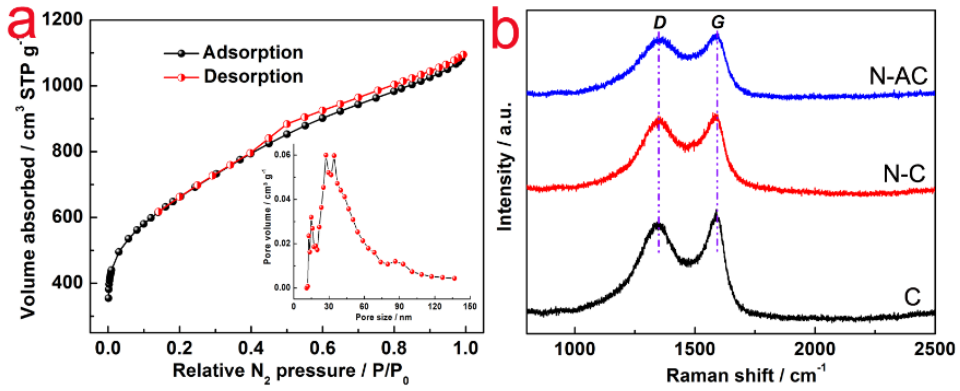

Fig. 43 (a) N_2 sorption-desorption isotherms of N-AC. The insert in (a) shows pore size distribution of N-AC; (b) Raman spectra of C, N-C and N-AC.

XPS was conducted to investigate the chemical state of N-AC (Fig. 44). Deconvolution of the C 1s spectra (Fig. 45a) showed the most pronounced peak being graphite-like carbon (C-C) at 285 eV and oxygen-containing groups located at different binding energy *e.g.*, C-C (), C-O/C-OH (~286 eV), C=O (~287 eV), COOH (~289 eV), and CO_2/CO_3^{2-} (~291 eV) [59]. These surface functional groups improved the hydrophilic nature of the N-AC and resulted in easy access of the electrolyte to the internal walls of the pores. In high resolution spectrum of O1s, three types of O species located at 531 eV, 532 eV, and 535 eV, respectively, were detected (Fig. 46b), which were associated with C=O groups (carbonyl/quinone), carbonyl oxygen atoms (phenol/ether) and oxygen atoms (carboxylic groups COOH and/or chemisorbed O_2/H_2O), respectively [157]. This result was consistent with C1s analysis that these functional groups could improve the wettability of N-AC electrodes and provided more accessible surface for aqueous electrolyte and eventually led to enhanced capacitance. In addition, high resolution spectrum of N1s was

deconvoluted into three peaks at ~399, 401 and 404 eV, which could be attributed to quaternary-N, pyridinic-N and N oxides of pyridinic-N, respectively. It was reported that pesudocapacitance behavior between the ions of electrolytes and the carbon electrode surface could be induced by pyridinic-N [124], which contributed to capacitance performance.

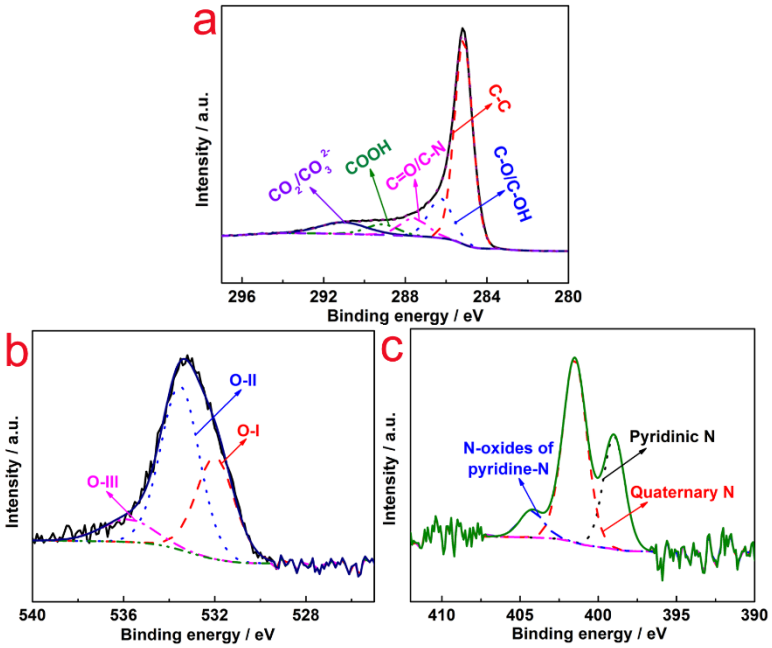

Fig. 47 High resolution C 1s (a), O 1s (b) and N 1s (c) XPS spectra of N-AC.

Fig. 48 illustrates the CV curves of C (a), N-C (c) and N-AC (e) electrodes at various scanning rates ranging from 5 to 300 mV s^{-1} to access the specific capacitance. Distorted rectangular shapes were observed for both C and N-C electrodes, which were significantly different from a typical rectangular shape with a big loop that the N-AC electrodes exhibited. These results indicated that N-AC electrodes possessed better capacitive behavior and higher specific capacitance. In addition, almost no distortion was observed for N-AC electrodes in contrast to the C and N-C electrodes even at increased

scanning rates. This result implied efficient charge transfer and electrolyte diffusion in the porous N-AC [162]. Moreover, to accurately evaluate the specific capacitance, the following equation [189] was used:

$$C = \frac{2\int I dv}{m\Delta v / \Delta t} \tag{14}$$

where C is the specific capacitance, I is the charge/discharge current, Δt is the corresponding charge or discharge time, m is the mass of active materials on single electrode, and Δv is the total corresponding potential change. The largest specific capacitances were 70 and 20 F g^{-1} for the C and N-C electrodes, respectively, assuming ideal rectangular CV curves. However, the specific capacitance of N-AC reached 231, 229, 228, 225, 223, 219 and 209 F g^{-1} at scanning rate of 5, 10, 20, 50, 100, 200 and 300 mV s^{-1}, respectively. Such a high specific capacitance could be attributed to the large SSA, porous structure, N doping and high degree of graphitization of N-AC. In addition, galvanostatic charge/discharge curves of C, N-C, and N-AC at different current densities are shown in Fig. 48b, d and f, respectively. Comparison with C and N-C, a symmetric triangular shape curve was displayed and no obvious Ohmic drop (IR_{drop}) was observed, demonstrating excellent electrochemical reversibility of N-AC [67].

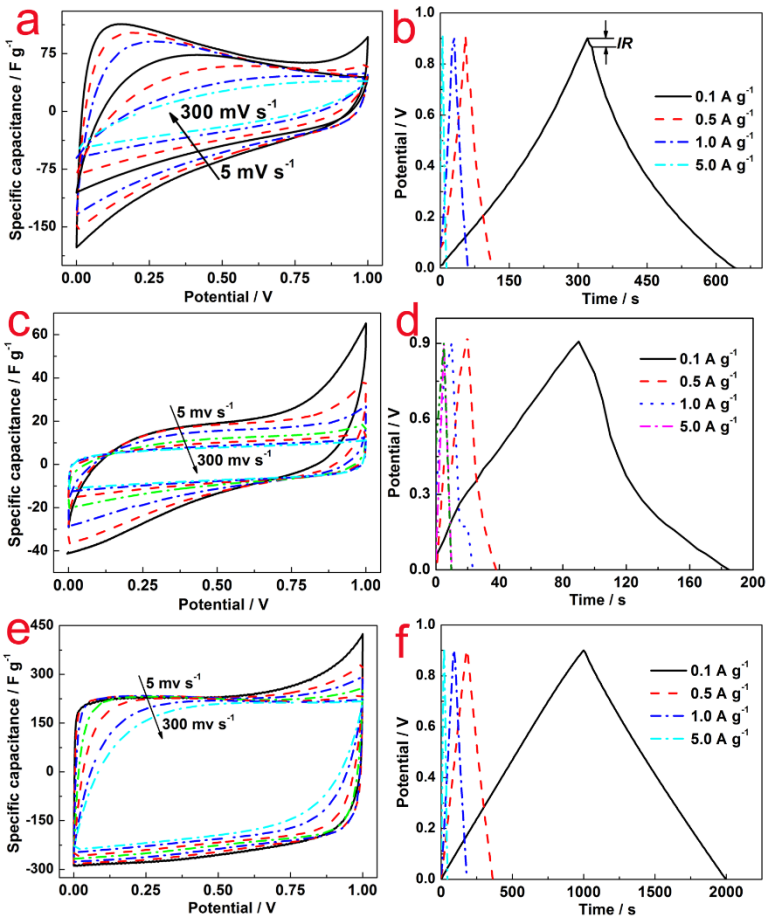

Fig. 48 CV curves of C (a), N-C (c) and N-AC (e) electrodes at various scanning rates ranging from 5 to 300 mV s^{-1}; and galvanostatic charge/discharge curves of C (b), N-C (d) and N-AC (f) electrodes at different current densities ranging from 0.1 to 5 A g^{-1}.

Nyquist plots obtained from KPF electrodes in 6 mol L^{-1} KOH electrolyte are shown in Fig. 49a. Typically, the resistance (3.0 Ω) consisted of bulk electrolyte resistance (0.8 Ω), interfacial impedance (1.2 Ω) and intra-particle impedance (1.0 Ω), which corresponded to *x*-intercept at the highest frequency region (R_1), semicircle at the mid-frequency region (R_2), and the spike at the low-frequency region (R_3) [106]. Among these three types of resistance, R_1 and R_2 were related to the electrolyte solution, and R_3 was associated with

intra-particle pores. This was in consistence with the porous structure, high SSA and good conductivity [106].

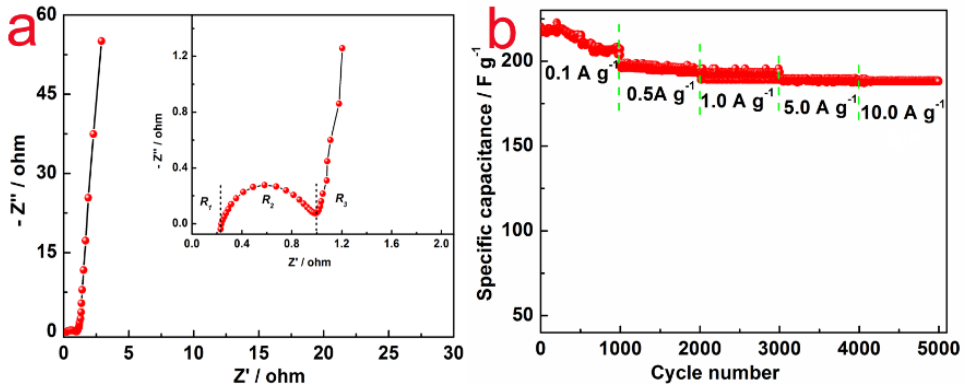

Fig. 49 (a) Nyquist plots of N-AC electrodes; (b) Cycle life of N-AC electrodes in 6 mol L^{-1} KOH electrolyte at different current density ranging from 0.1 to 10 A g^{-1}.

Rate capability is an important feature of EDLCs. Cycle life of N-AC electrode was recorded with 6 mol L^{-1} KOH electrolyte at different current density ranging from 0.1 to 10 A g^{-1}. As shown in Fig. 49b, specific capacitance of 218, 196, 192, 190 and 190 F g^{-1} were obtained at current density of 0.1, 0.5, 1.0, 5.0 and 10.0 A g^{-1} for 5000 cycles, respectively. The specific capacitance of N-AC during the cycling kept almost 100% with only a little bit fluctuation in the initial 1000 cycles, indicating excellent stability and long life time of N-AC electrode materials.

8.4 Conclusions

N-doped porous carbon derived from aniline modified fungus has been prepared *via* efficient KOH activation. Porous structure with high SSA of 2339 m^2g^{-1}, good conductivity, and N doping could be obtained as a result of combined physical and chemical effect during the pyrolysis, which subsequently facilitated capacitance

improvement. The N-doped active carbon exhibited high specific capacitance of 218 and 190 F g^{-1} at low and high current density of 0.1 and 10.0 A g^{-1} in 6 M KOH solution, respectively. Moreover, superior stability was demonstrated with 5000 charge-discharge cycles at different current densities for assembled EDLCs.

Chapter 9 Plasma-assisted fabrication of graphene for symmetric supercapacitors©

9.1 Introduction

Symmetric supercapacitors are also known as electrical double-layers capacitors (EDLCs). Differing from pseudocapacitors, carbon-based materials are used as electrodes in EDLCs and their capacitance is achieved by accumulating charges at the interface between the electrolyte and electrode materials [190]. A variety of carbon materials, including carbon nanotubes, carbon fibers, activated carbon and graphene, have been developed for achieving high performance EDLCs. Of these materials, graphene has attracted considerable attention due to its superior properties.

Graphene has been considered a revolutionary materials since it was first discovered by Geim and co-workers in 2004 [35]. Superior electrical conductivity, high theoretical surface area (2675 $m^2 g^{-1}$), excellent chemical resistance, and high mechanical strength make graphene an outstanding material for biosensors [191], energy storage devices (supercapacitors, Li-ion battery) [192, 193] and hydrogen storage [194]. Considerable efforts have been devoted to developing simple and efficient methods for preparing graphene, including chemical vapor deposition (CVD) [195, 196], mechanical exfoliation [197], epitaxial growth on substrate [198], solvothermal synthesis [199], and reduction of graphene oxide (GO) [200]. These methods required high temperatures and sophisticated equipment to tolerate the harsh reactions. Thus, manufacturing of graphene was inefficient and energy intensive, although each individual method possessed some unique advantages.

In this work, graphene was prepared *via* an efficient plasma exfoliation method, which could be conducted at room temperature. The plasma exfoliation mechanism was revealed by combining optical emission spectroscopy study with microstructure analysis. The prepared graphene was used as EDLCs electrode materials and excellent capacitance performance was demonstrated.

9.2 Experimental

9.2.1 Preparation of graphite oxides

Graphite oxides were prepared by a modified Hummers` method. Firstly, graphite (2.5 g, Fisher Scientific) was added into concentrated sulfuric acid (75 ml, Fisher Scientific) and the mixture was stirred at 0 ℃ for 4 h. Then, sodium nitrate (1.25 g, Fisher Scientific) was slowly added under vigorous stirring. Afterwards, potassium permanganate (7.5 g, Fisher Scientific) was slowly added and reacted at room temperature for 12 h under stirring. Then, 25 ml deionized water was gently added into the mixture and the temperature was kept at 98 ℃. Additional 75 ml deionized water was added slowly. After 4 h, 7.5 ml 30 *wt*% hydrogen peroxide (Fisher Scientific) was dropwise added and the color of the solution turned from brown to yellow. The prepared colloid was transferred into a dialysis tubing (14, 000 MWCO Daltons, Fisher Scientific) to dialyze in deionized water for 2 days and change deionized water every 2 h. Finally, the dialyzed sample was further separated by centrifugation at 8, 000 rpm till the pH was close to 7, and then dried at 60 ℃ in a vacuum oven for 24 h. The prepared graphite oxides were donated in short for GO.

9.2.2 Preparation of graphene

A dielectric barrier discharge plasma system was used to prepare graphene from the GO. The plasma system (Fig. 50) consisted of a quartz tube of 2.5 cm in diameter and 10 cm long that severed as a vacuum chamber, a mechanical pump, a vacuum gauge, a gas flow controller, two copper electrodes of ~2×2 cm attached to the outside surface of the quartz tube, and a 13.56 MHz RF power supply with matching network. Firstly, 200 mg GO was placed into the quartz tube in between the two copper electrodes. Then, the tube was evacuated with the vacuum pump down to ~10 mTorr and purged with the process gas (i.e. nitrogen, oxygen, or methane). This step was repeated at least three times to make sure the residual air in the tube was negligible. After that, the gas flow was adjusted using a needle valve to maintain a stable pressure of ~3 Torr. Then the RF power was turned on with about 20 W input power and the matching network was tuned to achieve almost zero watt reflection power. The RF power was then increased to 70 W, at which the GO was exfoliated. As the exfoliation was completed in seconds once the RF power reached ~70 W, the sample temperature remained at below 60°C as measured by a thermocouple immediately after the RF power was switched off. After the exfoliation, the RF power, gas flow, and vacuum valves were turned off in sequence and the quartz tube was vented to collect the exfoliated sample. Corresponding to the plasma gas, the prepared samples were denoted as GO-O_2, GO-N_2, and GO-CH_4.

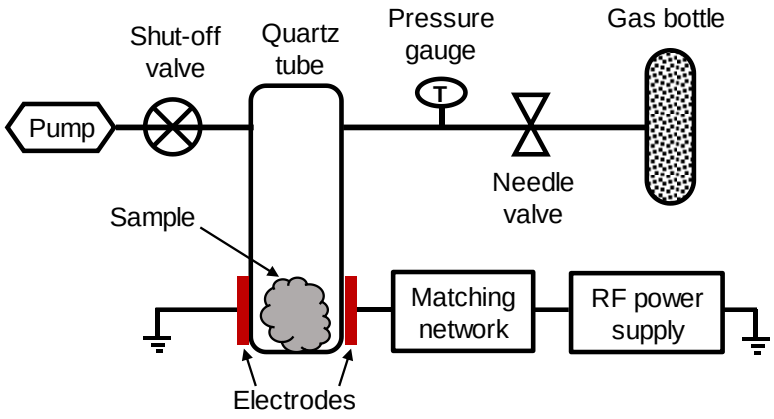

Fig. 50 Schematic diagram of designed plasma system.

9.2.3 Preparation of electrodes

Electrodes materials were made of graphene samples, acetylene black and PTFE with mass ratio of 8:1:1. After mixing, the slurry of mixture was pressed onto a nickel foam (EQ-bcnf-16m, MTI Corp.) with 1 cm^2 surface area. Then, the electrodes were put into an oven at 60 ℃ for 12 h to dry. Prior to assembling a symmetric supercapacitor, two electrodes with similar masses were first prewetted with 6 mol L^{-1} KOH electrolyte, subsequently, a sandwich structure was formed by placing two pieces of microporous Polypropylene (PP) separator (celgard-3501) between two electrodes in a CR2032 coin cell. Then, the cell was pressed under a pressure of 1,000 kg cm^{-2} to seal.

9.2.4 Physical characterization

The microstructure of the samples was characterized by X-ray diffraction (XRD) (Rigaku Smartlab, Rigaku Americas, Inc. USA). The morphology of the prepared samples was confirmed by transmission electron microscope (TEM) (JEM-2100 LaB6, JEOL, Japan) at an acceleration voltage of 200 kV. An optical spectrometer (USB2000+, Ocean Optics, Inc. USA) was used to record the plasma emission spectrum.

9.2.5 Electrochemical characterization

Electrochemical measurements, including cyclic voltammetry (CV) and electrochemical impedance spectroscopy, were conducted on SP-150 electrochemical work station (BioLogical, France). The galvanostatic charge/discharge tests were performed on a battery test system (BTS series, NEWARE, China).

9.3 Results and discussion

Fig. 51 shows GO before and after being treated by the plasma. Note that the shape of GO significantly changed from gel pieces into dark powder, indicating the GO structure was significantly altered due to the plasma exfoliation.

Fig. 51 Photos of GO before and after being treated by plasma.

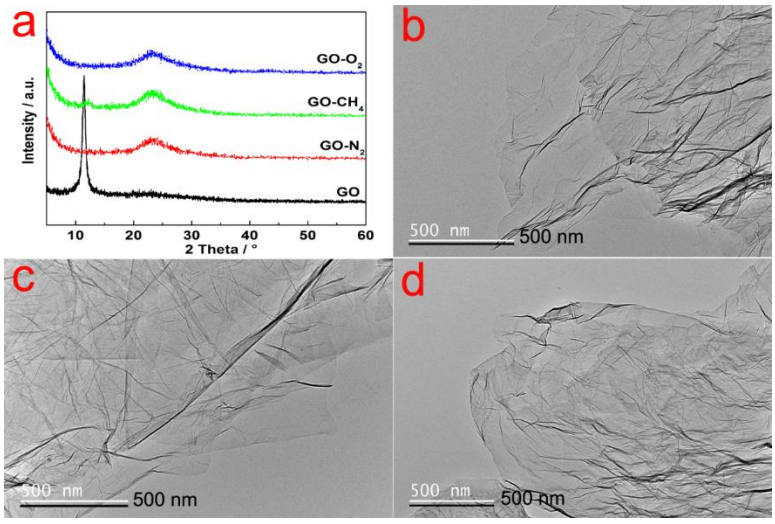

Fig. 52 XRD patterns (a) of GO, GO-N_2, GO-CH_4 and GO-O_2, and TEM images of GO-N_2 (b), GO-CH_4 (c), and GO-O_2 (d).

To verify the sample structure, XRD was conducted (Fig. 52a). As can be seen, the GO sample exhibited a characteristic peak located at ~11º, which was assigned to (001) reflection of GO. After exfoliation, the characteristic peak of GO at 11º was vanished, but a broad peak centering at 24º, corresponding to (002) diffraction pattern of graphitic structure, was observed for samples GO-N_2, GO-CH_4 and GO-O_2. These results confirmed that graphene was successfully prepared. The peak disappeared at the small diffraction angle (~11º) but appeared at a higher angle (~24º), which indicated that the interlayer spacing decreased after the exfoliation, implying the oxygen in GO was removed [201]. To further confirm the sample microstructure, TEM analysis was carried out (Fig. 52b, c and d). The crumply surface was the typical morphology of graphene or graphene nanosheets.

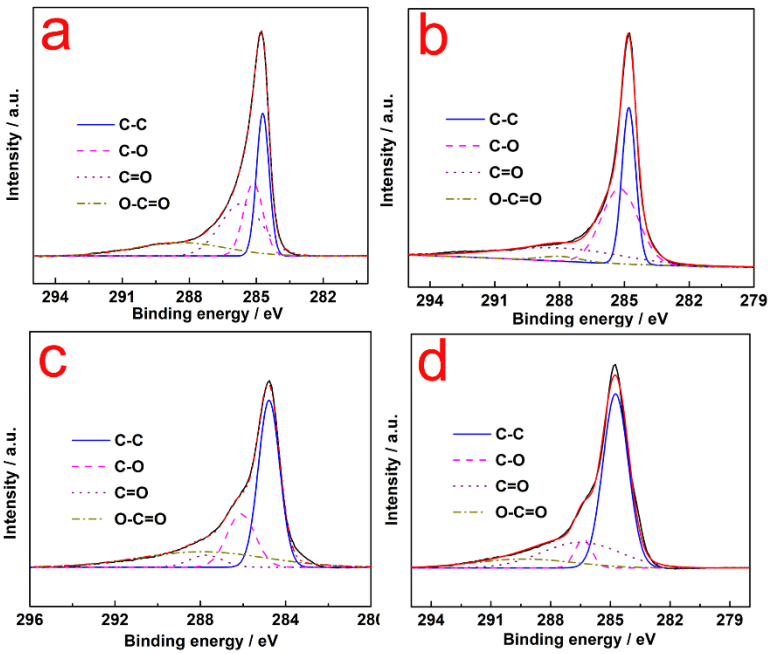

Fig. 53 High-resolution C 1s XPS spectrum of GO (a), GO-N_2 (b), GO-CH_4 (c) and GO-O_2 (d).

XPS characterization was performed to analyze the carbon bonding congurations in all the samples (Fig. 53). The high resolution C1s spectra were deconvoluted into four peaks located at binding energies of 284.5, 286.2, 287.9 and 289.0 eV, which corresponded to C-C, C-O, C=O and O-C=O, respectively [202]. The signal intensity of oxygen-containing bonds such as C=O, O-C=O became weaker than that of the untreated sample, which indicated the deoxygenation process accompanying the reduction of GO [202, 203].

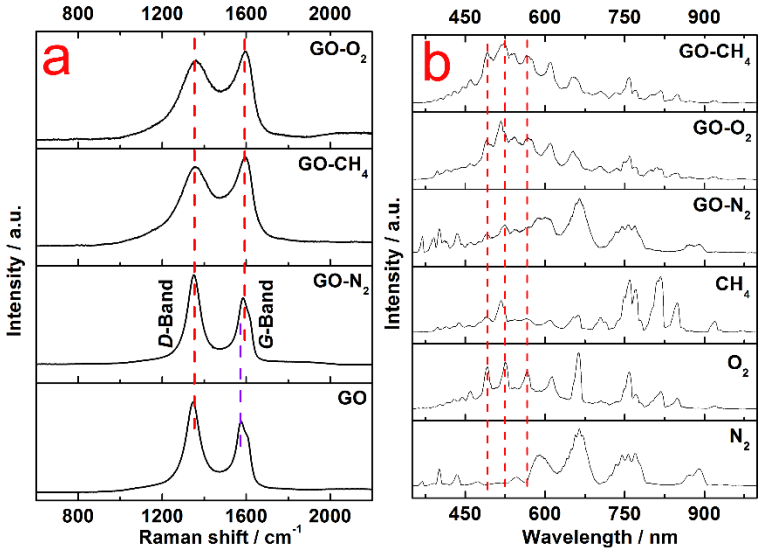

Fig. 54 Raman spectra (a) and OES spectra (b) of the background plasmas and at the explosion moment for GO-N_2, GO-CH_4 and GO-O_2.

Raman spectroscopy was used to investigate the ordered and disordered crystal structures of the fabricated samples due to its high sensitivity to the carbon electronic structures. As shown in Fig. 54, two featured peaks located at 1360 cm^{-1} and 1577 cm^{-1} were observed for all the samples, which were assigned to *D*-band and *G*-band, respectively. The *D*-

band and *G*-band were associated with disordered graphite structure or graphene edges, and the first-order scattering of the E_{2g} mode of sp^2 carbon domains, respectively. In addition, a blue-shift of *G*-band from 1577 cm^{-1} to 1596 cm^{-1} occurred for GO-N_2, GO-CH_4 and GO-O_2 in contrast to GO, which indicated a reduced number of graphene layers [204, 205]. In other words, the GO was transformed to graphene after the plasma treatment, which was consistent with the TEM observation.

To understand the mechanism of plasma exfoliation, the process was recorded by video Interestingly, no matter what kind of plasma gas was used, the plasma emission light turned into bright blue at the very moment of exfoliation, which was an indication of oxygen plasma. Enlighted by this phenomenon, it was speculated that oxygen was produced upon exfoliation. To verify this speculation, plasma emission spectra were recorded by OES to investigate the possible reactions during the exfoliation (Fig. 54b). In addition to recording the OES during the exfoliations, plasma emission spectra from the background gases were also recorded. It was found that there were three common peaks located at 491.8, 526.8 and 565.9 nm for samples of GO-N_2, GO-O_2 and GO-CH_4 and O_2 plasma after eliminating the background. These three peaks did not appear in the N_2 and CH_4 plasmas. These results clearly indicated that oxygen was produced during the exfoliation. Based on this result, the following mechanism was proposed. In the dielectric barrier discharge, GO samples were surrounded by plasma consisted of gas molecular, electrons and ions. Fast moving electrons would lead to negative self-bias of the GO samples. Ions were attracted by the negative potential to bombard the GO and broke the bonds between the oxygen and carbon. Meanwhile, the dissociated oxygen species combined to form oxygen molecules between the GO layers under the assistance of the

ion bombardment. When the RF power and gas pressure were increased to certain levels (e.g. 70 W and 3 Torr), the above reaction happened within a very short time and newly formed oxygen gas in between the graphitic layers drastically expanded, subsequently leading to the separation of the graphite layers.

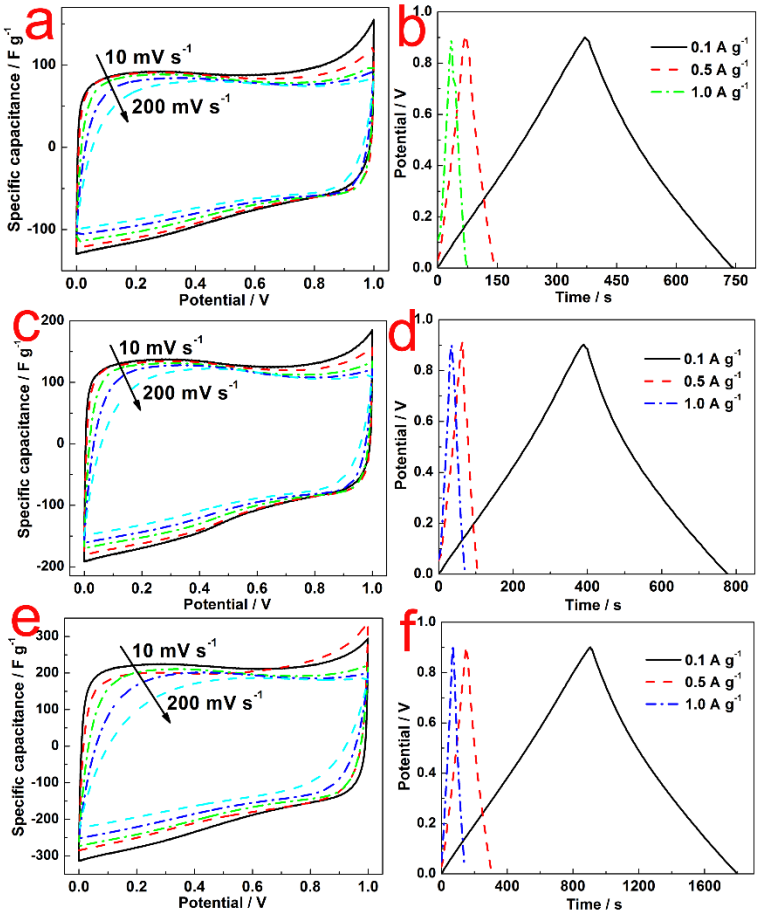

Fig. 55 CV curves of GO-N_2 (a), GO-CH_4 (c), and GO-O_2 (e) at different scanning rates ranging from 10 to 200 mV s^{-1}, and galvanostatic charge/discharge curves of GO-N_2 (b), GO-CH_4 (d), and GO-O_2 (f) at different current densities.

Fig. 55a, c and e showed the CV curves of GO-N_2, GO-CH_4 and GO-O_2 based electrodes at different scanning rate ranging from 10 to 200 mV s^{-1}, respectively. Typical quasi-

rectangular shapes were observed for all the electrodes at different scanning rate, indicating a representative capacitive behavior. The specific capacitance (*C*) of the electrode materials was calculated from the CV curves by the equation [189]:

$$C = 2\int IdV / vmV \quad (1)$$

where *C* is the specific capacitance, *I* is the response current; *V* is the potential; *v* is the potential scan rate; *m* is the mass of the electrode materials. The GO-CH_4 exhibited largest specific capacitance (215 F g^{-1} at 10 mV s^{-1}) compared with that of the GO-N_2 and GO-O_2 (88 and 129 F g^{-1} at 10 mV s^{-1}, respectively). Furthermore, the CV curve of the GO-CH_4 exhibited very small distortion, indicating very good rate capability. The capacitance performance obtained from this work was compared with the reported values of EDLCs that used graphene-based materials as electrodes (Table 4). The GO-CH_4 had comparable or better performance than those using the same electrolyte. The exact reasons accounting for the different capacitance caused by the CH_4, O_2, and N_2 plasmas were not clear. It was speculated that CH_4 plasma could have two effects acting at the same time, i.e. atomic hydrogen etching and carbon growth, which created defects in the produced graphene and/or led to new nanostructured carbon grown on the graphene/nanosheets. In addition, all the plasma-exfoliated samples exhibited triangular symmetric galvanostatic charge/discharge curves at different current densities (Fig.55 b, d and f), which indicated an excellent electrochemical reversibility.

Table 4 Comparison of specific capacitance of different graphene electrodes.

Electrode	Electrode	Specific	Current	Electrolyte	Reference

materials	system	capacitance	density		
Graphene	2	165 F g^{-1}	0.05 A g^{-1}	6 M KOH	[206]
Graphene	2	154.1 F g^{-1}	1 A g^{-1}	$EMIMBF_4$	[207]
RGO	2	138.1 F g^{-1}	1 A g^{-1}	1M Et_4NBF_4/ propylenecarbone	[208]
Activated Graphene	2	174 F g^{-1}	8.4 A g^{-1}	$[BMIM][BF_4]$/AN	[209]
C-NGNSs	2	245.9 F g^{-1}	1 A g^{-1}	1M $[Bu_4N]BF_4$	[210]
G-PNF_{30}	2	197 F g^{-1}	3 A g^{-1}	1 M H_2SO_4	[67]
GNSs	2	36.6 F g^{-1}	0.1A g^{-1}	2 M $EMIMBF_4$/acetonitrile	[211]
GNs	2	116 F g^{-1}	5 A g^{-1}	6 M KOH	[212]
GO-CH_4	2	192 F g^{-1}	1 A g^{-1}	6 M KOH	This work

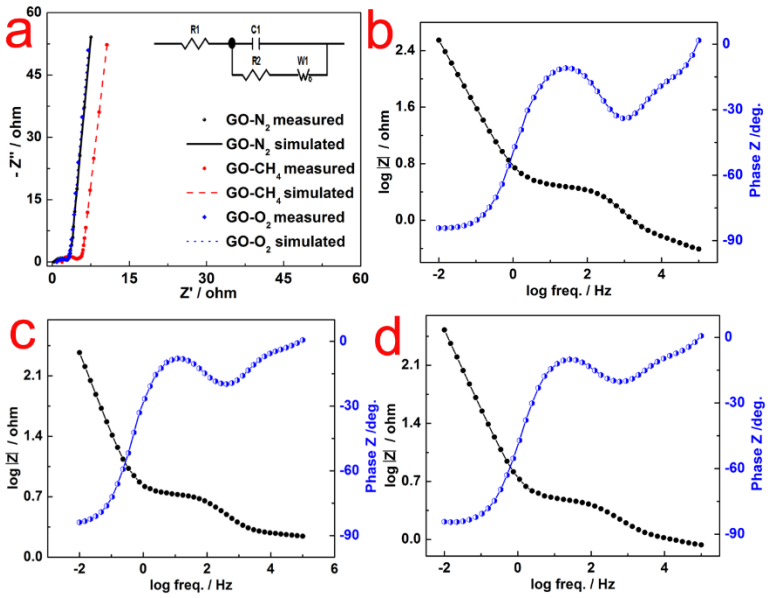

Fig. 56 Nyquist plots (a) and Bode plots of GO-N_2 (b), GO-CH_4 (c) and GO-O_2 (d). Inset in Fig. 56a is an equivalent electric circuit used for fitting the impedance spectra.

Fig. 56a showed Nyquist plots obtained from GO-N_2, GO-CH_4 and GO-O_2 electrodes in a frequency range of 0.01 Hz to 100 kHz and the equivalent circuit for fitting the EIS data obtained using ZView2 software. All the electrodes presented low resistance, which was 7.5, 8.9 and 7.2 **Ω** for GO-N_2, GO-CH_4 and GO-O_2 electrodes, respectively. The impedance consisted of an *x*-intercept in the high frequency region, a semicircle in the middle frequency region and a spike in the low frequency region, which corresponded to bulk electrolyte resistance (R_1), charge transfer resistance (R_2), and Warburg impedance (*W1*), respectively. [106, 134] Another distinct part C1 in the equivalent circuit stood for the double layer capacitance. Fig. 56b, c and d illustrated Bode phase angle plots of GO-N_2, GO-CH_4 and GO-O_2, respectively. Three slopes at different frequencies have been observed from the amplitude of the total impedance versus frequency plots. A sharp slope with phase shift ~84^o appeared in the low frequency range, which arose from the resistive components and stood for almost full double layer charge storage phenomenon and near absence of the faradic (redox) type charge storage phenomenon [213, 214]. A lower slope appeared in the mid-frequency range and was caused by capacitive components at the interfaces alone [213]. In the high frequency range, the small shift of the phase angle was controlled by the ionic resistance of the KOH electrolyte and both capacitive and resistive components of the electrode interfaces were displayed [213-215]. Notably, the lower slope of GO-CH_4 electrodes as compared with the other electrodes in the mid-frequency range indicated larger capacitive component and hence the electrode exhibited much better electrochemical performance with high specific capacitance.

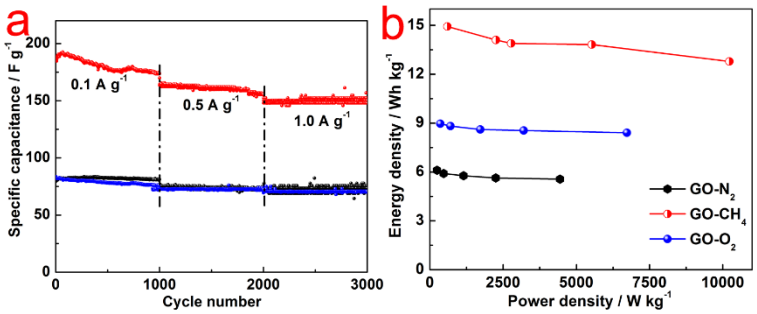

Fig. 57 Cycle life (a) at current densities from 0.1 to 1.0 A g^{-1} of GO-N_2, GO-CH_4 and GO-O_2 electrodes in 6 mol L^{-1} KOH and Ragone plots (b).

The cycle stability is also a crucial factor for supercapacitors application. Fig. 57a shows cycle life at current densities from 0.1 to 1.0 A g^{-1} of GO-N_2, GO-CH_4 and GO-O_2 electrodes in 6 mol L^{-1} KOH. As shown in Fig. 57b, comparable specific capacitance of ~80, 72, 70 F g^{-1} was obtained at current densities of 0.1, 0.5 and 1.0 A g^{-1} for GO-N_2 and GO-O_2 electrodes for each individual 1,000 cycles. GO-CH_4 electrode exhibited the largest specific capacitance of 192, 162, and 150 F g^{-1} at current densities of 0.1, 0.5 and 1.0 A g^{-1} for each individual 1000 cycles, respectively. Moreover, almost 100% retention was displayed though a little bit degradation appeared at current density of 0.1 A g^{-1}, indicating the good retention and excellent cycle stability of the GO-CH_4 electrodes.

To demonstrate the operational characteristics, the energy and power densities were calculated using the following equations [135]:

$$E = \frac{1}{2} C(\Delta V)^2 \tag{15}$$

$$P = \frac{E}{t} \tag{16}$$

where E is the average energy density (Wh kg^{-1}), C is the specific capacitance of the symmetric supercapacitor, ΔV is the voltage range, P is the average power density (W kg^{-1}) and t is the discharge time, respectively. Fig. 57b shows the Ragone plots of GO-N_2, GO-CH_4 and GO-O_2 based symmetric supercapacitors. The energy density of GO-CH_4 electrodes was delivered at 14.93 Wh kg^{-1} with a power density of 597.2 W kg^{-1}, The energy and power densities after the cycle-life tests remained at 12.8 Wh kg^{-1} and 10.2 kW kg^{-1}, which were much higher than the maximum values of GO-N_2 (6.11 Wh kg^{-1} and 244.4 W kg^{-1}) and GO-O_2 (8.96 Wh kg^{-1} and 358.4 W kg^{-1}). The superior performance of GO-CH_4 in energy and power densities made it a promising electrode material for EDLCs.

9.4 Conclusions

Graphene has been successfully prepared from graphite oxides using plasma exfoliation at room temperature. This method is time saving, energy efficient, and environmentally friendly. Oxygen was produced during the exfoliation process. Based on optical emission spectroscopy and microstructure analysis, the plasma exfoliation mechanism was revealed. The GO-CH_4 based electrodes for EDLCs displayed a specific capacitance as high as 215 F g^{-1}, together with excellent cycle stability and energy density. Plasma exfoliation is a promising method for manufacturing graphene, which has many potential applications such as supercapacitors.

Chapter 10 Low-temperature plasma exfoliated N-doped graphene for symmetrical electrode supercapacitors©

10.1 Introduction

Supercapacitors are electrical-energy-storage devices that have recently attracted considerable interest due to their long life cycle, fast charge/discharge capability, and high power [216-219]. Based on the working principles, supercapacitors can be classified into two major types: pseudocapacitors and electrical double layer capacitors (EDLCs). In pseudocapacitors, fast redox reactions, also known as faradic reactions, occur between the electrode and electrolyte during charge/discharge. Subsequently electrical energy is stored [220]. Thus, metal oxides (e.g. MnO_2, NiO, $Ni(OH)_2$, Co_3O_4 [146, 221-223]) are commonly used as the electrode materials to enable the redox reactions with the electrolyte. In contrast to pseudocapacitors, no chemical reaction is involved in EDLCs and carbon materials are commonly used for the electrodes. Energy storage in EDLCs is

achieved *via* adsorption and desorption of electrolyte ions. In this process, charge accumulation occurs due to electrostatic attraction between the positive and negative charges that separately reside at the electrode/electrolyte interface [224]. Pseduocapacitors have been demonstrated with very high capacitive performance. However, their capacity usually decreased sharply with increasing cycles, especially at high current densities. On the other hand, EDLCs possess superior stability under a wide range of current densities and excellent tolerance to a broad variety of electrolytes, due to the inherent stability of carbon materials. In the past few years, a variety of carbon materials (e.g. carbon nanotubes, carbon fibers, activated carbon and graphene [15, 209, 225, 226]) have been investigated as the electrodes for EDLCs. The desired characteristics for the carbon electrode materials include [227]: i) high specific surface area (SSA) to provide large accessible area to the electrolyte; ii) low resistance to minimize energy loss; iii) suitable pore size to allow fast transfer of electrolyte ions; and iv) sustainable and abundant to keep the cost low. These requirements have driven the research for various porous carbon and carbon nanomaterials for high-performance supercapacitors. Current challenges that limit the capacitive performance of porous-carbon-based electrodes include relatively low conductivity and structural degradation due to swelling and shrinkage during the charge/discharge process. Among the reported carbon materials, graphene has showed extraordinary potential for EDLCs [67, 228, 229].

Graphene is a two dimensional sp^2 hybridized carbon layer that has proven excellent properties including mechanical flexibility (high Young`s modulus 1.0 TPa) [230], exceptional thermal conductivity (5,000 W m^{-1} k^{-1}) [231], high electrical conductivity ($\sim 10^6$ S cm^{-2}) [232], high theoretical surface area (2,630 m^2 g^{-1} for single layer graphene)

[233], and high transmittance (97.7%) [234] to visible light. These unique physical and chemical properties make graphene promising for many applications, such as energy storage and conversion (supercapacitors, fuel cells, solar cells and Li-ion batteries) [207, 235-237], biomedical technologies (biosensors and drug carriers) [238, 239], and electronic components [240].

Many methods have been reported to fabricate graphene. In 2004, Geim and coworkers reported a scotch-tape method, in which graphene was prepared *via* mechanical exfoliation of graphite [241]. In 2006, planar carbon with a few layers of graphene was grown by chemical vapor deposition [242]. In 2007, epitaxial growth of graphene on SiC was reported [243]. In 2009, graphene was prepared *via* chemical exfoliation [244]. Of these methods, Hummers-method [245]-based chemical exfoliation was easier to implement than the others. In Hummers approach, concentrated sulfuric acid (H_2SO_4), sodium nitrite ($NaNO_3$) and potassium permanganate ($KMnO_4$) were used to exfoliate graphite flake to graphite oxides (GOs) and subsequently graphene was obtained *via* further chemical reduction and physical treatment.

The electrochemical properties of graphene could be modified by doping. Several groups have demonstrated N-doping that greatly promoted the specific capacitance of graphene. In 2011, *Choi* and *Yang* [69, 208] reported N-doped graphene prepared *via* plasma enhanced chemical vapor deposition and thermal nitridation, respectively. They prepared EDLCs using the N-doped graphene electrodes and obtained specific capacitance of 280 and 144.9 F g^{-1}. In 2012, specific capacitance of 245.9 F g^{-1} was reported by *Chen* [208] who used pyrolysis to prepare N-doped graphene. In 2013, *Chen* and *Yang* [77, 92] developed a solvothermal method to prepare N-doped graphene and achieved specific

capacitance of 301 F g^{-1}. In 2015, *Gomes* [246] reported a simple thermal treatment method to prepare N-doped graphene and attained a specific capacitance of 210 F g^{-1}. However, all the above processes required high temperatures and were time consuming.

The demands for graphene and N-doped graphene have driven the research on efficient fabrication of these carbon nanomaterials. In this work, the authors demonstrated an effective plasma exfoliation to prepare graphene, which was particularly suitable for high-performance supercapacitors. GOs prepared *via* modified-Hummers method were rapidly exfoliated into graphene or N-doped graphene at low temperatures using a radio frequency dielectric barrier discharge plasma. This study revealed the plasma exfoliation mechanisms by combining optical emission spectroscopy of the plasma discharge with materials microstructure analysis. The promising potential of the plasma exfoliated graphene for EDLCs was confirmed by a variety of electrochemical characterizations.

10.2 Material and methods

10.2.1 Preparation of graphite oxides

Graphite oxides were synthesized via modified Hummer`s method [245]. Typically, 2.5 g graphite (Fisher Scientific) was added into 100 ml concentrated sulfuric acid (98 *wt*%, Fisher Scientific) and kept stirring at 0 ℃ for 4 h. Afterwards 7.5 g potassium permanganate (Fisher Scientific) was slowly added into above solution before 2.5 g sodium nitrate (Fisher Scientific) being dissolved. The mixture was continuously stirred for 12 h and 50 ml distilled water was added into the solution drop by drop under a temperature of 98 ℃. Subsequently, 150 ml distilled water was added to further dilute the solution under stirring for 4 h. To reduce the residual permanganate and manganese dioxide to colorless soluble manganese sulfate, 15 ml hydrogen peroxide (30 *wt*%, Fisher

Scientific) was added. The prepared colloid was transferred into dialysis tubing (14,000 MWCO Daltons, Fisher Scientific) to dialyze in DI water for 2 days. Finally, the dialyzed sample was further separated by centrifugation at 8,000 rpm and washed with DI water till the pH was close to 7, and then dried at 60 ℃ in a vacuum oven for 24 h. The prepared graphite oxide was denoted in short for GO.

10.2.2 Preparation of N-modified graphite oxides

N-modified graphite oxide was prepared by immersing the synthesized GO (2 g) into 2 ml pyrrole for 48 h. During that period, the pyrrole spontaneously polymerized and became polypyrrole. The GO sample was subsequently covered with polypyrrole. The polypyrrole-modified graphite oxide was denoted as GO-PPY.

10.2.3 Preparation of graphene

A dielectric barrier discharge plasma system was used to prepare graphene from the GO and GO-PPY samples. The plasma system included a quartz tube that severed as the vacuum chamber, a mechanical vacuum pump, a 13.56 MHz RF power supply, a matching network, a vacuum gauge, and a gas flow controller. Firstly, 300 mg GO or GO-PPY was placed into the quartz tube. Then, the tube was evacuated with the vacuum pump and purged with the process gas (i.e. nitrogen, oxygen, or methane). This step was repeated three times to make sure the residual air in the tube was negligible. After that, the gas flow was adjusted to maintain a stable pressure of ~28 mTorr. Then the RF power was turned on and the matching network was tuned manually to achieve almost zero watt reflection power. The gas pressure was subsequently increased to 3 Torr and the RF power was gradually increased to 70 W, during which the graphite oxides exfoliated. After the exfoliation (please watch the supplemental video for the exfoliation process),

the RF power, gas flow, and vacuum valves were turned off in sequence and the quartz tube was vented to collect the exfoliated sample. Corresponding to the plasma gas, the prepared samples were named as GO-O_2, GO-N_2, and GO-CH_4.

10.2.4 Preparation of N-doped graphene

N-doped graphene was prepared following the same procedure of the GO samples, but the raw material was GO-PPY. Corresponding to the applied plasma gas, the prepared samples were denoted as GO-PPY-N_2, GO-PPY-O_2, and GO-PPY-CH_4.

10.2.5 Preparation of supercapacitor electrodes

The electrodes were prepared by mixing the graphene samples of GO-O_2, GO-N_2, GO-CH_4, GO-PPY-N_2, GO-PPY-O_2, or GO-PPY-CH_4 (80 *wt*%) with acetylene black (10 *wt*%) and PTFE (10 *wt*%), and then pressing onto a nickel foam (EQ-bcnf-16m, MTI Corp.) of 1 cm^2 surface area. The electrodes were dried at 60 ℃ for 12 hours in an oven. Afterwards, a sandwich structure was formed by placing two pieces of microporous PP separator celgard-3501 between two electrodes in a 2032 type coin cell. Finally, the cell was pressed under a pressure of 1,000 kg cm^{-2} to finish the assembly.

10.2.6 Physical characterization

X-ray photoelectron spectroscopy (XPS) was performed on an SSX-100 system (Surface Science Laboratories, Inc.) equipped with a monochromated Al K_α X-ray source. For high resolution data, the lowest binding energy C 1s peak was set at 285.0 eV and used as the reference for all of the other elements. Raman spectra were obtained on a Horiba LabRAM confocal Raman microscope system with excitation wavelength of 532 nm from a diode pumped solidstate laser. A transmission electron microscope (TEM) (JEM-2100 LaB6, JEOL) equipped with energy-dispersive X-ray spectroscopy (EDX) (Gatan

Inc.) was used to study the morphology, microstructure, and elemental mapping of the materials at an acceleration voltage of 200 kV. The plasma emission was monitored using an optical spectrometer (USB2000+, Ocean Optics, Inc. USA)

10.2.7 Electrochemical characterization

Cyclic voltammetry (CV) and electrochemical impedance spectroscopy (EIS) tests of the supercapacitors were performed on an electrochemical work station (SP-150, BioLogical, France) using 6 mol L^{-1} KOH electrolyte. The galvanostatic charge/discharge curves were obtained from a battery test system (BTS series, NEWARE, China).

10.3 Results and discussion

The XRD patterns of GO, GO-N_2, GO-O_2 and GO-CH_4 were recorded in Fig. 58. A featured peak located at ~10º was observed for the GO, which corresponded to the (001) planes of crystalline graphite. On the contrast, the peak at ~10º vanished after the plasma treatment and a broad peak at ~24º corresponding to graphitic (002) plane emerged for GO-N_2, GO-O_2 and GO-CH_4. These results indicated that the pristine GO was successfully exfoliated into disordered and loosely packed graphene [247, 248]. The exfoliation process was also recorded by video. As can be seen, the GO was exfoliated at RF power about 70 W and gas pressure ~3 Torr in a short time of a few seconds. In comparison with the tightly stacked GO hard flakes, the plasma treated samples (GO-N_2, GO-O_2 and GO-CH_4) became flocculent and soft particles with much larger volume.

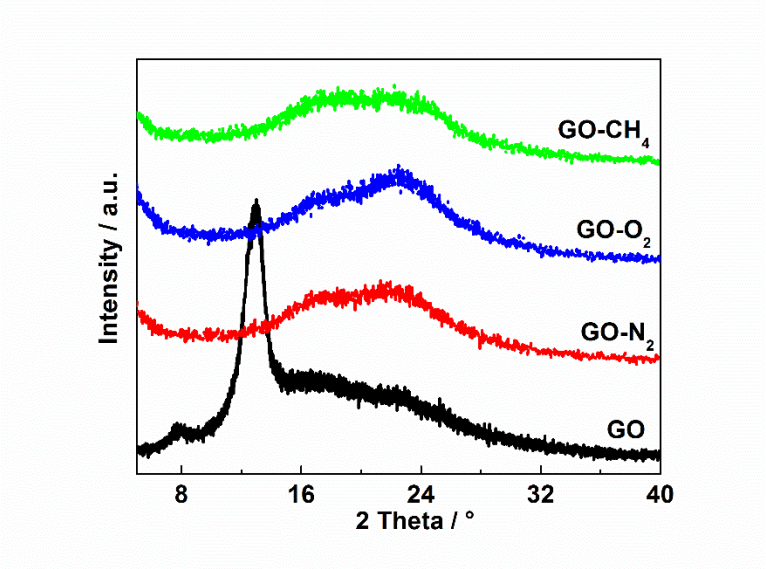

Fig. 58 XRD patterns of GO, GO-N_2, GO-O_2 and GO-CH_4.

Fig. 59 shows the Raman spectra of GO-N_2, GO-O_2 and GO-CH_4 in comparison with GO. Two distinct peaks of *D*-band and *G*-band located at 1350 cm^{-1} and 1580 cm^{-1}, respectively, were displayed. The *D*-band was associated with the A_{1g} mode breathing vibrations of six member sp^2 carbon rings, while the *G*-band was attributed to the first order scattering of the stretching vibration mode E_{2g} observed for the sp^2 carbon domain [135, 249]. Generally, the intensity ratio of *D*-band to *G* band (I_D/I_G) was used to estimate the disorder degree of graphene. The value of I_D/I_G was 1.24, 1.32, 0.92 and 0.91 for GO, GO-N_2, GO-O_2 and GO-CH_4, respectively. A I_D/I_G value larger than that of pristine GO implied that more defects were created after the nitrogen plasma treatment [135, 249]. The smaller I_D/I_G values for GO-O_2 and GO-CH_4 suggested the removal of oxygen-containing functional groups and partial restoration of the electronic conjugation in graphene sheets by repairing defects [135]. Such a difference most likely arose from the plasma gas during the exfoliation process.

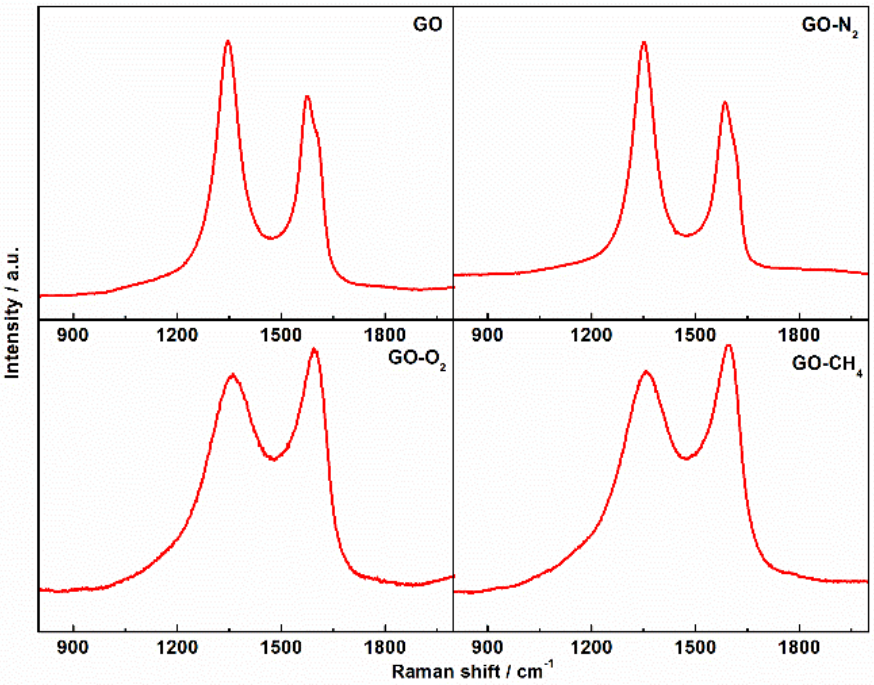

Fig. 59 Raman spectra of GO, GO-N_2, GO-O_2 and GO-CH_4.

To confirm the morphology and microstructure of the prepared samples, TEM was employed (Fig. 60). As displayed, the treated GO-N_2, GO-O_2 and GO-CH_4 samples exhibited ultrathin and flat graphene nanosheets, which were essential to provide beneficial SSA. The TEM results clearly indicated that the RF plasma successfully exfoliated the pristine GO into graphene nanosheets which was in consistence with the XRD analysis. In addition, element mapping (Fig. 61) showed carbon and oxygen uniformly dispersed in these samples.

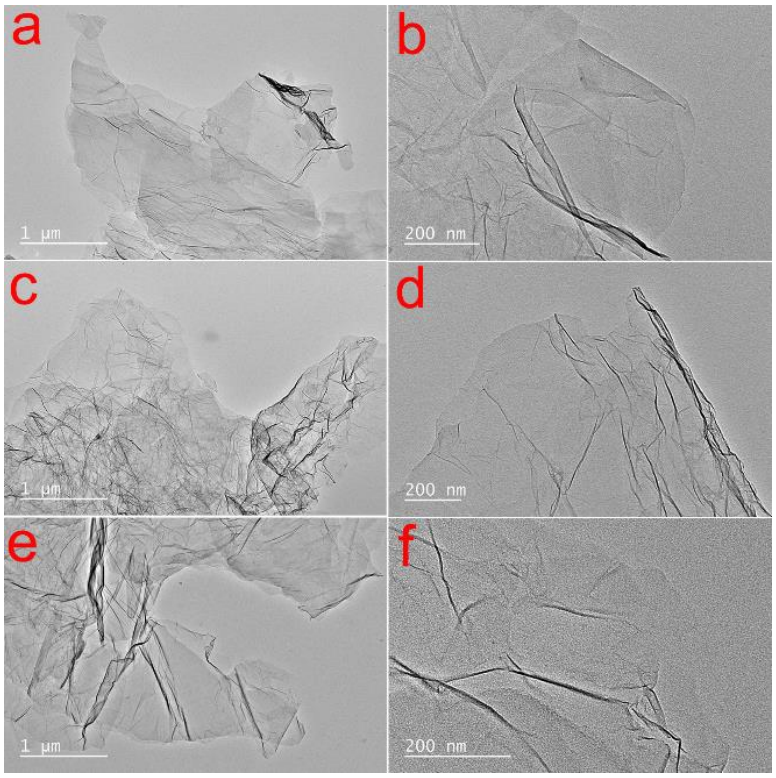

Fig. 60 Different magnifications TEM images of GO-N_2 (a, b), GO-O_2 (c, d) and GO-CH_4 (e, f).

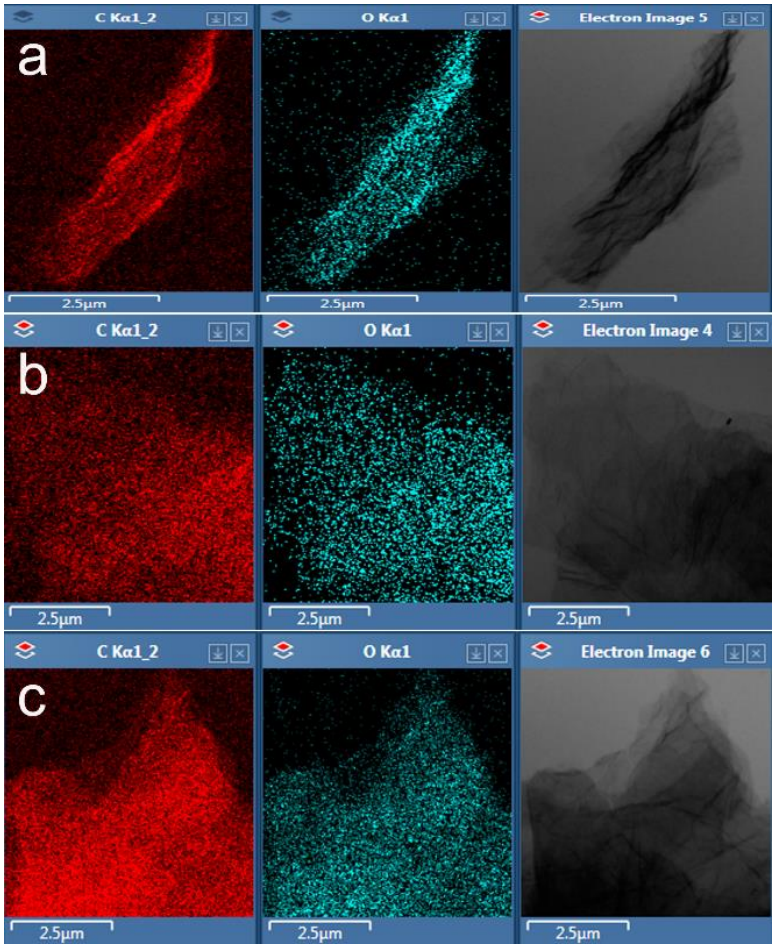

Fig. 61 Elemental mapping of GO- N_2, GO-O_2 and GO-CH_4.

To help understand the mechanism of the plasma exfoliation, the process was recorded by video (see Supplementary Information). Interestingly, no matter what kind of gas was used, the color of the plasma turned into bright blue at the very moment of explosion. The blue color was an indication of the presence of oxygen in the plasma. Inspired by this observation, the authors speculated that oxygen might be produced at the moment of explosion. To verify this speculation, optical emission spectra were recorded to study the reactions occurred during the exfoliation. The optical spectra are shown in Fig. 62, which includes the background spectra coming from the process gases (N_2, O_2, or CH_4). After eliminating the background spectra, it was found that there were three common peaks

located at 491.8, 526.8 and 565.9 nm, respectively, for all the three GO samples (GO-N_2, GO-O_2 and GO-CH_4) and O_2 plasma background. This result supported the speculation that oxygen was generated during the exfoliation. The suggested interactions between the plasma and the GO sample are as following. In the dielectric barrier discharge, the GO sample was electrically floating in the plasma. Electrons in the plasma moved faster than ions and led to negative self-bias of the GO samples. Ions attracted by the negative potential bombarded the GO and broke the bonds between the oxygen and carbon. Ion-GO interactions also led to localized rapid increase in the temperature of the GO as a result of kinetic energy transfer. Under the assistance of the ion bombardment, the dissociated oxygen species combined to form oxygen molecules between the GO layers. When the RF power and gas pressure were increased to certain levels (e.g. 70 W and 3 Torr), the thermal expansion of the oxygen gas formed inside the GO led to the separation of the graphite layers and exfoliation occurred. The plasma exfoliation was a swift process; it was completed in just a few seconds. Moreover, the exfoliation did not require external heating. After the process, the surface temperature of the quartz tube was low 80°C. Comparing with other methods used to prepare graphene (e.g. CVD, PECVD, thermal solvent), RF dielectric barrier discharge plasma was highly efficient.

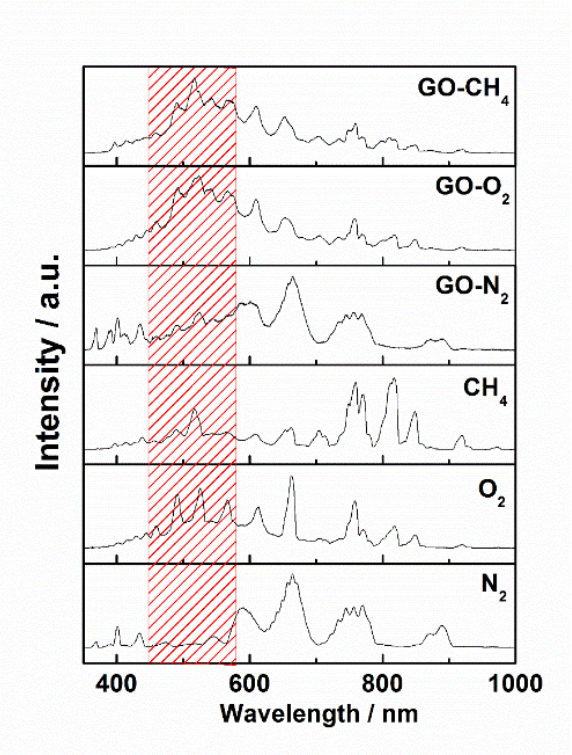

Fig. 62 OES observed at the explosion moment for GO-N_2, GO-O_2 and GO-CH_4, and the background.

The exfoliated GO was expected to have a porous structure with large surface area. Hence, EDLCs with symmetrical electrodes were prepared to evaluate the specific capacitance of the plasma exfoliated GO. The following equation [55] was used to calculated the specific capacitance:

$$C = \frac{2I\Delta t}{m\Delta v} \qquad (17)$$

where C is the specific capacitance, I is the charge/discharge current, Δt is the corresponding charge or discharge time, m is the mass of active materials on single electrode, and Δv is the total corresponding potential change.

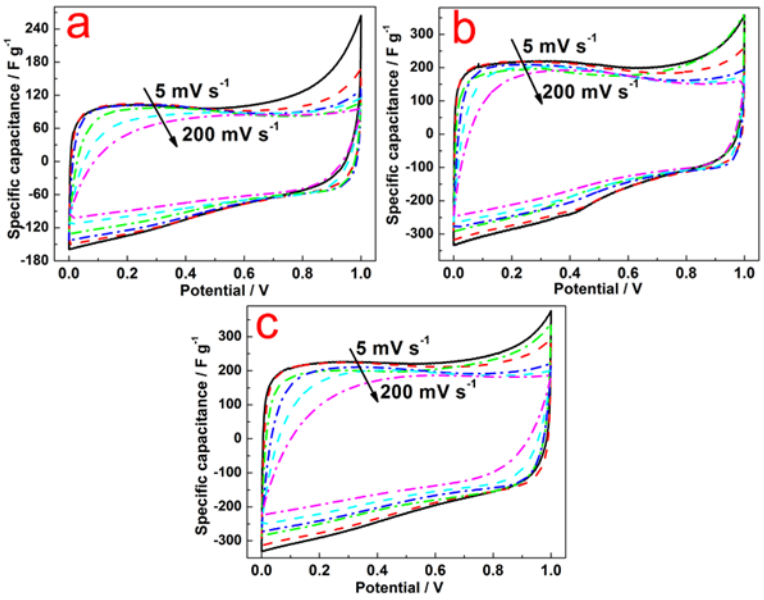

Fig. 63 CV curves of GO- N_2 (a), GO-O_2 (b) and GO-CH_4 (c) electrodes at various scanning rates ranging from 5 to 200 mV s^{-1} in 6 mol L^{-1} KOH.

Fig. 63a shows the CV curves of the electrodes prepared with GO-N_2, GO-O_2 and GO-CH_4 at a sweep potential window of 0 to 1 V at a scanning rate of 20 mV s^{-1}. All the three pairs of electrodes exhibited typical rectangular CV curves with only a little deformation for the GO-O_2 sample, indicating very good EDLCs behavior. At a scanning rate of 20 mV s^{-1}, the specific capacitance of GO-N_2, GO-O_2 and GO-CH_4 reached up to 93, 178 and 199 F g^{-1}, respectively, which indicated the potential of the materials for EDLC applications. In addition, the CV curves of GO-N_2, GO-O_2 and GO-CH_4 electrodes at different scanning rate ranging from 5 to 200 mV s^{-1} were recorded in Fig. 64. With the increase in the scanning rate, the specific capacitance gradually decreased and the shape distortion appeared for all these three electrodes. However, GO-CH_4 showed the least distortion. EIS measurements of the supercapacitors were conducted in the frequency range of 10 Hz to 100 kHz in order to evaluate resistance of the device (Fig. 63b). The

EIS consisted of an *x*-intercept at high frequency range, a semicircle in the middle frequency range, and a vertical line in the low frequency range, which corresponded to bulk electrolyte resistance, interfacial impedance between the electrode and bulk solution, and the impedance that was associated with intra-particle pores, respectively [105, 106]. The GO-O_2 sample presented the smallest resistance (6.6 Ω), while GO-N_2 (10.2 Ω) and GO-CH_4 (10.0 Ω) showed slightly higher resistance than the GO-O_2, but still small enough for high performance EDLCs electrode material.

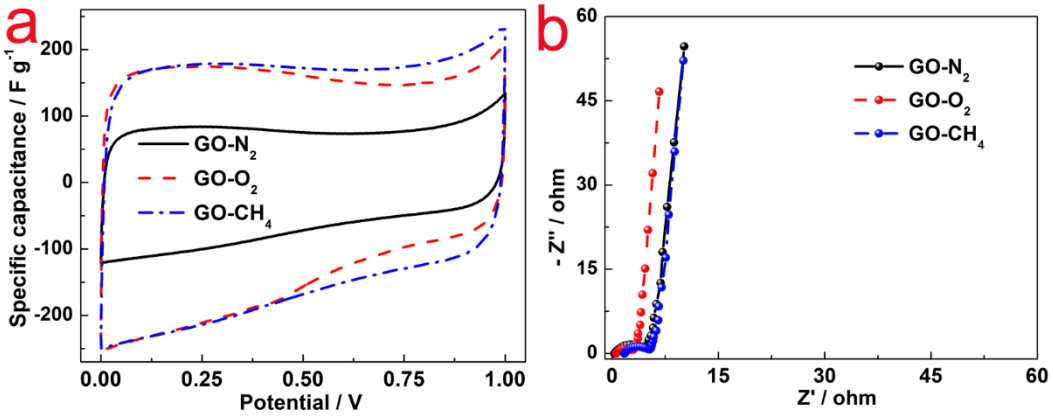

Fig. 63 CV curves (a) at scanning rate 20 mV s^{-1}, nyquist plots (b) of GO-N_2, GO-O_2 and GO-CH_4 electrodes in 6 mol L^{-1} KOH electrolyte.

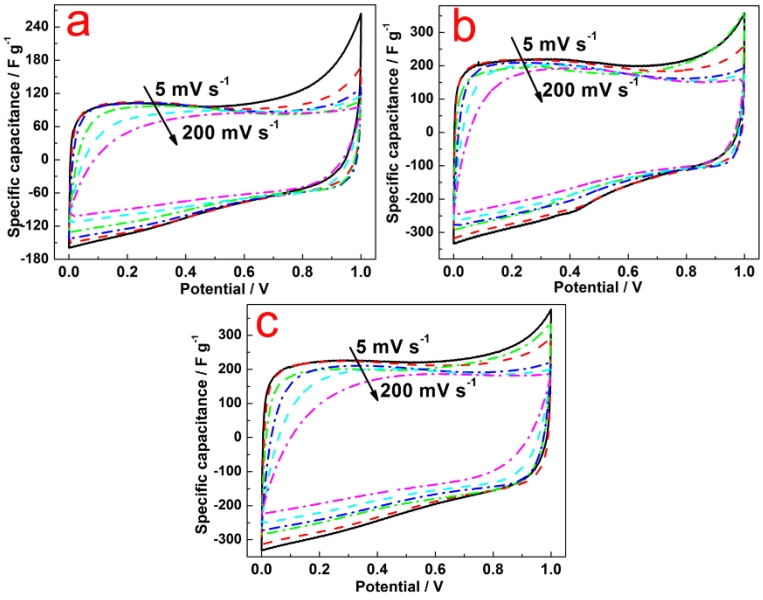

Fig. 64 CV curves of GO- N_2 (a), GO-O_2 (b) and GO-CH_4 (c) electrodes at various scanning rates ranging from 5 to 200 mV s^{-1} in 6 mol L^{-1} KOH.

The plasma exfoliated GO could be further modified to promote the specific capacitance. It was reported that introducing N could improve the capacitive performance *via* pseudocapacitance effect [124]. Therefore, N-modified GO (GO-PPY) was prepared and subsequently exfoliated by plasma.

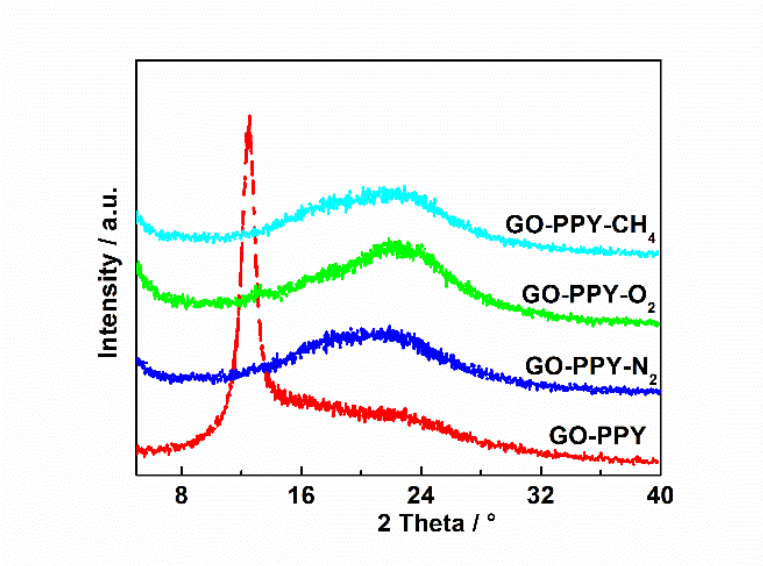

Fig. 65 XRD patterns of GO-PPY, GO-PPY-N_2, GO-PPY-O_2 and GO-PPY-CH_4.

Fig. 65 shows the XRD patterns of GO-PPY, GO-PPY-N_2, GO-PPY-O_2 and GO-PPY-CH_4. After the plasma treatment, the characteristic peak of GO located at ~10° (001) disappeared, but a broad peak around 24° (002) showed up, suggesting that the GOs were successfully exfoliated into graphene by the plasmas. Likewise, the same phenomenon as GO exfoliation was observed for GO-PPY with each of the plasma gases.

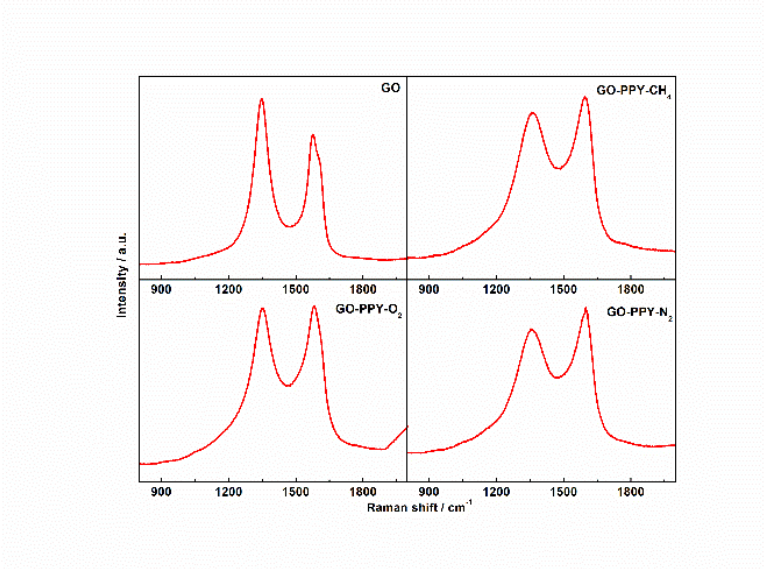

Fig. 66 Raman spectra of GO, GO-PPY-N_2, GO-PPY-O_2 and GO-PPY-CH_4.

Fig. 66 illustrated Raman spectra of GO, GO-PPY-N_2, GO-PPY-O_2 and GO-PPY-CH_4. Two distinct peaks of *D*-band and *G*-band located at 1350 cm^{-1} and 1580 cm^{-1}, respectively, were observed, which were related to A_{1g} mode breathing vibrations of six member sp^2 carbon rings, and the first order scattering of the stretching vibration mode E_{2g} of the sp^2 carbon domain [135, 249], respectively. The intensity ratio of *D*-band to *G* band (I_D/I_G) was also used to estimate the disorder degree of graphene. The value of I_D/I_G was 1.24, 0.92, 0.98 and 0.86 for GO, GO-PPY-N_2, GO-PPY-O_2 and GO-PPY-CH_4,

respectively, suggesting the removal of oxygen-containing functional groups and the partial restoration of the electronic conjugation in graphene sheets by repairing the defects [135].

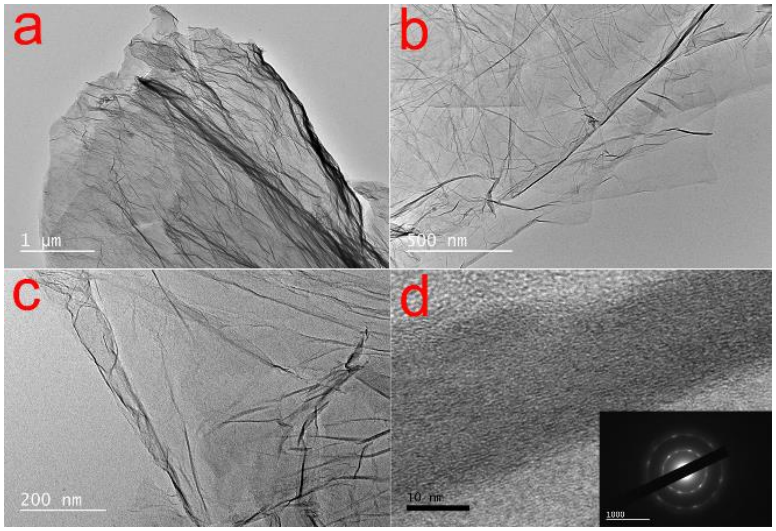

Fig. 67 TEM images of GO-PPY-CH_4 under different magnifications. The inset in (d) is SAED.

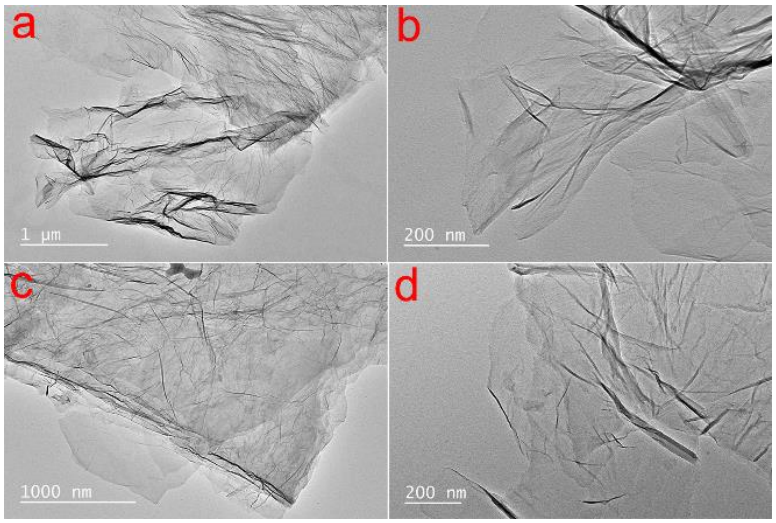

Fig. 68 TEM images of GO-PPY-N_2, GO-PPY-O_2 with different magnification.

To verify the microstructure of the prepared N-doped graphene, TEM was conducted (Fig. 67). As shown in Fig. 67 and Fig. 68, two-dimensional ultrathin graphene monolayer or multilayers were observed with some ripples. In addition, the existence of monolayer graphene for GO-PPY-CH_4 was further proved by SAED (the inset in Fig. 67d). A perfect hexagonal pattern was presented, which confirmed the well-crystallized single layer graphene structure [124, 250]. Elemental mapping (Fig. 69) was made to verify the nitrogen inclusion. The signals of carbon, oxygen and nitrogen were all detected and distributed uniformly, indicating nitrogen was successfully introduced. In other word, the N-doped graphene was expected to be a suitable material for high performance EDLCs.

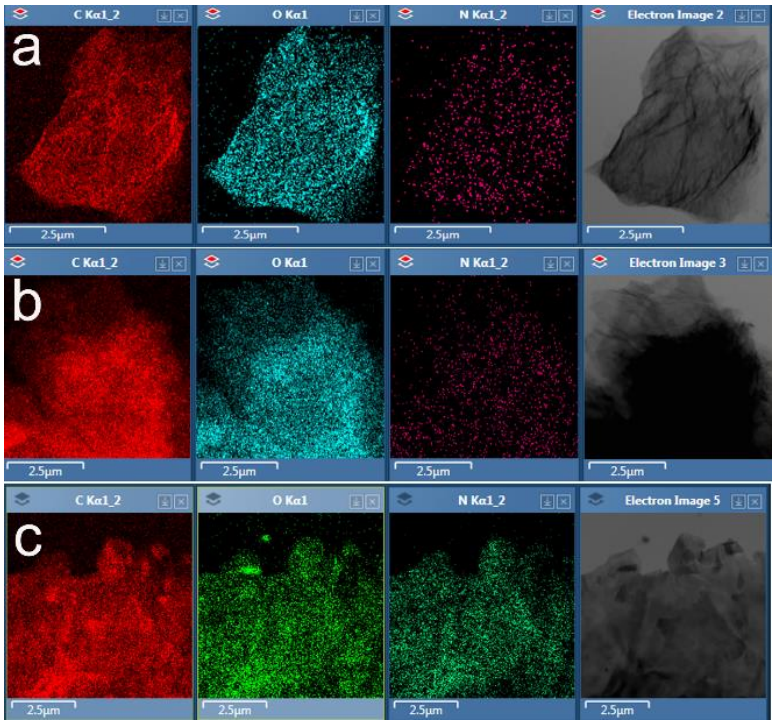

Fig. 69 Elemental mapping of GO-PPY-N_2 (a), GO-PPY-O_2 (b) and GO-PPY-CH_4 (c).

During the plasma exfoliation, OESs were recorded (Fig. 70). Interestingly, the same bright blue light appeared at the explosion moment for all the three gases. Besides, the

featured peaks of oxygen located at 491.8, 526.8 and 565.9 nm were also observed. All these results revealed that the exfoliation mechanisms were similar to that of GO, the only difference was that N was incorporated in the treated sample.

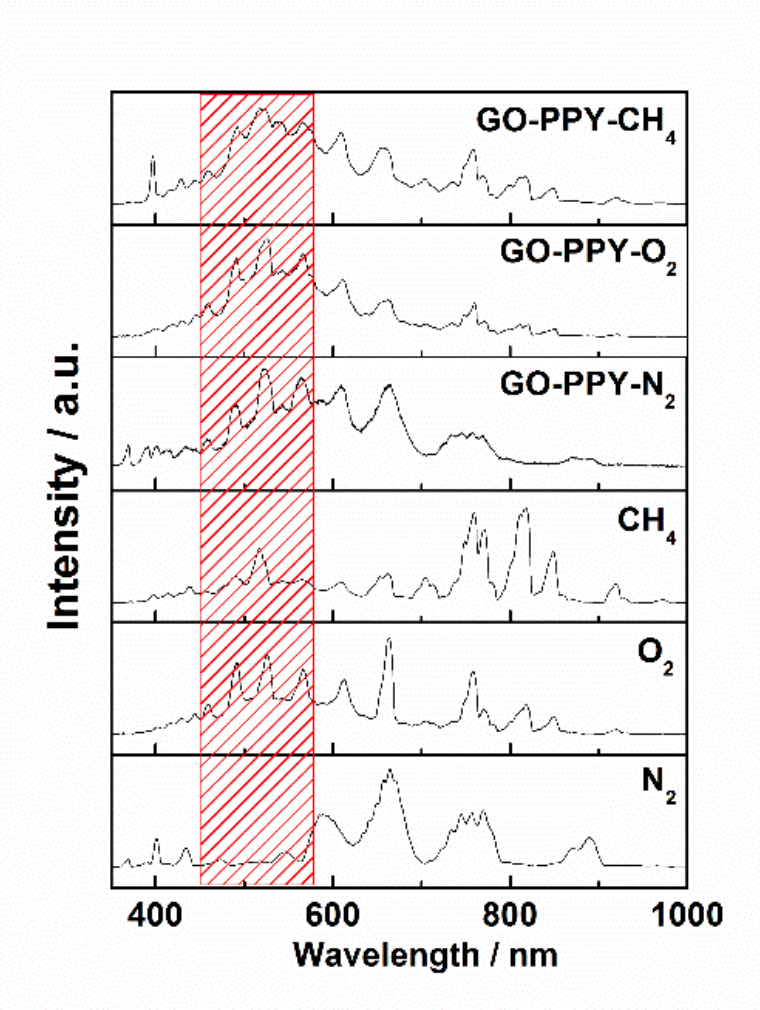

Fig. 70 OES observed at the explosion moment for GO-PPY-N_2, GO-PPY-O_2 and GO-PPY-CH_4, and the background.

XPS analysis was employed to analyze the functional groups in the surface of GO-PPY-N_2, GO-PPY-O_2 and GO-PPY-CH_4. In Fig. 71a, signals of C 1s (532 eV), O 1s (284 eV) and N 1s (400 eV) were detected, which indicated that N was successfully introduced

into the prepared graphene. The XPS analysis also verified the results of TEM elemental mapping. High resolution O 1s spectrum (Fig. 71b and Fig. 72a, c) was deconvoluted into three peaks at binding energy of ca. 531 eV, 532 eV, and 533.5 eV, which were assigned to O-I, O-II and O-III, respectively. The three O species represented C=O groups for O-I, C-OH groups and/or C-O-C groups for O-II, and O-C=O groups for O-III, respectively [157, 251]. Among them, O-I and O-II were the dominant functionalities that would contribute to the pseudocapacitance through the quinone/hydroquinone redox [251]. Besides, two peaks were detected at binding energy ca.398.9 and 401.0 eV for N species, which were attributed to pyridinic-N, and quaternary-N, respectively (Fig. 71c and Fig. 72b, d) [158, 159]. The significance of introducing N was that pyridinic-N could lead to great pseudocapacitance effect and improve the conductivity, resulting in enhanced capacitive performance. In addition, atomic element concentrations in the prepared GO-PPY, GO-PPY-N_2, GO-PPY-O_2 and GO-PPY-CH_4 were summarized in Table 5. It was noted that GO-PPY possessed the highest atomic content of nitrogen (10.9%), which was reasonable due to the incorporation of polypyrrole before the plasma treatment. After exfoliation, 8.9%, 1.1% and 4.2% N was detected in GO-PPY-N_2, GO-PPY-O_2 and GO-PPY-CH_4, respectively. This result indicated that N was partially removed due to the interactions between the plasma species and polypyrrole. Oxygen was most effective in removing polypyrrole. Further studied are underway to reveal the chemical interactions between the plasma species and GO-PPY.

Table. 5 Atomic elements content of prepared GO-PPY, GO-PPY-N_2, GO-PPY-O_2 and GO-PPY-CH_4.

	Carbon (Atomic %)	Oxygen (Atomic %)	Nitrogen (Atomic %)
GO-PPY	73.3	15.7	10.9

GO-PPY-N_2	73.8	17.4	8.9
GO-PPY-O_2	86.7	12.2	1.1
GO-PPY-CH_4	81.4	14.5	4.2

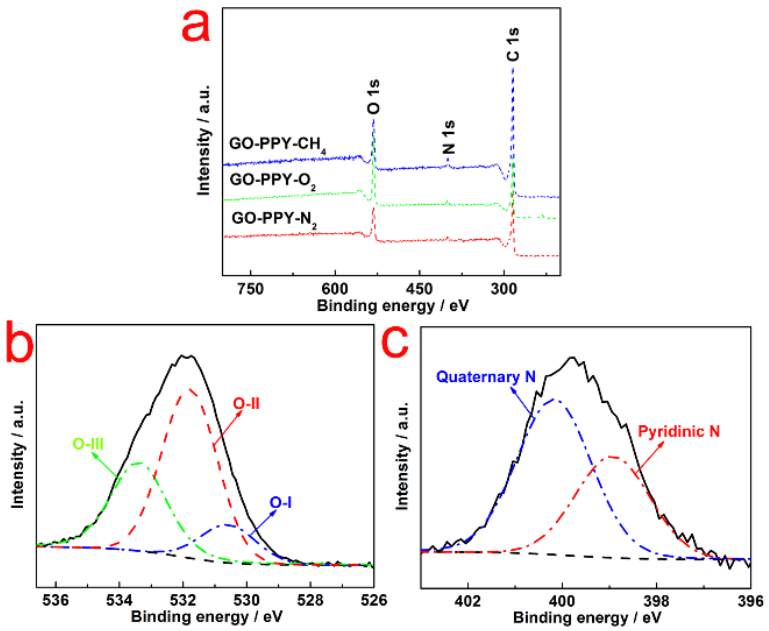

Fig. 71 XPS survey (a) of GO-PPY-N_2, GO-PPY-O_2 and GO-PPY-CH_4 and high resolution O 1s (b) and N 1s (c) XPS spectra of GO-PPY-CH_4.

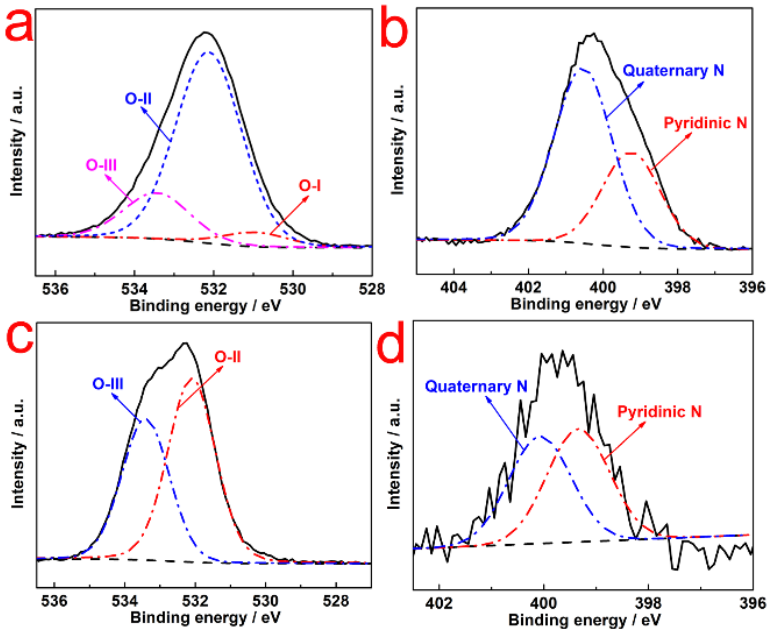

Fig. 72 High resolution O 1s and N 1s XPS spectra of GO-PPY-N_2 (a, b), GO-PPY-O_2 (c, d).

EDLCs were prepared with the exfoliated N-doped graphene as the electrode materials. CV tests were conducted to evaluate the electrochemical performance. Fig.73a shows the CV curves of GO-PPY-N_2, GO-PPY-O_2 and GO-PPY-CH_4 electrodes in 6 mol L^{-1} KOH electrolyte at a scanning rate of 20 mV s^{-1}. All three cells exhibited characteristic rectangular shape CV curves, which were an indication of very good electrochemical EDLC behavior. The specific capacitance was calculated according to formula (1) to quantify the EDLCs' performance. The specific capacitance reached up to 130, 178 and 250 F g^{-1} for GO-PPY-N_2, GO-PPY-O_2 and GO-PPY-CH_4, respectively. Although GO-PPY-N_2 contained the highest concentration of N from the XPS analysis, it produced the lowest specific capacitance. This result implied that only certain type of nitrogen doping, *i.e.* pyridinic-N, was effective in promoting the capacitive performance. CH_4 plasma promoted the incorporation of effective N in GO and/or created additional surface structures and functional groups that beneficial the capacitive performance. In addition, the better capacitance performance of GO-PPY-CH_4 may be arisen from two distinct effects of CH_4 plasma: i) hydrogen plasma etching of the graphite oxides, and ii) growth of nanostructured carbon on the produced graphene. These effects created defects and active surface that promoted the capacitance performance.

The impedance spectra were measured over a frequency range from 100 mHz to 10 kHz (Fig. 73b). From the inset, a short *x*-intercept, small diameter of the semicircle, and high slope at low frequency revealed that the GO-PPY-CH_4 electrodes had small bulk electrolyte resistance, interfacial impedance and the inter-particle ionic impedance. A smaller resistance meant higher conductivity and less energy loss, as well as good performance of EDLCs.

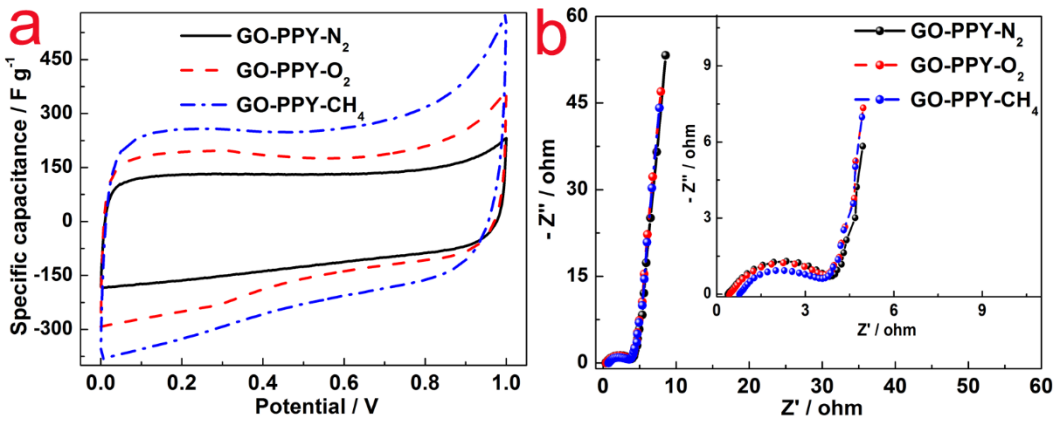

Fig. 73 CV curves (a) at scanning rate 20 mV s^{-1}, nyquist plots (b) of GO-PPY-N_2, GO-PPY-O_2 and GO-PPY-CH_4 electrodes in 6 mol L^{-1} KOH electrolyte; The inset in (b) shows the magnified view of the high-frequency region.

The specific capacitance was also recorded at different scanning rate ranging from 5 to 200 mV s^{-1} in CV test for all three samples (Fig. 74a and Fig. 75). GO-PPY-CH_4 showed much higher specific capacitance and rate capability with negligible distortion in comparison with that of GO-PPY-N_2 and GO-PPY-O_2.

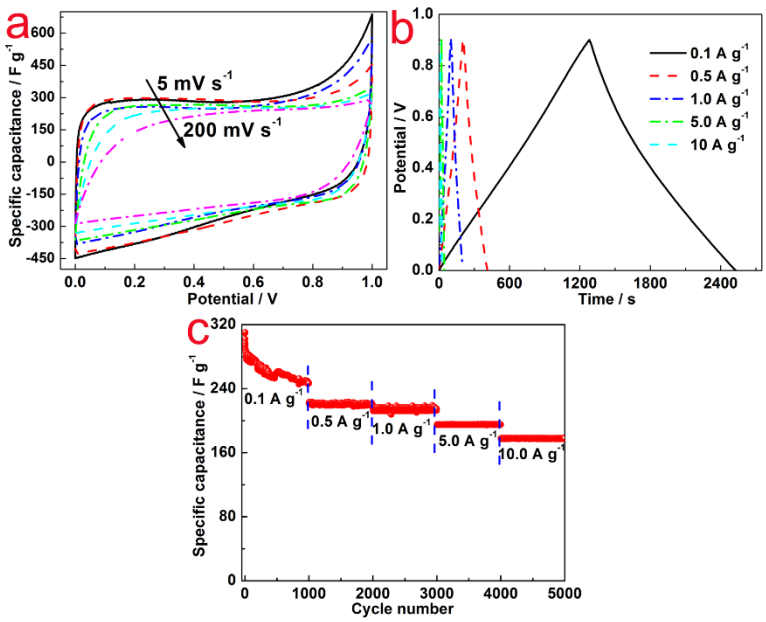

Fig. 74 CV curves (a) at various scanning rates ranging from 5 to 200 mV s^{-1}, galvanostatic charge/discharge curves (b) and cycle life plot (c) at different current density ranging from 0.1 to 10 A g^{-1} for GO-PPY-CH_4 electrodes in 6 mol L^{-1} KOH electrolyte, respectively.

Meanwhile, as another important index for EDLCs, stability or cycle life of GO-PPY-CH_4 was assessed by charge/discharge at various current densities. In galvanostatic charge/discharge measurement (Fig. 74b), symmetric lines without IR_{drop} indicated a good capacitive behavior of EDLCs, which was consistent with the result of CV measurement. The cycling performance of GO-PPY-CH_4 electrode was also evaluated using the galvanostatic charge/discharge shown in Fig. 74c. The measurement yielded a specific capacitance as high as 312 F g^{-1} at beginning and ended at 250 F g^{-1} under 0.1 A g^{-1} charge/discharge current with little fluctuation. The specific capacitance remained at 220, 215, 196, 178 F g^{-1} with a retention of almost 100% after 1000 consecutive cycles under larger currents of 0.5, 1.0, 5.0 and 10.0 A g^{-1}, respectively. The results indicated that the electrodes were highly reversible during charge/discharge processes.

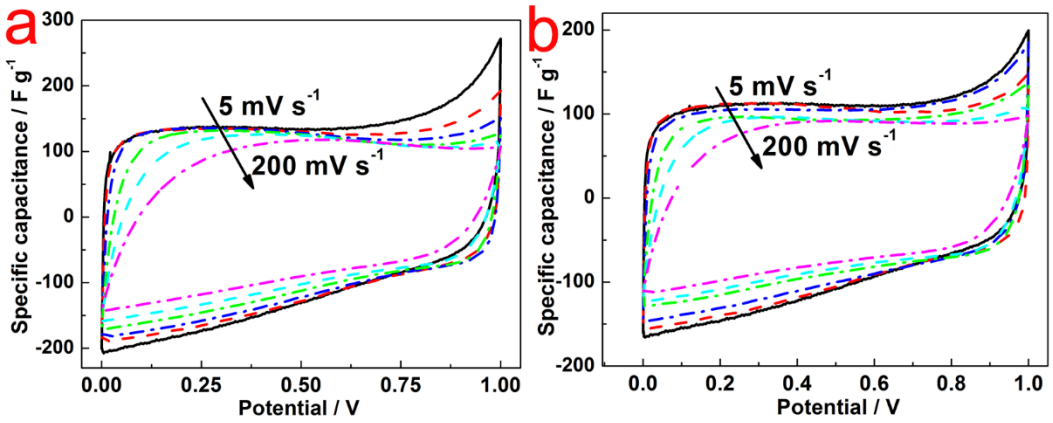

Fig. 75 CV curves of GO-PPY-N_2 (a) and GO-PPY-O_2 (b) electrodes at various scanning rates ranging from 5 to 200 mV s^{-1} in 6 mol L^{-1} KOH.

10.4 Conclusions

Graphite oxides were successfully exfoliated into graphene and N-doped graphene using radio-frequency dielectric barrier discharge plasma. The plasma exfoliation required a certain power level and pressure to transfer sufficient energy. Optical emission spectroscopy revealed the mechanisms of plasma exfoliation, which was due to the breakage of the C-O bonds and combination of O atoms into molecules that expanded under plasma. Comparing with oxygen and nitrogen plasmas, CH_4 plasma exfoliated N-doped graphene exhibited better capacitive characteristics, including high specific capacitance ~312 F g^{-1} and stable charge/discharge performance. The RF plasma exfoliation was a low-temperature and efficient approach to manufacturing graphene.

CONCLUSIONS

Carbon materials including AC/N-doped AC and graphene/N-doped graphene, have been prepared and successfully used as electrodes materials for symmetric supercapacitors. Of them, AC/N-doped AC derived from biomass/N-containing chemicals modified biomass (*e. g.* whey protein, cyanobacteria, fungus and lignin) has been prepared *via* efficient KOH activation method under pyrolysis and graphene/N-doped graphene was exfoliated by newly designed plasma system. Porous structure with high SSA and typical graphene morphology were displayed for prepared AC/N-doped AC and graphene/N-doped graphene in physical characterizations, respectively. Upon preparing into electrodes for EDLCs, excellent specific capacitance ranging from 215 to 333 F g^{-1}, low resistance (< 10 Ω) and high power and energy density have been obtained for prepared carbon

materials based electrodes in assembled EDLCs. KOH activation method worked efficiently in AC derived from biomass which was a mature routine to produce AC from biomass. Meanwhile, plasma exfoliation was creative and promising in graphene synthesis, which provided a new prospective for researchers focused on graphene preparation and application.

REFERENCES

[1] https://www.eia.gov/outlooks/ieo/world.cfm.

[2] S. Peng, L. Li, H.B. Wu, S. Madhavi, X.W.D. Lou, Adv. Energy Mater., 5 (2015) 1-7.

[3] R.R. Salunkhe, Y.H. Lee, K.H. Chang, J.M. Li, P. Simon, J. Tang, N.L. Torad, C.C. Hu, Y. Yamauchi, Chem. Eur. J., 20 (2014) 13838-13852.

[4] T.Y. Wei, C.H. Chen, H.C. Chien, S.Y. Lu, C.C. Hu, Adv. Mater., 22 (2010) 347-351.

[5] B.P. Bastakoti, H. Oveisi, C.C. Hu, K.C.W. Wu, N. Suzuki, K. Takai, Y. Kamachi, M. Imura, Y. Yamauchi, Eur. J. Inorg. Chem., 2013 (2013) 1109-1112.

[6] L. Kang, L. Zhang, H. Zou, Z. Deng, Y. Zhang, L. Chen, J. Alloy. Compd., 648 (2015) 190-194.

[7] Y. Ye, H. Zhang, Y. Chen, P. Deng, Z. Huang, L. Liu, Y. Qian, Y. Li, Q. Li, J. Alloy. Compd., 639 (2015) 422-427.

[8] B.E. Conway, Electrochemical supercapacitors: scientific fundamentals and technological applications, Springer Science & Business Media, 2013.

[9] M. Acerce, D. Voiry, M. Chhowalla, Nature Nanotechnol., 10 (2015) 313-318.

[10] J. Ji, L.L. Zhang, H. Ji, Y. Li, X. Zhao, X. Bai, X. Fan, F. Zhang, R.S. Ruoff, ACS Nano, 7 (2013) 6237-6243.

[11] R. Rakhi, W. Chen, M.N. Hedhili, D. Cha, H.N. Alshareef, ACS Appl. Mater. Inter., 6 (2014) 4196-4206.

[12] P. Yang, Y. Ding, Z. Lin, Z. Chen, Y. Li, P. Qiang, M. Ebrahimi, W. Mai, C.P. Wong, Z.L. Wang, Nano Lett., 14 (2014) 731-736.

[13] M.F. El-Kady, R.B. Kaner, Nature Commun., 4 (2013) 1475.

[14] K. Wang, Q. Meng, Y. Zhang, Z. Wei, M. Miao, Adv. Mater., 25 (2013) 1494-1498.

[15] K. Jost, D. Stenger, C.R. Perez, J.K. McDonough, K. Lian, Y. Gogotsi, G. Dion, Energ. Environ. Sci., 6 (2013) 2698-2705.

[16] C. Zheng, X. Zhou, H. Cao, G. Wang, Z. Liu, J. Power Sources, 258 (2014) 290-296.

[17] L. Qie, W.M. Chen, Z.H. Wang, Q.G. Shao, X. Li, L.X. Yuan, X.L. Hu, W.X. Zhang, Y.H. Huang, Adv. Mater., 24 (2012) 2047-2050.

[18] Y. Chen, X. Li, K. Park, J. Song, J. Hong, L. Zhou, Y.-W. Mai, H. Huang, J.B. Goodenough, J. Am. Chem. Soc., 135 (2013) 16280-16283.

[19] L. Qie, W. Chen, H. Xu, X. Xiong, Y. Jiang, F. Zou, X. Hu, Y. Xin, Z. Zhang, Y. Huang, Energ. Environ. Sci. 6 (2013) 2497-2504.

[20] C. Hu, L. Wang, Y. Zhao, M. Ye, Q. Chen, Z. Feng, L. Qu, Nanoscale, 6 (2014) 8002-8009.

[21] Y.S. Yun, S.Y. Cho, J. Shim, B.H. Kim, S.J. Chang, S.J. Baek, Y.S. Huh, Y. Tak, Y.W. Park, S. Park, Adv. Mater., 25 (2013) 1993-1998.

[22] Y. Fang, Y. Lv, R. Che, H. Wu, X. Zhang, D. Gu, G. Zheng, D. Zhao, J. Am. Chem. Soc., 135 (2013) 1524-1530.

[23] Y. Li, Z. Li, P.K. Shen, Adv. Mater., 25 (2013) 2474-2480.

[24] Y. Liang, D. Wu, R. Fu, Sci. Rep., 3 (2013) 1-5.

[25] Y. Li, W. Zhou, H. Wang, L. Xie, Y. Liang, F. Wei, J.-C. Idrobo, S.J. Pennycook, H. Dai, Nature Nanotechnol., 7 (2012) 394-400.

[26] L. Yang, S. Jiang, Y. Zhao, L. Zhu, S. Chen, X. Wang, Q. Wu, J. Ma, Y. Ma, Z. Hu, Angew. Chem., 123 (2011) 7270-7273.

[27] W.H. Shin, H.M. Jeong, B.G. Kim, J.K. Kang, J.W. Choi, Nano Lett., 12 (2012) 2283-2288.

[28] Z.-S. Wu, W. Ren, L. Xu, F. Li, H.-M. Cheng, ACS Nano, 5 (2011) 5463-5471.

[29] O. Ioannidou, A. Zabaniotou, Renew. Sust. Energ. Rev., 11 (2007) 1966-2005.

[30] W. Qian, F. Sun, Y. Xu, L. Qiu, C. Liu, S. Wang, F. Yan, Energ. Environ. Sci., 7 (2014) 379-386.

[31] Y. Gao, L. Li, Y. Jin, Y. Wang, C. Yuan, Y. Wei, G. Chen, J. Ge, H. Lu, Appl. Energ., 153 (2015) 41-47.

[32] Y. Zhang, Z. Gao, N. Song, X. Li, Electrochim. Acta, 222 (2016) 1257-1266.

[33] W. Tian, Q. Gao, Y. Tan, K. Yang, L. Zhu, C. Yang, H. Zhang, J. Mater. Chem. A, 3 (2015) 5656-5664.

[34] D. Jiménez-Cordero, F. Heras, M.A. Gilarranz, E. Raymundo-Piñero, Carbon, 71 (2014) 127-138.

[35] K.S. Novoselov, A.K. Geim, S.V. Morozov, D. Jiang, Y. Zhang, S.V. Dubonos, I.V. Grigorieva, A.A. Firsov, Science, 306 (2004) 666-669.

[36] K.S. Novoselov, V. Fal, L. Colombo, P. Gellert, M. Schwab, K. Kim, Nature, 490 (2012) 192-200.

[37] Q. Li, R. Jiang, Y. Dou, Z. Wu, T. Huang, D. Feng, J. Yang, A. Yu, D. Zhao, Carbon, 49 (2011) 1248-1257.

[38] L. Basirico, G. Lanzara, Nanotechnol.y, 23 (2012) 305401.

[39] P. Kossyrev, J. Power Sources, 201 (2012) 347-352.

[40] Y. Zhai, Y. Dou, D. Zhao, P.F. Fulvio, R.T. Mayes, S. Dai, Adv. Mate., 23 (2011) 4828-4850.

[41] M. Chen, X. Kang, T. Wumaier, J. Dou, B. Gao, Y. Han, G. Xu, Z. Liu, L. Zhang, J. Solid State Electrochem., 17 (2013) 1005-1012.

[42] X. He, R. Li, J. Han, M. Yu, M. Wu, Mater. Lett., 94 (2013) 158-160.

[43] X. Hong, K. Hui, Z. Zeng, K. Hui, L. Zhang, M. Mo, M. Li, Electrochim. Acta, 130 (2014) 464-469.

[44] M. Mladenov, K. Alexandrova, N.V. Petrov, B. Tsyntsarski, D. Kovacheva, N. Saliyski, R. Raicheff, J. Solid State Electrochem., 17 (2013) 2101-2108.

[45] C. Peng, X.-b. Yan, R.-t. Wang, J.-w. Lang, Y.-j. Ou, Q.-j. Xue, Electrochim. Acta, 87 (2013) 401-408.

[46] T.E. Rufford, D. Hulicova-Jurcakova, Z. Zhu, G.Q. Lu, Electrochem. Commun., 10 (2008) 1594-1597.

[47] D.J. Barrington, A. Ghadouani, Environ. Sci. Technol., 42 (2008) 8916-8921.

[48] Y. Li, M. Horsman, N. Wu, C.Q. Lan, N. Dubois‐Calero, Biotechnol. Prog., 24 (2008) 815-820.

[49] D.E. Robertson, S.A. Jacobson, F. Morgan, D. Berry, G.M. Church, N.B. Afeyan, Photosynthe. Res., 107 (2011) 269-277.

[50] L.C. González, F.F. Acién, S.J. Fernández, F.J. Sánchez, G.M. Cerón, G.E. Molina, Bioresour. Technol., 100 (2009) 5904-5910.

[51] H. Qiang, A. Richmond, J. Appl. Phyc., 8 (1996) 139-145.

[52] F. Sarsekeyeva, B.K. Zayadan, A. Usserbaeva, V.S. Bedbenov, M.A. Sinetova, D.A. Los, Photosynth. Res., (2015) 1-12.

[53] E. Raymundo‐Piñero, M. Cadek, F. Beguin, Adv. Fun. Mater., 19 (2009) 1032-1039.

[54] M. Sevilla, W. Gu, C. Falco, M. Titirici, A. Fuertes, G. Yushin, J. Power Sources, 267 (2014) 26-32.

[55] M. Wahid, G. Parte, D. Phase, S. Ogale, J.Mater. Chem. A, 3 (2015) 1208-1215.

[56] X. Ning, W. Zhong, S. Li, Y. Wang, W. Yang, J. Mater. Chem. A, 2 (2014) 8859-8867.

[57] J. Qi, L. Jiang, S. Wang, G. Sun, Appl. Catal. B: Environ., 107 (2011) 95-103.

[58] C. Moreno-Castilla, M. Lopez-Ramon, F. Carrasco-Marın, Carbon, 38 (2000) 1995-2001.

[59] J.D. Ding, Y.F. Diao, H.G. Shen, Adv. Mater. Res., 156 (2011) 1211-1214.

[60] J. Romanos, M. Beckner, T. Rash, L. Firlej, B. Kuchta, P. Yu, G. Suppes, C. Wexler, P. Pfeifer, Nanotechnol., 23 (2012) 015401.

[61] W. Fan, Y.-Y. Xia, W.W. Tjiu, P.K. Pallathadka, C. He, T. Liu, J. Power Sources, 243 (2013) 973-981.

[62] J. Wei, D. Zhou, Z. Sun, Y. Deng, Y. Xia, D. Zhao, Adv. Fun. Mater., 23 (2013) 2322-2328.

[63] J. Han, G. Xu, B. Ding, J. Pan, H. Dou, D.R. MacFarlane, J. Mater. Chem. A, 2 (2014) 5352-5357.

[64] B. Xu, D. Zheng, M. Jia, G. Cao, Y. Yang, Electrochim. Acta, 98 (2013) 176-182.

[65] N. Xiao, D. Lau, W. Shi, J. Zhu, X. Dong, H.H. Hng, Q. Yan, Carbon, 57 (2013) 184-190.

[66] L.-F. Chen, X.-D. Zhang, H.-W. Liang, M. Kong, Q.-F. Guan, P. Chen, Z.-Y. Wu, S.-H. Yu, ACS Nano, 6 (2012) 7092-7102.

[67] Q. Wu, Y. Xu, Z. Yao, A. Liu, G. Shi, ACS Nano, 4 (2010) 1963-1970.

[68] H.D. Yoo, J.H. Jang, J.H. Ryu, Y. Park, S.M. Oh, J. Power Sources, 267 (2014) 411-420.

[69] H.M. Jeong, J.W. Lee, W.H. Shin, Y.J. Choi, H.J. Shin, J.K. Kang, J.W. Choi, Nano Lett., 11 (2011) 2472-2477.

[70] X. Zhao, B.M. Sánchez, P.J. Dobson, P.S. Grant, Nanoscale, 3 (2011) 839-855.

[71] C. Yuan, J. Li, L. Hou, X. Zhang, L. Shen, X.W.D. Lou, Advance. Fun. Mate., 22 (2012) 4592-4597.

[72] H. Jiang, P.S. Lee, C. Li, Energ. Environ. Sci., 6 (2013) 41-53.

[73] H. Gao, F. Xiao, C.B. Ching, H. Duan, ACS Appl. Mater. Inter., 4 (2012) 2801-2810.

[74] C.-W. Kung, H.-W. Chen, C.-Y. Lin, R. Vittal, K.-C. Ho, J. Power Sources, 214 (2012) 91-99.

[75] F. Cao, G. Pan, X. Xia, P. Tang, H. Chen, J. Power Sources, 264 (2014) 161-167.

[76] H. Xia, Y.S. Meng, G. Yuan, C. Cui, L. Lu, Electrochem. Solid-State Lett., 15 (2012) A60-A63.

[77] Y. Lu, F. Zhang, T. Zhang, K. Leng, L. Zhang, X. Yang, Y. Ma, Y. Huang, M. Zhang, Y. Chen, Carbon, 63 (2013) 508-516.

[78] D.W. Wang, F. Li, M. Liu, G.Q. Lu, H.M. Cheng, Angew. Chem., 120 (2008) 379-382.

[79] F. Xu, R. Cai, Q. Zeng, C. Zou, D. Wu, F. Li, X. Lu, Y. Liang, R. Fu, J. Mater. Chem., 21 (2011) 1970-1976.

[80] C. Zhan, Q. Xu, X. Yu, Q. Liang, Y. Bai, Z.-H. Huang, F. Kang, RSC Adv., 6 (2016) 41473-41476.

[81] M. Zhou, F. Pu, Z. Wang, S. Guan, Carbon, 68 (2014) 185-194.

[82] X. He, P. Ling, M. Yu, X. Wang, X. Zhang, M. Zheng, Electrochim. Acta, 105 (2013) 635-641.

[83] J. Wang, S. Kaskel, J. Mater. Chem., 22 (2012) 23710-23725.

[84] X. Yang, L. Zhang, F. Zhang, T. Zhang, Y. Huang, Y. Chen, Carbon, 72 (2014) 381-386.

[85] H. Mi, X. Zhang, X. Ye, S. Yang, J. Power Sources, 176 (2008) 403-409.

[86] Q. Wang, J. Yan, Y. Wang, T. Wei, M. Zhang, X. Jing, Z. Fan, Carbon, 67 (2014) 119-127.

[87] Y. Liang, F. Liang, H. Zhong, Z. Li, R. Fu, D. Wu, J. Mater. Chem. A, 1 (2013) 7000-7005.

[88] H. Yu, J. Wu, L. Fan, K. Xu, X. Zhong, Y. Lin, J. Lin, Electrochim. Acta, 56 (2011) 6881-6886.

[89] P. Chen, H. Chen, J. Qiu, C. Zhou, Nano Res., 3 (2010) 594-603.

[90] H. Yu, J. Wu, L. Fan, Y. Lin, K. Xu, Z. Tang, C. Cheng, S. Tang, J. Lin, M. Huang, J. Power Sources, 198 (2012) 402-407.

[91] J. Han, L.L. Zhang, S. Lee, J. Oh, K.-S. Lee, J.R. Potts, J. Ji, X. Zhao, R.S. Ruoff, S. Park, ACS Nano, 7 (2012) 19-26.

[92] B. You, L. Wang, L. Yao, J. Yang, Chem. Commun., 49 (2013) 5016-5018.

[93] Y. Zhao, M. Liu, X. Deng, L. Miao, P.K. Tripathi, X. Ma, D. Zhu, Z. Xu, Z. Hao, L. Gan, Electrochim. Acta, 153 (2015) 448-455.

[94] D. Zhu, Y. Wang, L. Gan, M. Liu, K. Cheng, Y. Zhao, X. Deng, D. Sun, Electrochim. Acta, 158 (2015) 166-174.

[95] W. Lu, M. Liu, L. Miao, D. Zhu, X. Wang, H. Duan, Z. Wang, L. Li, Z. Xu, L. Gan, Electrochim. Acta, 205 (2016) 132-141.

[96] J. Zakzeski, P.C. Bruijnincx, A.L. Jongerius, B.M. Weckhuysen, Chem. Rev., 110 (2010) 3552-3599.

[97] J. Horáček, F. Homola, I. Kubičková, D. Kubička, Cataly. Today, 179 (2012) 191-198.

[98] K.S. Sing, Pure and Appl. Chem., 57 (1985) 603-619.

[99] M. Liu, J. Qian, Y. Zhao, D. Zhu, L. Gan, L. Chen, J. Mater. Chem. A, 3 (2015) 11517-11526.

[100] M. Liu, X. Ma, L. Gan, Z. Xu, D. Zhu, L. Chen, J. Mater. Chem. A, 2 (2014) 17107-17114.

[101] T. Jawhari, A. Roid, J. Casado, Carbon, 33 (1995) 1561-1565.

[102] X. Yang, C. Li, W. Wang, B. Yang, S. Zhang, Y. Qian, Chem. Commun., (2004) 342-343.

[103] X. Yang, D. Wu, X. Chen, R. Fu, The J. Phys. Chem. C, 114 (2010) 8581-8586.

[104] Y. Tan, C. Xu, G. Chen, Z. Liu, M. Ma, Q. Xie, N. Zheng, S. Yao, ACS Appl. Mater. Inter., 5 (2013) 2241-2248.

[105] Y. Mun, C. Jo, T. Hyeon, J. Lee, K.-S. Ha, K.-W. Jun, S.-H. Lee, S.-W. Hong, H.I. Lee, S. Yoon, Carbon, 64 (2013) 391-402.

[106] H.D. Yoo, J.H. Jang, J.H. Ryu, Y. Park, S.M. Oh, J. Power Sources, 267 (2014) 411-420.

[107] D.P. Dubal, S.H. Lee, J.G. Kim, W.B. Kim, C.D. Lokhande, J. Mater. Chem., 22 (2012) 3044-3052.

[108] S. Jiang, T. Shi, X. Zhan, H. Long, S. Xi, H. Hu, Z. Tang, J. Power Sources, 272 (2014) 16-23.

[109] M. Zhi, C. Xiang, J. Li, M. Li, N. Wu, Nanoscale, 5 (2013) 72-88.

[110] S. Faraji, F.N. Ani, Renew. Sust. Energ. Rev., 42 (2015) 823-834.

[111] N. Devillers, S. Jemei, M.-C. Péra, D. Bienaimé, F. Gustin, J. Power Sources, 246 (2014) 596-608.

[112] S. Faraji, F.N. Ani, J. Power Sources, 263 (2014) 338-360.

[113] J. Yan, Z. Fan, W. Sun, G. Ning, T. Wei, Q. Zhang, R. Zhang, L. Zhi, F. Wei, Adv. Fun. Mater., 22 (2012) 2632-2641.

[114] Y. He, W. Chen, X. Li, Z. Zhang, J. Fu, C. Zhao, E. Xie, ACS Nano, 7 (2012) 174-182.

[115] X.-h. Xia, J.-p. Tu, Y.-q. Zhang, Y.-j. Mai, X.-l. Wang, C.-d. Gu, X.-b. Zhao, RSC Adv., 2 (2012) 1835-1841.

[116] S. Vijayakumar, S. Nagamuthu, G. Muralidharan, ACS Appl. Mater. Inter., 5 (2013) 2188-2196.

[117] H. Jiang, J. Ma, C. Li, Chem. Commun., 48 (2012) 4465-4467.

[118] B.P. Bastakoti, Y. Kamachi, H.S. Huang, L.C. Chen, K.C.W. Wu, Y. Yamauchi, Eur. J. Inorg. Chem., 2013 (2013) 39-43.

[119] C. Largeot, C. Portet, J. Chmiola, P.-L. Taberna, Y. Gogotsi, P. Simon, J. Am. Chem. Soc., 130 (2008) 2730-2731.

[120] Y. Huang, J. Liang, Y. Chen, Small, 8 (2012) 1805-1834.

[121] L. Wang, G. Mu, C. Tian, L. Sun, W. Zhou, P. Yu, J. Yin, H. Fu, ChemSusChem, 6 (2013) 880-889.

[122] M. Zhi, F. Yang, F. Meng, M. Li, A. Manivannan, N. Wu, ACS Sust. Chem. Eng., 2 (2014) 1592-1598.

[123] Y.S. Yun, M.H. Park, S.J. Hong, M.E. Lee, Y.W. Park, H.-J. Jin, ACS Appl. Mater. Inter., 7 (2015) 3684-3690.

[124] W. Si, J. Zhou, S. Zhang, S. Li, W. Xing, S. Zhuo, Electrochim. Acta, 107 (2013) 397-405.

[125] Z. Cai, L. Li, J. Ren, L. Qiu, H. Lin, H. Peng, J. Mater. Chem. A, 1 (2013) 258-261.

[126] R.C.Y. King, F. Roussel, J.-F. Brun, C. Gors, Synthetic Met., 162 (2012) 1348-1356.

[127] S. Brunauer, P.H. Emmett, E. Teller, J. Am. Chem. Soc., 60 (1938) 309-319.

[128] C. Ruan, K. Ai, L. Lu, RSC Adv., 4 (2014) 30887-30895.

[129] S. Shanmugam, T. Osaka, Chem. Commun., 47 (2011) 4463-4465.

[130] L.-F. Chen, Z.-H. Huang, H.-W. Liang, W.-T. Yao, Z.-Y. Yu, S.-H. Yu, Energ. Environ. Sci., 6 (2013) 3331-3338.

[131] B. Zheng, J. Wang, F.-B. Wang, X.-H. Xia, Electrochem. Commun., 28 (2013) 24-26.

[132] M.D. Stoller, R.S. Ruoff, Energ. Environ. Sci., 3 (2010) 1294-1301.

[133] L. Zhang, F. Zhang, X. Yang, G. Long, Y. Wu, T. Zhang, K. Leng, Y. Huang, Y. Ma, A. Yu, Sci. Rep., 3 (2013) 1-9.

[134] T. Zhu, J. Zhou, Z. Li, S. Li, W. Si, S. Zhuo, J. Mater. Chem. A, 2 (2014) 12545-12551.

[135] J. Yan, J. Liu, Z. Fan, T. Wei, L. Zhang, Carbon, 50 (2012) 2179-2188.

[136] Y. Zhao, X. Li, B. Yan, D. Li, S. Lawes, X. Sun, J. Power Sources, 274 (2015) 869-884.

[137] A.W. Anwar, A. Majeed, N. Iqbal, W. Ullah, A. Shuaib, U. Ilyas, F. Bibi, H.M. Rafique, J. Mate. Sci. Technol., 31 (2015) 699-707.

[138] A. Choudhury, H. Chandra, A. Arora, Renew. Sust. Energ. Rev., 20 (2013) 430-442.

[139] B.E. Conway, J. Electrochem. Soc., 138 (1991) 1539-1548.

[140] I. Tanahashi, A. Yoshida, A. Nishino, J. Electrochem. Soc., 137 (1990) 3052-3057.

[141] D. Pech, M. Brunet, H. Durou, P. Huang, V. Mochalin, Y. Gogotsi, P.-L. Taberna, P. Simon, Nature Nanotechnol., 5 (2010) 651-654.

[142] H.-J. Liu, W.-J. Cui, L.-H. Jin, C.-X. Wang, Y.-Y. Xia, J. Mater. Chem., 19 (2009) 3661-3667.

[143] C.-C. Hu, C.-Y. Hung, K.-H. Chang, Y.-L. Yang, J. Power Sources, 196 (2011) 847-850.

[144] B. Wang, J. Park, C. Wang, H. Ahn, G. Wang, Electrochim. Acta, 55 (2010) 6812-6817.

[145] C. Zhou, Y. Zhang, Y. Li, J. Liu, Nano Lett., 13 (2013) 2078-2085.

[146] S.-I. Kim, J.-S. Lee, H.-J. Ahn, H.-K. Song, J.-H. Jang, ACS Appl. Mater. Inter., 5 (2013) 1596-1603.

[147] H. Zhu, X. Wang, X. Liu, X. Yang, Adv. Mater., 24 (2012) 6524-6529.

[148] S. Gao, Y. Chen, H. Fan, X. Wei, C. Hu, H. Luo, L. Qu, J. Mater. Chem. A, 2 (2014) 3317-3324.

[149] P. Wang, H. He, X. Xu, Y. Jin, ACS Appl. Mater. Inter., 6 (2014) 1563-1568.

[150] K. Gong, F. Du, Z. Xia, M. Durstock, L. Dai, Science, 323 (2009) 760-764.

[151] D.-s. Yuan, T.-x. Zhou, S.-l. Zhou, W.-j. Zou, S.-s. Mo, N.-n. Xia, Electrochem. Commun., 13 (2011) 242-246.

[152] W. Li, D. Chen, Z. Li, Y. Shi, Y. Wan, J. Huang, J. Yang, D. Zhao, Z. Jiang, Electrochem. Commun., 9 (2007) 569-573.

[153] J. Romanos, M. Beckner, T. Rash, L. Firlej, B. Kuchta, P. Yu, G. Suppes, C. Wexler, P. Pfeifer, Nanotechnol., 23 (2011) 015401.

[154] Z. Chen, J. Wen, C. Yan, L. Rice, H. Sohn, M. Shen, M. Cai, B. Dunn, Y. Lu, Adv. Energ. Mater., 1 (2011) 551-556.

[155] K. Xia, Q. Gao, J. Jiang, J. Hu, Carbon, 46 (2008) 1718-1726.

[156] J.D. Ding, Y.F. Diao, H.G. Shen, in: Adv. Mater. Res., Trans Tech Publ, 156 (2011) 1211-1214.

[157] C. Wang, L. Sun, Y. Zhou, P. Wan, X. Zhang, J. Qiu, Carbon, 59 (2013) 537-546.

[158] W.-h. Lee, J.H. Moon, ACS Appl. Mater. Inter., 6 (2014) 13968-13976.

[159] M. Sevilla, L. Yu, L. Zhao, C.O. Ania, M.-M. Titiricic, ACS Sust. Chem. Eng., 2 (2014) 1049-1055.

[160] D.W. Wang, F. Li, L.C. Yin, X. Lu, Z.G. Chen, I.R. Gentle, G.Q.M. Lu, H.M. Cheng, Chem. Eur. J., 18 (2012) 5345-5351.

[161] G. Lota, B. Grzyb, H. Machnikowska, J. Machnikowski, E. Frackowiak, Chem. Phys. Lett., 404 (2005) 53-58.

[162] Y. Fan, X. Yang, B. Zhu, P.-F. Liu, H.-T. Lu, J. Power Sources, 268 (2014) 584-590.

[163] K. Wang, Y. Cao, X. Wang, Q. Fan, W. Gibbons, T. Johnson, B. Luo, Z. Gu, Energy, 94 (2016) 666-671.

[164] J. Fang, M. Li, Q. Li, W. Zhang, Q. Shou, F. Liu, X. Zhang, J. Cheng, Electrochim. Acta, 85 (2012) 248-255.

[165] C. Lei, F. Markoulidis, Z. Ashitaka, C. Lekakou, Electrochim. Acta, 92 (2013) 183-187.

[166] M. Min, K. Machida, J.H. Jang, K. Naoi, J. Electrochem. Soc., 153 (2006) A334-A338.

[167] X.-h. Xia, J.-p. Tu, Y.-j. Mai, X.-l. Wang, C.-d. Gu, X.-b. Zhao, J. Mate. Chem., 21 (2011) 9319-9325.

[168] S. Chen, J. Zhu, X. Wu, Q. Han, X. Wang, ACS Nano, 4 (2010) 2822-2830.

[169] H. Wei, X. Yan, Q. Wang, S. Wu, Y. Mao, Z. Luo, H. Chen, L. Sun, S. Wei, Z. Guo, Energ. Environ. Focus, 2 (2013) 112-120.

[170] X. Chen, H. Wang, H. Yi, X. Wang, X. Yan, Z. Guo, The J. Phys. Chem. C, 118 (2014) 8262-8270.

[171] M. Seredych, T.J. Bandosz, J. Mater. Chem. A, 1 (2013) 11717-11727.

[172] H. Guo, Q. Gao, J. Power Sources, 186 (2009) 551-556.

[173] H. Wei, H. Gu, J. Guo, S. Wei, Z. Guo, J. Electrochem. Soc., 160 (2013) G3038-G3045.

[174] J. Ding, H. Wang, Z. Li, K. Cui, D. Karpuzov, X. Tan, A. Kohandehghan, D. Mitlin, Energ. Environ. Sci., 8 (2015) 941-955.

[175] Y. Liang, D. Wu, R. Fu, Langmuir, 25 (2009) 7783-7785.

[176] H. Yamada, I. Moriguchi, T. Kudo, J. Power Sources, 175 (2008) 651-656.

[177] W. Xing, S. Qiao, R. Ding, F. Li, G. Lu, Z. Yan, H. Cheng, Carbon, 44 (2006) 216-224.

[178] S. Chen, J. Duan, Y. Tang, S. Zhang Qiao, Chem. Eur. J., 19 (2013) 7118-7124.

[179] W. Li, F. Zhang, Y. Dou, Z. Wu, H. Liu, X. Qian, D. Gu, Y. Xia, B. Tu, D. Zhao, Adv. Energ. Mater., 1 (2011) 382-386.

[180] S. Sarangapani, B. Tilak, C.P. Chen, J. Electrochem. Soc., 143 (1996) 3791-3799.

[181] J. Li, W. Zhao, F. Huang, A. Manivannan, N. Wu, Nanoscale, 3 (2011) 5103-5109.

[182] L. Huang, D. Chen, Y. Ding, S. Feng, Z.L. Wang, M. Liu, Nano Lett., 13 (2013) 3135-3139.

[183] P. Simon, Y. Gogotsi, Nature Mater., 7 (2008) 845-854.

[184] Z.-D. Huang, B. Zhang, S.-W. Oh, Q.-B. Zheng, X.-Y. Lin, N. Yousefi, J.-K. Kim, J. Mater. Chem., 22 (2012) 3591-3599.

[185] K. Wang, L. Li, T. Zhang, Z. Liu, Energy, 70 (2014) 612-617.

[186] B. Li, F. Dai, Q. Xiao, L. Yang, J. Shen, C. Zhang, M. Cai, Energ. Environ. Sci., 9 (2016) 102-106.

[187] Z.S. Wu, K. Parvez, A. Winter, H. Vieker, X. Liu, S. Han, A. Turchanin, X. Feng, K. Müllen, Adv. Mater., 26 (2014) 4552-4558.

[188] U.B. Nasini, V.G. Bairi, S.K. Ramasahayam, S.E. Bourdo, T. Viswanathan, A.U. Shaikh, J. Power Sources, 250 (2014) 257-265.

[189] W. Wang, Q. Hao, W. Lei, X. Xia, X. Wang, J. Power Sources, 269 (2014) 250-259.

[190] D. Bhattacharjya, M.-S. Kim, T.-S. Bae, J.-S. Yu, J. Power Sources, 244 (2013) 799-805.

[191] Y. Shao, J. Wang, H. Wu, J. Liu, I.A. Aksay, Y. Lin, Electroanalysis, 22 (2010) 1027-1036.

[192] H. Wang, Y. Yang, Y. Liang, J.T. Robinson, Y. Li, A. Jackson, Y. Cui, H. Dai, Nano Lett., 11 (2011) 2644-2647.

[193] D.A. Brownson, C.E. Banks, Chem. Commun., 48 (2012) 1425-1427.

[194] A. Du, Z. Zhu, S.C. Smith, J. Am. Chem. Soc., 132 (2010) 2876-2877.

[195] K.S. Kim, Y. Zhao, H. Jang, S.Y. Lee, J.M. Kim, K.S. Kim, J.-H. Ahn, P. Kim, J.-Y. Choi, B.H. Hong, Nature, 457 (2009) 706-710.

[196] L. Gao, H. Xu, L. Li, Y. Yang, Q. Fu, X. Bao, K.P. Loh, 2D Mater., 3 (2016) 021001.

[197] X. Lu, M. Yu, H. Huang, R.S. Ruoff, Nanotechnol., 10 (1999) 269.

[198] C. Berger, Z. Song, X. Li, X. Wu, N. Brown, C. Naud, D. Mayou, T. Li, J. Hass, A.N. Marchenkov, Science, 312 (2006) 1191-1196.

[199] M. Choucair, P. Thordarson, J.A. Stride, Nature Nanotechnol., 4 (2009) 30-33.

[200] S. Stankovich, D.A. Dikin, R.D. Piner, K.A. Kohlhaas, A. Kleinhammes, Y. Jia, Y. Wu, S.T. Nguyen, R.S. Ruoff, Carbon, 45 (2007) 1558-1565.

[201] M. Fu, Q. Jiao, Y. Zhao, J. Mater. Chem. A, 1 (2013) 5577-5586.

[202] S. Stankovich, R.D. Piner, X. Chen, N. Wu, S.T. Nguyen, R.S. Ruoff, J. Mater. Chem., 16 (2006) 155-158.

[203] Y. Sun, X. Hu, W. Luo, Y. Huang, The J. Phys. Chem. C, 116 (2012) 20794-20799.

[204] K.N. Kudin, B. Ozbas, H.C. Schniepp, R.K. Prud'Homme, I.A. Aksay, R. Car, Nano Lett., 8 (2008) 36-41.

[205] W. Zhou, K. Zhou, X. Liu, R. Hu, H. Liu, S. Chen, J. Mater. Chem. A, 2 (2014) 7250-7255.

[206] B. Xu, S. Yue, Z. Sui, X. Zhang, S. Hou, G. Cao, Y. Yang, Energ. Environ. Sci., 4 (2011) 2826-2830.

[207] C. Liu, Z. Yu, D. Neff, A. Zhamu, B.Z. Jang, Nano Lett., 10 (2010) 4863-4868.

[208] Y. Qiu, X. Zhang, S. Yang, Phys. Chem. Chem. Phys., 13 (2011) 12554-12558.

[209] T. Kim, G. Jung, S. Yoo, K.S. Suh, R.S. Ruoff, ACS Nano, 7 (2013) 6899-6905.

[210] Z. Wen, X. Wang, S. Mao, Z. Bo, H. Kim, S. Cui, G. Lu, X. Feng, J. Chen, Adv. Mater., 24 (2012) 5610-5616.

[211] W.-w. Liu, X.-b. Yan, J.-w. Lang, C. Peng, Q.-j. Xue, J. Mater. Chem., 22 (2012) 17245-17253.

[212] Y. Liu, Y. Li, M. Zhong, Y. Yang, Y. Wen, M. Wang, J. Mater. Chem., 21 (2011) 15449-15455.

[213] R. Ramachandran, M. Saranya, V. Velmurugan, B.P. Raghupathy, S.K. Jeong, A.N. Grace, Appl. Energ., 153 (2015) 22-31.

[214] I.I. Misnon, N.K.M. Zain, R.A. Aziz, B. Vidyadharan, R. Jose, Electrochim. Acta, 174 (2015) 78-86.

[215] M. Biswal, A. Banerjee, M. Deo, S. Ogale, Energ. Environ. Sci., 6 (2013) 1249-1259.

[216] H.-P. Cong, X.-C. Ren, P. Wang, S.-H. Yu, Energ. Environ. Sci., 6 (2013) 1185-1191.

[217] Y. Zhu, S. Murali, M.D. Stoller, K. Ganesh, W. Cai, P.J. Ferreira, A. Pirkle, R.M. Wallace, K.A. Cychosz, M. Thommes, Science, 332 (2011) 1537-1541.

[218] C. Guan, X. Xia, N. Meng, Z. Zeng, X. Cao, C. Soci, H. Zhang, H.J. Fan, Energ. Environ. Sci., 5 (2012) 9085-9090.

[219] Y.Y. Wang, B.H. Hou, H.Y. Lü, C.L. Lü, X.L. Wu, ChemistrySelect, 1 (2016) 1441-1447.

[220] D. Puthusseri, V. Aravindan, S. Madhavi, S. Ogale, Energ. Environ. Sci., 7 (2014) 728-735.

[221] C. Xiang, M. Li, M. Zhi, A. Manivannan, N. Wu, J. Power Sources, 226 (2013) 65-70.

[222] W. Zhou, X. Cao, Z. Zeng, W. Shi, Y. Zhu, Q. Yan, H. Liu, J. Wang, H. Zhang, Energ. Environ. Sci., 6 (2013) 2216-2221.

[223] Z. Lei, J. Zhang, X. Zhao, J. Mater. Chem., 22 (2012) 153-160.

[224] C. Lei, N. Amini, F. Markoulidis, P. Wilson, S. Tennison, C. Lekakou, J. Mater. Chem. A, 1 (2013) 6037-6042.

[225] K. Wang, Y. Cao, Z. Gu, P. Ahrenkiel, J. Lee, Q.H. Fan, RSC Adv., 6 (2016) 26738-26744.

[226] A. Borenstien, M. Noked, S. Okashy, D. Aurbach, J. Electrochem. Soc., 160 (2013) A1282-A1285.

[227] A. Pandolfo, A. Hollenkamp, J. Power Sources, 157 (2006) 11-27.

[228] Q. Cheng, J. Tang, J. Ma, H. Zhang, N. Shinya, L.-C. Qin, Phys. Chem. Chem. Phys., 13 (2011) 17615-17624.

[229] J. Zhang, J. Jiang, H. Li, X. Zhao, Energ. Environ. Sci., 4 (2011) 4009-4015.

[230] C. Lee, X. Wei, J.W. Kysar, J. Hone,Science, 321 (2008) 385-388.

[231] L.A. Jauregui, Y. Yue, A.N. Sidorov, J. Hu, Q. Yu, G. Lopez, R. Jalilian, D.K. Benjamin, D.A. Delkd, W. Wu, ECS Trans., 28 (2010) 73-83.

[232] L.L. Zhang, R. Zhou, X. Zhao, J. Mater. Chem., 20 (2010) 5983-5992.

[233] M. Pumera, Chem. Rec., 9 (2009) 211-223.

[234] Y. Zhu, S. Murali, W. Cai, X. Li, J.W. Suk, J.R. Potts, R.S. Ruoff, Adv. Mater., 22 (2010) 3906-3924.

[235] L.-S. Zhang, L.-Y. Jiang, H.-J. Yan, W.D. Wang, W. Wang, W.-G. Song, Y.-G. Guo, L.-J. Wan, J. Mater. Chem., 20 (2010) 5462-5467.

[236] X. Wang, L. Zhi, K. Müllen, Nano Lett., 8 (2008) 323-327.

[237] L. Qu, Y. Liu, J.-B. Baek, L. Dai, ACS Nano, 4 (2010) 1321-1326.

[238] X. Yang, X. Zhang, Y. Ma, Y. Huang, Y. Wang, Y. Chen, J. Mater. Chem., 19 (2009) 2710-2714.

[239] B. Zhang, Q. Li, T. Cui, Biosens. Bioelectron., 31 (2012) 105-109.

[240] Z. Chen, Y.-M. Lin, M.J. Rooks, P. Avouris, Physica E: Low-dimens. Syst. Nanostruct., 40 (2007) 228-232.

[241] K.S. Novoselov, A.K. Geim, S. Morozov, D. Jiang, Y. Zhang, S.a. Dubonos, I. Grigorieva, A. Firsov, Science, 306 (2004) 666-669.

[242] P.R. Somani, S.P. Somani, M. Umeno, Chem. Phys. Lett., 430 (2006) 56-59.

[243] H. Huang, W. Chen, S. Chen, A.T.S. Wee, ACS Nano, 2 (2008) 2513-2518.

[244] H. Wang, J.T. Robinson, X. Li, H. Dai, J. Am. Chem. Soc., 131 (2009) 9910-9911.

[245] W.S. Hummers Jr, R.E. Offeman, J. Am. Chem. Soc., 80 (1958) 1339-1339.

[246] E. Haque, M.M. Islam, E. Pourazadi, M. Hassan, S.N. Faisal, A.K. Roy, K. Konstantinov, A.T. Harris, A.I. Minett, V.G. Gomes, RSC Adv., 5 (2015) 30679-30686.

[247] L. Stobinski, B. Lesiak, A. Malolepszy, M. Mazurkiewicz, B. Mierzwa, J. Zemek, P. Jiricek, I. Bieloshapka, J. Electron Spectros. Relat. Phenomena, 195 (2014) 145-154.

[248] Y. Han, Y. Wu, M. Shen, X. Huang, J. Zhu, X. Zhang, J. Mater. Sci., 48 (2013) 4214-4222.

[249] F.M. Hassan, V. Chabot, J. Li, B.K. Kim, L. Ricardez-Sandoval, A. Yu, J. Mater. Chem. A, 1 (2013) 2904-2912.

[250] J.N. Coleman, Acc. Chem. Res., 46 (2012) 14-22.

[251] Z. Li, Z. Xu, H. Wang, J. Ding, B. Zahiri, C.M. Holt, X. Tan, D. Mitlin, Energ. Environ. Sci., 7 (2014) 1708-1718.

PUBLICATIONS

[1] **K. Wang**, M. Xu, Y. Gu, Z. Gu, J. Liu, Q.H. Fan, ***Nano Energy,*** 31 (2017) 486-494.

[2] **K. Wang**, M. Xu, M. Shrestha, Z. Gu, Q.H. Fan, ***Mater. Today Energy,*** 4 (2017) 7-13.

[3] **K. Wang**, M. Xu, Y. Gu, Z. Gu, Q.H. Fan, ***J. Power Sources,*** 332 (2016) 180-186.

[4] **K. Wang**, Y. Cao, X. Wang, M.A. Castro, B. Luo, Z. Gu, J. Liu, J.D. Hoefelmeyer, Q. Fan, ***J. Power Sources***, 307 (2016) 462-467.

[5] **K. Wang**, Y. Cao, X. Wang, Q. Fan, W. Gibbons, T. Johnson, B. Luo, Z. Gu, ***Energy,*** 94 (2016) 666-671.

[6] **K. Wang**, Y. Cao, X. Wang, P.R. Kharel, W. Gibbons, B. Luo, Z. Gu, Q. Fan, L. Metzger, ***Energy,*** 101 (2016) 9-15.

[7] **K. Wang**, M. Xu, X. Wang, Z. Gu, Q.H. Fan, W. Gibbons, J. Croat, ***RSC Adv.,*** 7 (2017) 8236-8240.

[8] **K. Wang**, Y. Cao, Z. Gu, P. Ahrenkiel, J. Lee, Q.H. Fan, ***RSC Adv.,*** 6 (2016) 26738-26744.

[9] **K. Wang**, M. Xu, Z. Gu, P. Ahrenkiel, J. Lee, W. Gibbons, J. Croat, Q. Fan, ***Int. J. Hydrogen Energy,*** 41 (2016) 13109-13115.

[10] Y. Cao, **K. Wang**, X. Wang, Z. Gu, W. Gibbons, H. Vu, ***Bioresour. Technol.,*** 196 (2015) 525-532.

[11] Y. Cao, **K. Wang**, X. Wang, Z. Gu, W. Gibbons, H. Vu, ***Appl. Surf. Sci.,*** 349 (2015) 1-7.

[12] Y. Cao, **K. Wang**, X. Wang, Z. Gu, Q. Fan, W. Gibbons, J.D. Hoefelmeyer, P.R. Kharel, M. Shrestha, ***Electrochim. Acta,*** 212 (2016) 839-847.

[13] Y. Cao, **K. Wang**, X. Wang, Z. Gu, T. Ambrico, W. Gibbons, Q. Fan, A.-A. Talukder, ***J. Energy Chem.,*** 26 (2017) 35-41.

[14] Y. Cao, Y. Gu, **K. Wang**, X. Wang, Z. Gu, T. Ambrico, M.A. Castro, J. Lee, W. Gibbons, J.A. Rice, ***J. Taiwan Inst. Chem. E.,*** 66 (2016) 347-356.

[15] H. Wang, Z. Zhang, Y. Yang, **K. Wang**, S. Ji, J. Key, Y. Ma, R. Wang, ***J. Solid State Electrochem.*** 19 (2015) 1727-1733.